Lithium Extraction and Purification from Geothermal Brine

For Eric Anderson

Prepared by Sarah Bhargava, Maurice Curran,
Madaline Marland & Allison Sawyer

Chemical Engineering Department, University of Virginia

May 11, 2023

Table of Contents

SECTION 1: EXECUTIVE SUMMARY

Current and pending mine projects have supply capability covering only half of projected 2030 global lithium needs, and "are not ready to to support accelerated energy transitions" (IEA, 2022, p. 11). It is thus in the economic and security interests of the United States to invest in lithium extraction research (Hailes, 2022; Parker et al., 2022). Geothermal brines at high temperatures–on the order of 200-300°C–and high pressures–on the order of 20,000 psig–can dissolve metals including lithium present in specific geological regions (Ventura et al., 2020, p. 5). Geothermal brines at Salton Sea, California present a significant opportunity to increase the domestic supply of lithium (Warren, 2022, p. 15).

The following work showcases process design surrounding a novel sorbent for lithium extraction from geothermal brine. Mineral extraction from geothermal brines has historically been hindered by silica scaling, brine corrosivity, and low selectivity for lithium over other minerals. University of Virginia professors Geise, Koenig, and Giri designed a sorbent, Iron (III) Phosphate ($FePO_4$), which offers high selectivity for lithium over other minerals present in the brine. The designed process with iron (III) phosphate sorbent achieves 99% overall process recovery for lithium and 99 weight % purity.

The overall process design consists of 4 main process blocks: additives mixing, a packed bed reactor network, electrolyzers, and a crystallization unit to achieve the final lithium hydroxide monohydrate product ($LiOH \cdot H_2O$). The additives mixing unit sees the addition of tripotassium citrate monohydrate ($K_3(C_6H_5O_7) \cdot H_2O$), to lower the brine reduction potential such that adsorption in the packed bed reactors is favorable, and ferric chloride ($FeCl_2$), to allow for maximum lithium uptake. In the packed bed reactor network, the sorbent material Iron (III) Phosphate ($FePO_4$) is used to extract lithium (Li^+) using consecutive adsorption and desorption schemes. In the electrolyzers, stripped lithium chloride (LiCl) is converted to lithium hydroxide (LiOH) before crystallization into the final lithium hydroxide monohydrate product ($LiOH \cdot H_2O$).

Based on discounted cash flow analysis, Section 6.7, with a 7-year straight-line depreciation schedule, a plant lifetime of 20 years, and a battery grade lithium hydroxide monohydrate sale price of $65/kg (*About lithium*, 2023), the project IRR is 592%. This indicates an extremely attractive investment opportunity. The return on investment (ROI) is determined to be 11,700% over 20 years with a final cumulative cash position of 14 billion USD. The process

and plant designed within this report should be strongly considered as a candidate for addition to existing Salton Sea geothermal plants. Further work should be done to finalize chemical and scale specifications, but the overall profitability suggests this is a worthwhile investment of time and resources.

SECTION 2: INTRODUCTION

Rapid clean energy scale-up will generate increased demand for critical minerals; thus, new and diverse supply sources are necessary to counter supply strains (IEA, 2022, p. 14). These strains arise particularly from rapid supply chain expansion (Olivetti et al., 2017, p. 229), high geographic reserve location and refining capability concentration (Sun et al., 2021, p. 12180), mining asset exposure to climate risk (Delevingne et al., 2020, pp. 2-5), and long project development time (IEA, 2022, p. 12). Lithium is classified as a critical mineral "hav[ing] a supply chain that is vulnerable to disruption and serv[ing] an essential function in the manufacturing of a product, the absence of which would have significant consequences for the economic or national security of the United States" (USGS, 2022, p. 17).

Lithium hydroxide monohydrate ($LiOH \cdot H_2O$) and lithium carbonate (Li_2CO_3) are used in battery applications ranging from electric vehicles to personal care items and baseline power storage. Lithium demand from traditional car companies is increasing as they shift their business models toward vehicle electrification (Early, 2022). Global demand for lithium is therefore projected to reach 1.65 million US tons of lithium carbonate equivalent (LCE) by 2025, compared to the 595,000 US tons of LCE in 2021 (World Economic Forum, 2023). Current and pending mine projects have supply capability covering only half of projected 2030 lithium needs, and "are not ready to to support accelerated energy transitions" (IEA, 2022, p. 11).

The U.S. contributes less than 2% of the world supply of lithium while holding 17% of the global lithium reserves (GTO, 2021). Starting March 18th, 2022, the Department of Energy is supporting up to five pilot training programs in energy and automotive communities as well as encouraging partnerships between industry and labor for the increase in domestic lithium battery supply. To secure a sustainable supply of lithium and other critical minerals, the Biden-Harris administration and the DOE increased funding by $44 million to specifically sponsor research that increases mineral yield while decreasing energy. This mission stresses the importance of developing and optimizing an extraction and purification process for battery-grade lithium hydroxide monohydrate (US DOE, 2022).

Geothermal brines at Salton Sea, California present a significant opportunity to increase the domestic supply of lithium (Warren, 2022, p. 15). Geothermal brines at high temperatures–on the order of 200-300°C–and high pressures–on the order of 20,000 psig–can dissolve metals

including lithium present in specific geological regions (Ventura et al., 2020, p. 5). The 11 existing geothermal plants in the Salton Sea region have the capacity to produce lithium approximately 10 times the current U.S demand (Warren, 2021). Research interest in lithium extraction from underground geothermal reservoirs has persisted since the 1970's (Hoffmann, 1975, pp. 4-9), but only recently has it evolved into an economically and technically viable scheme (Warren, 2021). Geothermal brine exploitation has historically been hindered by severe scaling, primarily silica deposition, and equipment corrosion owing to low brine pH (Hoffmann, 1975, pp. 9-13). Anti-scaling advancements now allow electricity production from the geothermal fluid heat. Licensed private companies produce electricity and reinject the lithium-rich liquid into the underground reservoirs it came from without extracting the lithium; thus, lithium extraction units can be added to existing geothermal plant infrastructure (Imperial Valley Geothermal Area).

University of Virginia professors Gary Koenig, Geoffrey Geise, and Gaurav Giri from the chemical engineering department comprise a team for Targeted Extraction of Lithium with Electroactive Particles for Recovery Technology (TELEPORT). They are competing for grant allocation from the Department of Energy's Geothermal Technologies Office and National Renewable Energy Laboratory (US DOE, 2022) for lithium extraction in the Salton Sea region. The following technical work seeks to process engineer unit operations surrounding a novel Project TELEPORT sorbent material for geothermally sourced lithium extraction and lithium hydroxide monohydrate ($LiOH \cdot H_2O$) production. This work will be based on existing geothermal plants within the Salton Sea Known Geothermal Resource Area (KGRA) in California, US.

SECTION 3: PRIOR WORKS

Current domestic projects in lithium-brine extraction are based on the Smackover Formation brine in Arkansas and Salton Sea brines from California. These locations were selected based on the high concentration of lithium (200+ mg/L) and other alkaline earth elements in the geothermal brines. In the South West Arkansas project (SWA), the flowsheet of the process design is separated into three main parts: brine pre-treatment, direct lithium extraction (DLE) technology and conversion. Our process starts at the steps following brine pre-treatment, which involves removal of gas and organic liquids, H_2S (hydrogen sulfide) and solids. For the DLE portion, the SWA project explores the use of a packed bed reactor (PBR) with loading, washing and stripping steps to produce LiCl. The product stream leaving the PBR then undergoes ion exchange polishing and reverse osmosis steps to remove the divalent cations like calcium and magnesium, as well as evaporative concentration. Following this, the stream goes through electrochemical conversion to produce lithium hydroxide and undergoes post-processing steps involving evaporation and crystallization, and finally washing and drying. Any waste streams involving barren brine are reinjected to the wells. The process outlined in SWA does not utilize a sorbent that is as effective as the one discussed in this paper, as the lower sorbent selectivity from the paper requires additional steps following the packed bed reactor to remove divalent cations before the brine is sent to the electrolysis unit. These processes led to an annual production of 30,000 tons with an overall recovery of 90% (NORAM et al., 2021).

There are several strategies for DLE that are currently used in industry, including adsorption, ion exchange and solvent extraction. Adsorption involves the physical binding of the lithium chloride from the brine onto the sorbent where it is removed with a stripping agent. The ion exchange process consists of the lithium ion (Li^+) in the brine chemically absorbing into a solid ion exchange material where it is swapped for a positive ion such as hydrogen (H^+) from hydrochloric acid (HCl). Finally, with solvent extraction, a liquid phase that contains adsorptive or ion-exchange properties removes the LiCl from the brine.

Previous scholars like Berthold and Baker explored lithium recovery using ion-exchange and precipitation, where higher pH conditions (7.5-8) and lime were used to precipitate metal hydroxides and remove iron, silica, manganese and zinc. After the addition of $AlCl_3$, lithium extraction occurred through the precipitation of LiOH. This process achieved high recoveries of

lithium (greater than 98%) at a pH of 7.5 and a temperature between 75 and 85°C; however, it is important to note that the optimal lithium recovery parameters vary greatly based on the physical and chemical properties of the geothermal brine.

The extraction of lithium was also explored on a scale with post-flash brine flow of 10 gallons per minute. Schultze and Bauer describe a process with 99% recovery of lithium from the geothermal brines at Salton Sea. More specifically, through the addition of $AlCl_3$ solution and lime slurry, a lithium-aluminum precipitate is dissolved in HCl and sparged with gaseous HCl. This results in the removal of $AlCl_3$ to produce a solution of LiCl and $CaCl_2$. With further evaporation at 100°C and purification through dissolving the final lithium product in water and treating with oxalic acid, a purity of 99.9% is achieved with a 89% recovery.

For the packed bed reactor, the SRI International Chemistry and Materials Laboratory used nanostructured hydrous manganese oxide (HMO) as a sorbent which corresponds to a lithium capacity as high as 16.2 mg Li/g sorbent. The laboratory group used a feed of synthetic brine with compositions similar to those in actual geothermal brine samples from Salton Sea. They further used ion sieves to allow hydrogen ions to replace lithium ions through the addition of a hydrochloric acid solution for extraction (CEC, 2020). At a pH of 7.2, the highest separation coefficient, which describes the selectivity of the regeneration solution for lithium against other metal ions, was 323 against sodium ions. This suggests high selectivity for lithium as opposed to sodium is feasible.

Similar reactions between iron (III) phosphate and iron cyanide in a packed bed flow reactor show flows in the laminar regime with increased flow rates affecting the bulk transport of the iron cyanide reactant (Gupta et al., 2022). Overcoming mass transport resistance is therefore considered most important in the packed bed reactor network. The assumptions for our packed bed reactor system are built upon diffusion-limiting transport and therefore instantaneous reaction rates. Varying temperature on the packed bed reactor further shows a similar conversion of LFP (lithium iron phosphate) to FP (iron phosphate) of 80% at temperatures of 22.4 and 40 °C.

Regarding the electrolyzer unit, Grageda (2020) performed experiments to determine the optimal conditions for maximizing the production of battery grade (99 weight percent) lithium hydroxide monohydrate by membrane electrodialysis. Using an anolyte with impurities similar to those found in geothermal brines and a catholyte of deionized water with small concentrations of lithium hydroxide (LiOH) in a batch set-up, they determined the production levels and

corresponding purities of LiOH. The overall reaction involved the production of Cl_2 gas, H_2 gas and LiOH from reactants LiCl and H_2O, with the oxidation of the chlorine ions to chloride gas occurring at the anode and the reduction of water into hydroxide ions and hydrogen gas occurring at the cathode. The similarities to our process suggests the benefits of modeling the industrial-scale electrolyzer unit based on the optimal production conditions outlined in this paper.

SECTION 4: DISCUSSION

In this section, an overview and optimized designs for the Lithium Extraction system will be presented.

4.1 System Overview

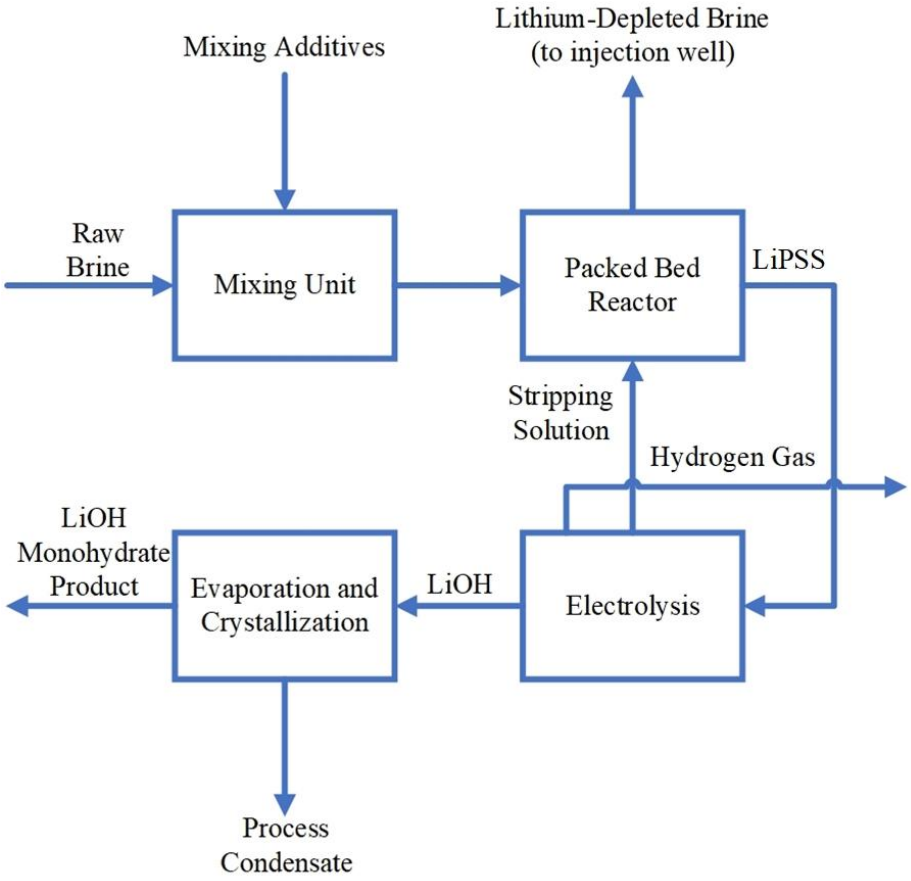

Figure 1. General Block Flow Diagram of Lithium Extraction and Purification

The overall process design consists of four main process blocks and is outlined in Figure 1.

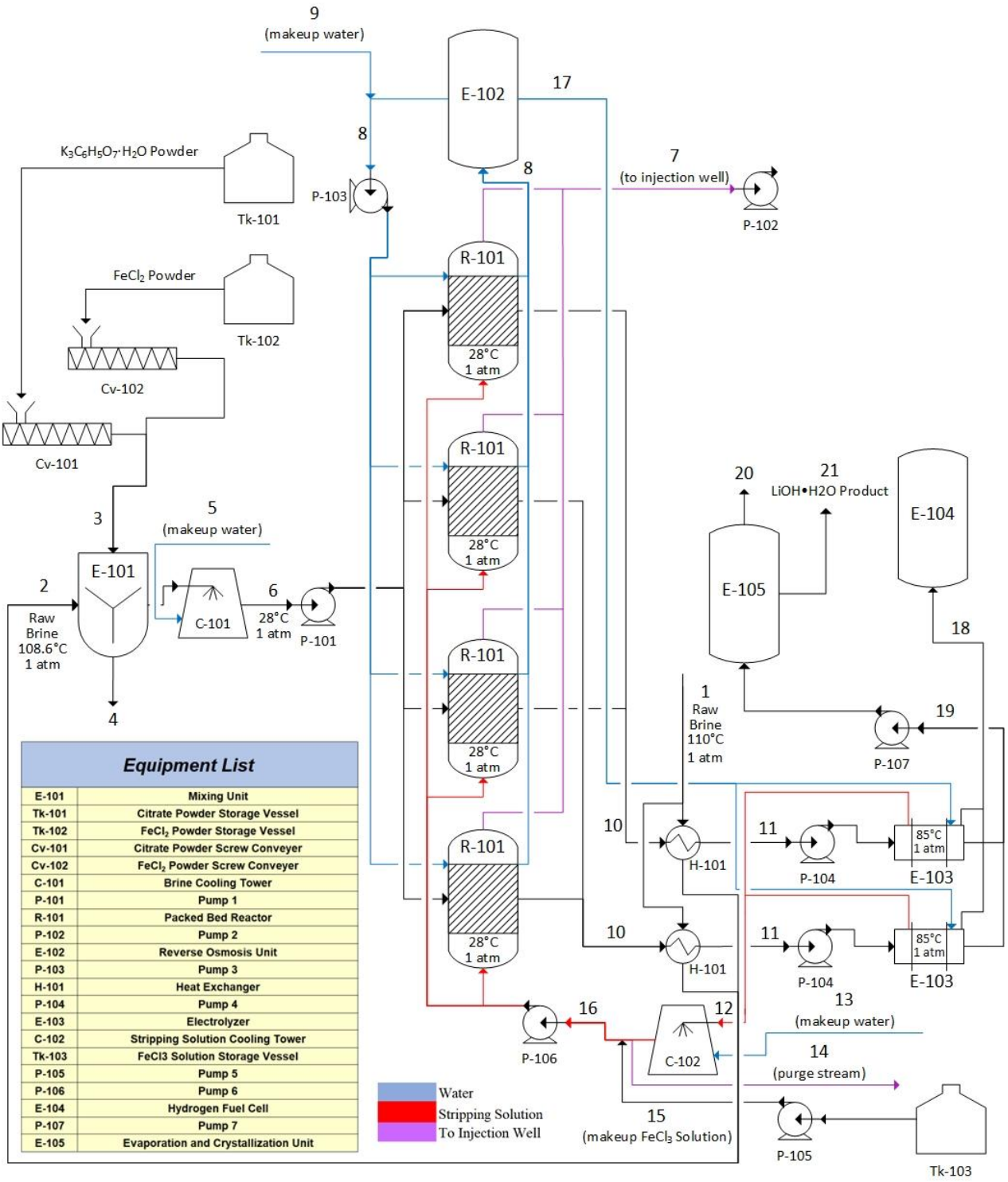

Equipment List	
E-101	Mixing Unit
Tk-101	Citrate Powder Storage Vessel
Tk-102	$FeCl_2$ Powder Storage Vessel
Cv-101	Citrate Powder Screw Conveyer
Cv-102	$FeCl_2$ Powder Screw Conveyer
C-101	Brine Cooling Tower
P-101	Pump 1
R-101	Packed Bed Reactor
P-102	Pump 2
E-102	Reverse Osmosis Unit
P-103	Pump 3
H-101	Heat Exchanger
P-104	Pump 4
E-103	Electrolyzer
C-102	Stripping Solution Cooling Tower
Tk-103	FeCl3 Solution Storage Vessel
P-105	Pump 5
P-106	Pump 6
E-104	Hydrogen Fuel Cell
P-107	Pump 7
E-105	Evaporation and Crystallization Unit

Figure 2. Process Flow Diagram of Lithium Extraction and Purification

Figure 2 displays a more detailed process flow diagram of the process. Starting after the pre-treatment steps that include the removal of silica and other inorganic solids, the selected

process is split into four main parts: mixing, packed bed reactor network, electrolysis, and crystallization. Prior to the mixing unit, the raw brine is used to heat a lithium-rich stream exiting the packed bed reactors before entering the electrolyzer units. The mixing unit involves the addition of tripotassium citrate monohydrate to the brine in order to make the adsorption reaction more favorable. The addition of citrate lowers the standard potential of the $Fe^{2|3+}$solution in the brine to below the standard potential of the FP to drive the adsorption reaction. To capture the total amount of lithium present in the brine, iron must be present in the brine at a 1:1 ratio to lithium; thus, a small amount $FeCl_2$ is added to ensure a 1:1 molar concentration ratio between Fe^{2+} and Li^+. The design of this unit is detailed in Section 4.2. We previously explored the addition of a filtering unit before the brine encountered the sorbent material to filter out the larger divalent cations. However, due to the highly selective nature of the packed bed reactor to smaller monovalent cations, the filtration step was deemed unnecessary.

Following the additives mixing, the resulting brine stream is sent into a series of two cooling towers where its temperature is lowered from 86℃ to 25℃. The cooled stream is then fed into a packed bed reactor. The sorption process can be further divided into four stages: loading, washing, and stripping, and washing. Loading the packed bed refers to the chemisorption of lithium from the inlet brine stream to the iron (III) phosphate sorbent structure. The electron transfer between the sorbent iron $Fe^{3+}PO_4(s)$ and brine iron $Fe^{2+}(aq)$ facilitates lithium adsorption. The brine solution leaving the bed during adsorption is reinjected. This reinjected stream is composed of multivalent cations like calcium and manganese that do not adsorb to the sorbent. Additionally, the reinjected stream is fed back into the well without the need for pH re-balancing considering the acidic nature of the brine. The washing step following loading entails washing the bed with H_2O to remove impurities that are in the interstitial spaces of the iron (III) phosphate. Following washing, the stripping step involves adding a stream of aqueous ferric chloride ($FeCl_3$) to the reactor to strip the lithium from the sorbent material and produce lithium chloride (LiCl) as well as the reduced $FeCl_2$ in the outlet stream. Some sodium chloride (NaCl) is also in the stream due to the sorbent's non-negligible selectivity for sodium ions. The second washing step follows sorbent stripping and ensures the reactor is free of impurities for regeneration. The specific calculations and process for the sorption unit is detailed in Section 4.3.

After the packed bed reactor, the LiCl, $FeCl_2$ and NaCl aqueous stream is fed to the electrolyzer units where lithium hydroxide monohydrate is produced. In the electrolyzer,

hydrogen gas (H_2) and $FeCl_3$ are formed, with the $FeCl_3$ returning to the sorbent unit for use as the stripping agent. Within this process unit, the brine serves as the anolyte whereas H_2O from reverse osmosis serves as the catholyte. After undergoing electrolysis, the produced lithium hydroxide undergoes further crystallization steps to prepare the lithium hydroxide monohydrate product for delivery.

Table 1. Overall Mass Flow Summary Table for a Proposed Lithium Extraction and Purification Process from Geothermal Brines

Stream		1	2	3	4	5	6	7	8	9	10	11	12	13	14	15	16	17	18	19	20	21
Temperature (°C)		110	86.25	25	86.25	28	28	28	25	25	28	85	85	28	28	28	28	25	85	85	120	120
Pressure (atm)		1	1	1	1	1	1	1	1	1	1	1	1	1	1	1	1	1	1	1	1	1
Mass Flow (kg/hr)		1,637,129.97	1,637,129.97	16,573.05	14,587.06	121,276.98	1,639,115.92	1,638,726.05	43,446.78	11,452.63	340,646.47	340,646.47	680,906.81	63,412.80	68,090.68	68,084.26	680,900.39	11,452.63	55.37	11,787.32	9,483.34	2,303.98
Component Flow (kg/hr)	H_2O	1,151,696.79	1,151,696.79	—	802.75	121,276.98	1,151,775.51	1,151,775.51	43,446.78	11,452.63	335,980.92	335,980.92	671,961.83	63,412.80	67,196.18	67,196.18	671,961.83	11,452.63	—	10,463.11	9,483.34	979.77
	LiOH	—	—	—	—	—	—	—	—	—	—	—	—	—	—	—	—	—	—	1,302.55	—	1,302.55
	LiCl	—	—	—	—	—	—	—	—	—	1,152.82	1,152.82	—	—	—	—	—	—	—	—	—	—
	Li	380.99	380.99	—	—	—	380.99	3.50	—	—	—	—	—	—	—	—	—	—	—	—	—	—
	$FeCl_2$	—	—	699.67	—	—	—	—	—	—	3,469.95	3,469.95	—	—	—	—	—	—	—	—	—	—
	$FeCl_3$	—	—	—	—	—	—	—	—	—	—	—	8,880.81	—	888.08	888.08	8,880.81	—	—	—	—	—
	H_2	—	—	—	—	—	—	—	—	—	—	—	—	—	—	—	—	—	55.37	—	—	—
	NaOH	—	—	—	—	—	—	—	—	—	—	—	—	—	—	—	—	—	—	21.66	—	21.66
	NaCl	—	—	—	—	—	—	—	—	—	42.78	42.78	64.17	—	6.42	—	57.75	—	—	—	—	—
	Na	97,970.44	97,970.44	—	—	—	97,970.44	97,958.06	—	—	—	—	—	—	—	—	—	—	—	—	—	—
	Ca	58,716.27	58,716.27	—	5,358.03	—	53,358.25	53,358.25	—	—	—	—	—	—	—	—	—	—	—	—	—	—
	Cl	291,932.06	291,932.06	—	—	—	292,323.81	292,323.81	—	—	—	—	—	—	—	—	—	—	—	—	—	—
	Fe	2,754.28	2,754.28	—	—	—	3,062.54	3,062.54	—	—	—	—	—	—	—	—	—	—	—	—	—	—
	K	29,523.13	29,523.13	—	—	—	35,262.76	35,262.76	—	—	—	—	—	—	—	—	—	—	—	—	—	—
	Mn	3,446.81	3,446.81	—	—	—	3,446.81	3,446.81	—	—	—	—	—	—	—	—	—	—	—	—	—	—
	B	709.20	709.20	—	—	—	709.20	709.20	—	—	—	—	—	—	—	—	—	—	—	—	—	—
	$C_6H_5O_7$	—	—	—	8,426.28	—	825.61	825.61	—	—	—	—	—	—	—	—	—	—	—	—	—	—
	$K_3C_6H_5O_7{\cdot}H_2O$	—	—	15,873.38	—	—	—	—	—	—	—	—	—	—	—	—	—	—	—	—	—	—

Table 1 displays the overall flow summary table for the process. The inlet brine following silica and organics removal is contained in stream 1. Stream 1 is also used as the hot stream in heat exchanger H-101. Stream 2 represents the raw brine following the heat exchangers and before entering the additives mixing unit. Stream 3 contains the ferric chloride and tripotassium citrate monohydrate additives. Ferric chloride is required to add iron ions to enable maximum lithium adsorption in the packed bed reactor. Potassium citrate monohydrate is required to lower the standard potential of the redox shuttle within the brine so that adsorption favors the sorbent. This is further detailed in Section 4.3.2. Stream 4 contains the waste precipitate from mixing unit E-101. Stream 5 represents the makeup water required for cooling tower C-101. Stream 6 exits

the additive unit and enters the packed bed reactor network. Stream 7 contains the lithium-depleted brine which is sent back to the injection well.

Stream 8 represents the washing step performed after sorbent loading and after sorbent stripping. Section 4.3 details the reactors cycling through the following steps: a loading step, a washing step, a stripping step, and a second washing step. Stream 9 contains the makeup water added to ensure stream 6 remains constant. The washing water in stream 8 passes through a reverse osmosis unit (E-102) where the water is purified. Following this, some water is removed in stream 17, which is why stream 9 is required. Stream 10 represents the Lithium Pregnant Strip Solution (LiPSS) which exits the packed bed reactor network and enters each electrolyzer unit. Stream 11 represents stream 9 following an increase in temperature for use in electrolyzer E-103. Stream 12 represents the ferric chloride ($FeCl_3$) stripping solution recycle stream which exits the anode side of the electrolyzer units and is combined between the outputs of both electrolyzers. To maintain continuous processing, our design consists of four reactors and two electrolyzers. Stream 13 contains the makeup water required for cooling tower C-102. To prevent buildup of sodium in the recycled stripping solution, we added a purge to the flowsheet as represented by stream 14. To maintain the amount of stripping solution sent back to the reactors in the recycle stream, stream 15 contains a makeup $FeCl_3$ solution. Stream 16 represents the stripping solution entering the reactors for sorbent stripping following cooling tower C-102, the purge stream, and the added makeup $FeCl_3$ stream.

Stream 17, as mentioned above, represents the water removed from reverse osmosis, E-102, and added to the cathode side of the electrolyzer units. This stream represents the total input into both electrolyzer units. Stream 18 is a combination of the hydrogen gas emitted from both electrolyzer units. Stream 19 contains the LiOH product stream from the electrolyzer units that enters the evaporation and crystallization unit, E-105. Stream 20 represents the process condensate formed during evaporation of stream 19. Stream 21 represents the LiOH monohydrate product exiting the evaporation and crystallization unit.

4.1.1 Inlet Feed Composition and Conditions

The inlet brine will enter at a flow rate of 6,000 gallons per minute, or 1,637,000 kg/hr with a composition derived from measured feed stream concentrations to a Simbol pilot scale lithium extraction plant (Simbol, 2011).

Table 2. Concentrations of Synthetic Lithium Prize Brine (SLPB) Compared to Measured Concentrations of Simbol Feed Brine (SFB)

Constituent	SLPB mg/kg	SFB mg/kg	Difference %
Boron	430	432	-0.5%
Calcium	35,600	37,600	-5.3%
Chloride	177,000	165,000	7.3%
Iron	1,670	1,680	-0.6%
Potassium	17,900	18,900	-5.3%
Lithium	231	232	-0.4%
Manganese	2,090	2,100	-0.5%
Sodium	59,400	62,700	-5.3%
TDS	296,000	290,000	2.1%

Table 2 shows a breakdown based on the brine feed composition of the most prominent constituents. Only analytes in the Simbol Feed Brine (SFB) present in greater than 0.04 molal were represented in a Synthetic Lithium Prize Brine (SLPB), used for laboratory experimentation. The synthetic brine developed thus excludes trace elements including aluminum, ammonia, antimony, arsenic, barium, copper, fluoride, magnesium, silica, silver, sulfate, and strontium. Further inclusion of trace elements in the synthetic brine may allow for more accurate process design and scaling predictions, but this was not considered in this report. The following process design scope excludes pre-treatment steps toward silica removal and assumes that exclusion of these analytes will not significantly affect operations. We utilize the synthetic brine composition (SLPB) as our feed brine.

The point of brine reinjection underground currently occurring in Salton Sea geothermal plants is the point at which our lithium extraction process will be added. The brine will first flow from silica and inorganics removal, outside the scope of this design process, and then will be utilized in heat integration, Section 4.6.1.2, before recycling back to mixing unit E-101 for additive mixing. At the point the geothermal plant currently reinjects the brine, the brine is at 110°C and 1 atm. The brine at 110°C is utilized to heat the lithium rich stream before it enters electrolysis, Section 4.4. This process cools the brine to 86.25°C and it is recycled back the the beginning of the process; therefore, the brine inlet stream to the mixing unit is at 86.25°C. The

SLPB density was found to be 1.238 g/mL at 20°C, 1.226 g/mL at 45°C, and 1.219 g/mL at 70°C (A. Hawkins, personal communication, February 9, 2023). From linear extrapolation, the SLPB density at 86.25°C is taken to be 1.2103 g/mL, Appendix A.1. We recommend explicitly measuring the experimental brine at 86.25°C for greater accuracy.

4.2 Mixing Unit for Process Additives

4.2.1 Mass Balance Considerations

The diagram outlined below provides a close-up view into the stream around the mixing unit E-101.

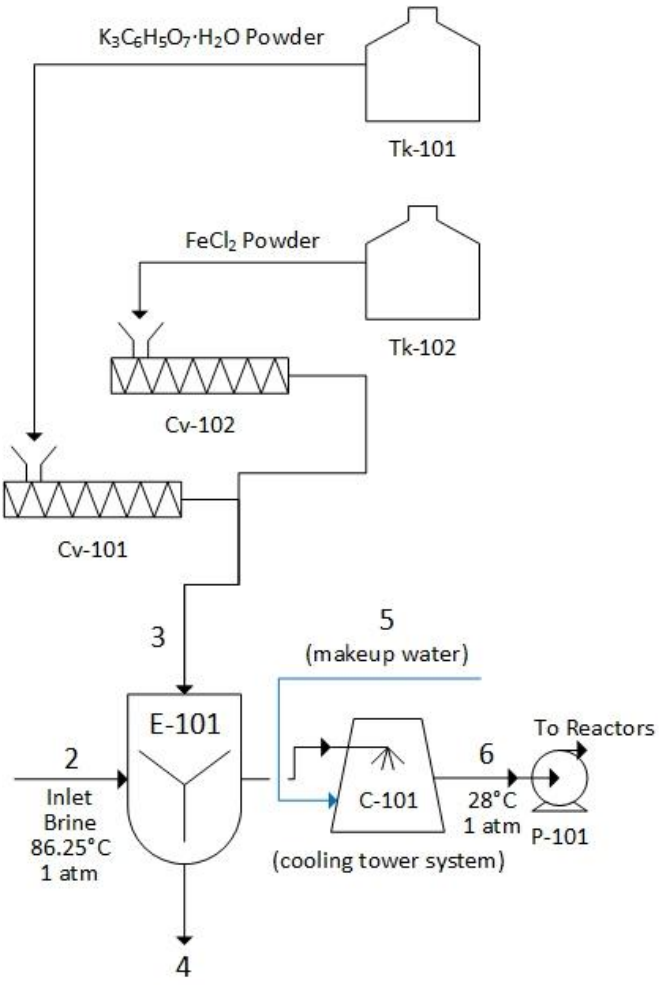

Figure 3. Close-Up Process Flow Diagram of Mixing Unit E-101

As shown in Figure 3, tripotassium citrate monohydrate ($K_3(C_6H_5O_7) \cdot H_2O$) is added prior to the cooling unit in a 1:1 stoichiometric ratio of citrate ion to iron in the brine. A screw conveyor, Cv-101, brings the tripotassium citrate monohydrate powder into mixing unit E-101. This addition decreases the standard potential of the redox shuttle below that of the sorbent material such that lithium adsorption occurs. Using the brine flow rate and assuming equimolarity with the brine iron content, $(C_6H_5O_7)^{3-}$ must be added at a rate of 9,250 kg/hr.

The electron transfer between the sorbent $Fe^{3+}PO_4(s)$ and brine containing $Fe^{2+}(aq)$ facilitates lithium adsorption. To capture the total amount of lithium present in the brine, iron must be present in the brine at a 1:1 molar ratio to lithium. $FeCl_2$ is thus added at a rate of 700 kg/hr which is the difference between the lithium and iron concentration present initially in the brine. Along with $K_3(C_6H_5O_7) \cdot H_2O$, the $FeCl_2$ is added to mixing unit E-101 using screw conveyor Cv-101.

The inlet brine is cooled to 28°C, the operational temperature of the Packed Bed Reactors (PBR), as $K_3(C_6H_5O_7) \cdot H_2O$, and $FeCl_2$ are mixed in E-101. This temperature was selected based upon the minimum temperature the brine can be cooled to from the 23°C Imperial County mean coincident wet bulb temperature and a minimum 5°C cooling tower approach. The solubility of calcium citrate tetrahydrate ($Ca_3(C_6H_5O_7) \cdot 4H_2O$), a byproduct of the mixing unit, is 1.83 g/liter water at 95°C as reported by Boulet and Marier (1960). The reported solubility at 95°C is assumed to be equivalent at 86°C and with additional ions present in solution. Appendix A.5 shows calculations for the predicted $Ca_3(C_6H_5O_7) \cdot 4H_2O$ scaling rate of 25,670 kg/hr. This is approximately 91% of the citrate initially added on a molar basis which is a significant process loss. We recommend further experimentation into the effect of citrate addition on the SLPB reduction potential. Should citrate addition not prove necessary, this would eliminate the calcium citrate tetrahydrate scaling problem.

The data collection for the lithium adsorption and desorption was taken at a system pH ranging from 3-5 at temperatures around 25℃ (G. Koenig, personal communication, January 20, 2023). We assume that the brine exiting the additive mixing unit is within operational range. We recommend further testing the effect of additives on brine pH. Further sorbent performance testing beyond the current pH range of 3-5 may also eliminate the need for pH balancing additives.

Table 3. Material Balance Around Mixing Unit E-101 (kg/hr)

Constituent	Stream 2 Inlet brine to E-101 (kg/hr)	Stream 3 $FeCl_2$ to E-101 (kg/hr)	Stream 3 $K_3C_6H_5O_7 \cdot H_2O$ to E-101 (kg/hr)	Stream 4 $Ca_3C_6H_5O_7 \cdot H_2O$ Precipitate from E-101 (kg/hr)	Stream 6 Outlet brine from E-101 (kg/hr)
H_2O	1,151,696.79	0	881.47	802.75	1,151,775.51
Li^+	380.99	0	0	0	380.99
Na^+	97,970.44	0	0	0	97,970.44
Ca^{+2}	58,716.27	0	0	5,358.03	53,358.25
Cl^-	291,932.06	391.76	0	0	292,323.81
Fe^{+2}	2,754.28	308.26	0	0	3,062.54
K^{+1}	29,523.13	0	5,739.63	0	35,262.76
Mn^{+2}	3,446.81	0	0	0	3,446.81
B^{+2}	709.20	0	0	0	709.20
$C_6H_5O_7^{-3}$	0	0	9,252.65	8,426.28	825.61

Converting to a molar basis and assuming a 6,000 gallon per minute inlet brine basis (Ventura et al., 2020, p. 2), Table 3 shows the inlet and outlet streams to E-101. Related calculations are in Appendices A.2. and A.3.

4.2.2. Energy Balance Considerations

The heat removal required to cool the brine solution from 86°C to 28°C is calculated with Equation 1:

$$Q = mC_p\Delta T \quad (1)$$

where m is the solution mass, C_p is the brine heat capacity, and ΔT is the brine temperature change. We assume that the heat capacity of the brine is equal to the heat capacity of water. Salt addition decreases the specific heat capacity of water, thus this estimation is the upper bound of heat removal requirement. We recommend calorimetric measurement of the brine heat capacity for greater accuracy. The calculated heat removal requirement is 111 MW, as calculated in Appendix A.6.

The enthalpy of solution of tripotassium citrate monohydrate is 7,087 J/mol (Apelblat, 1994). The molar flow rate of $K_3C_6H_5O_7 \cdot H_2O$ and enthalpy of solution corresponds to 0.096 MW being absorbed from $K_3C_6H_5O_7 \cdot H_2O$ dissolution, as referenced in Appendix A.7. The enthalpy of solution for $FeCl_2$ is 19.82 $\frac{kcal}{mol}$ (Cerutti & Helper, 1977). The heat released from ferric chloride dissolution is 0.138 MW, as shown in Appendix A.8. The heat of dissolution is thus considered negligible compared to the heat of the bulk solution. This means that the exit temperature of the stream coming out of the mixing unit can be assumed to be 86.25°C as it heads to the cooling tower. We recommend research efforts towards adsorption/desorption data collection at 85℃, as this is the optimal temperature for electrolysis and would eliminate the need for cooling towers.

4.2.3. Mixing Tank Design

The optimal dimensions for the $FeCl_2$ and tripotassium citrate monohydrate mixing tank are calculated with standard proportions as defined by McCabe (pg. 243).

Table 4. Sizing Parameters for Mixing Tank

Sizing	Length (m)
Height (H)	2
Tank Diameter (Dt)	2
Impeller Diameter (Da)	0.67
Impeller Length (L)	0.17
Impeller Width (W)	0.13
Baffle Width (J)	0.17
Distance from Base to Impeller (E)	0.67

Table 4 reflects the final sizing parameters of the mixing tank unit. The mixing tank is further constructed using four baffles and a six-blade propeller to reduce swirling by impeding rotational flow. A propeller agitator is selected given the low viscosity of the brine and it generates axial-flow in the mixing tank. A motor speed of 400 rpm is selected based on the range of larger propeller speeds from 400 to 800 rpm as recommended by McCabe et al. (1993, p. 237).

The Reynolds number is calculated near 2,000,000 using density and viscosity approximations for the brine data following reinjection using Equation 2.

$$Re = \frac{\rho N D^2}{\mu} \quad (2)$$

where ρ is the density of solution, N is the rotational speed, D is the impeller diameter and μ is the viscosity.

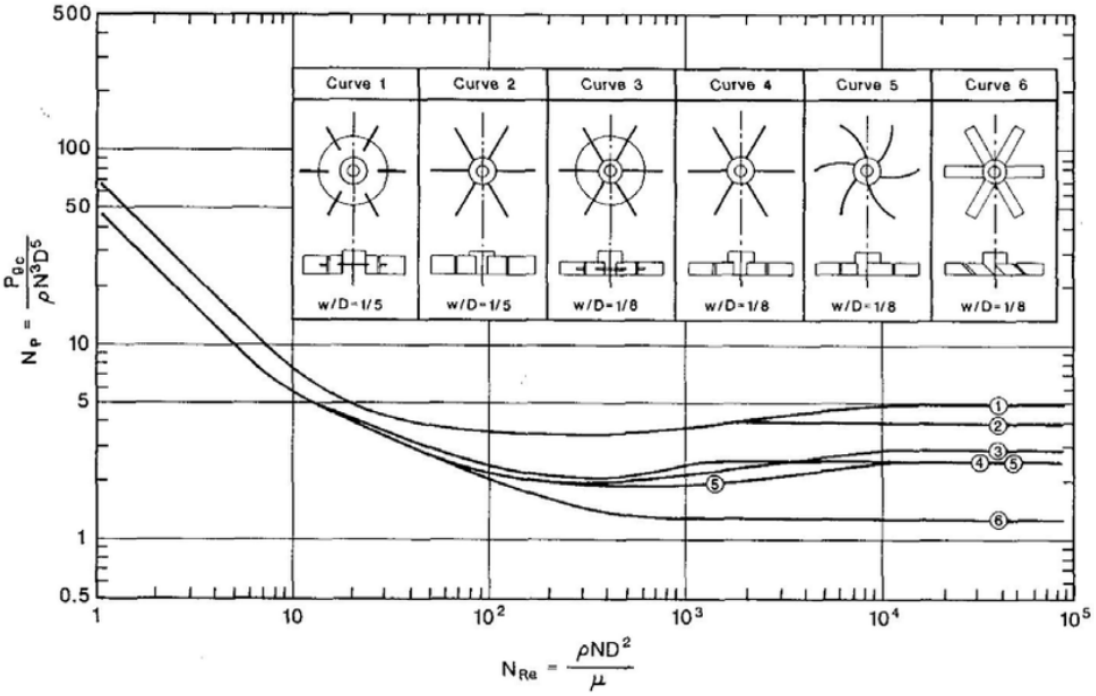

Figure 4. Power Number Vs. Reynold's Number for Various Impellers (Padron, 2001)

For the purposes of the calculation, the density of solution is approximated as the density of the brine at 86°C, the operating temperature of the mixing unit. The viscosity of solution is estimated using brine properties given the minimal amount of additional inputs into the mixing unit. Using this Reynold's number calculation, the power number was found using Figure 4 to ultimately determine the power requirements of the mixing unit.

A power number of 5.75 correlates to an overall power consumption of 0.27 MW, corresponding to curve 1 on Figure 4. The mean residence time was further calculated as 16.5 seconds using Equation 3, Appendix A.9.

$$\tau = \frac{V}{V_\circ} \quad (3)$$

where V is the volume of the reactor tank and V° is the volumetric flow rate. The calculated residence time will allow complete mixing of the citrate with the brine given the relatively non-viscous nature of the solution .

4.3 Packed Bed Reactor Network

The packed bed reactor network is the second stage of the design. The brine, containing a low concentration of lithium ions, is converted into a solution with a higher lithium chloride concentration. This is achieved using a Iron (III) Phosphate sorbent material that selectively adsorbs lithium ions from the brine. This stage progresses through four phases: sorbent loading, washing, sorbent stripping and washing again. Limited information is known about the sorbent material including heat of reaction, reaction behavior at different temperatures and diffusion properties. The assumptions and design parameters for the reactors are detailed in this section.

4.3.1 Sorbent Material & Electron Exchange Reactions

In the reactor network, the sorbent material Iron (III) Phosphate ($FePO_4$) is used to extract lithium (Li^+) using consecutive adsorption and desorption schemes. The overall reaction is listed below as Equation 4 and can be run in either direction. Charged states for the iron in the phosphate complex are included for reference. The sorbent is iron phosphate ($FePO_4$) in its oxidized state and lithium iron phosphate ($LiFePO_4$) in its reduced state.

$$Fe^{3+}PO_4(s) + Fe^{2+}(aq) + Li^+(aq) \rightleftharpoons LiFe^{2+}PO_4(s) + Fe^{3+}(aq) \quad (4)$$

Adsorption or desorption mechanisms are selected by modifying Fe^{2+}/Fe^{3+} and citrate ion concentrations. Both reactions begin with an electron transfer step. This step is favorable depending on the chemical potential of the solution, which is calculated in Section 4.3.2. All species present are ionic components so the products are converted from the reactants using charge balancing ions that offset the charge difference resulting from the electron transfer.

The adsorption reaction is detailed using Equation 5 representing the deposition of lithium and the reduction of Iron Phosphate (FP). FP is selected for its high selectivity for lithium over other cations such as sodium or potassium. The electron being transferred originates from the $Fe^{2+}(aq)$ in the brine and is accepted by the Fe^{3+} in the FP. The resulting solid complex contains PO_4^{3-} and Fe^{2+}. A Li^+ ion is thus absorbed to reestablish charge neutrality. The resulting Fe^{3+} in the brine is reinjected leaving lithium chemically absorbed into the FP framework.

$$Fe^{3+}PO_4(s) + Fe^{2+}(aq) + Li^+(aq) \rightarrow LiFe^{2+}PO_4(s) + Fe^{3+}(aq) \quad (5)$$

Desorption is summarized using Equation 6 below. Fe^{3+} is introduced into the system using aqueous Ferric Chloride ($FeCl_3$) which changes the ratio of Fe^{3+}:Fe^{2+} ions that in turn changes the chemical potential of the solution. An electron is transferred from the LFP to the Fe^{3+} due to this potential difference. The solid then contains PO_4^{3-}, Fe^{3+} and Li^+ with an overall +1 charge. To restore electroneutrality, the Li^+ is ejected into solution and forms an ionic bond with a chlorine ion from the $FeCl_3$ solution. This LiCl is represented below with the unbonded Li^+ to show the charge transfer between species, but the solution leaving the bed is neutral and contains ionic bonds between the charged species.

$$LiFe^{2+}PO_4(s) + Fe^{3+}(aq) \rightarrow Fe^{3+}PO_4(s) + Fe^{2+}(aq) + Li^+(aq) \quad (6)$$

4.3.2 Favorability of Reactions

The favorability of a reaction is related to the change in enthalpy, change in entropy and the temperature at which the reaction occurs. There is limited knowledge of the adsorption and desorption thermodynamics of the iron phosphate and lithium iron phosphate interacting with the iron solutions and lithium. This section will prove that both of these reactions are favorable by estimating the change in gibbs free energy using the chemical potential of the solution. This is reasonable because the first step in both reaction mechanisms is electron transfer. If the electron transfer is favorable, the second step, either lithium adsorption or desorption, will be favorable. This is assumed due to the high potential that exists when systems are not electrically neutral.

4.3.2.1 Adsorption

The standard potential $E_{0,cell}$ for the adsorption cell is calculated. The standard potential for FP/LFP is constant at 0.41V vs the standard hydrogen electrode (SHE) with very low fluctuation due to system conditions (Gupta et al., 2022). The standard hydrogen electrode is a common zero voltage reference point for half cell potentials; the potential for each half cell is calculated with respect to the voltage required to atomize hydrogen. The standard potential for the oxidation half cell of 0.244V vs SHE is referenced from Wen et al. (2006) and refers to $Fe^{2|3+}$ with a citrate additive. This decreases the potential of the $Fe^{2|3+}$ solution and makes electron transfer from the brine containing Fe^{2+} to the FP favorable. Thus $E_{0,cell}$ is positive at 0.166V using Equation 7.

$$E_{0,cell} = E_{0,red} - E_{0,ox} \quad (7)$$

where $E_{0,red}$ is the reduction potential and $E_{0,ox}$ is the oxidation potential.

To account for the high concentration of Fe^{2+} ions in the brine, the Nernst equation is used to find the cell potential as a function of the reaction quotient, Q. The Nernst equation is shown below as Equation 8. Q is equal to the concentration of products divided by the concentration of reactants. The concentration of solid material, FP and LFP, is set equal to unity since it is independent of conditions. A 99:1 ratio of Fe^{2+} to Fe^{3+} in the brine is assumed to resemble the brine composition provided without dividing by zero. The non-standard cell potential is 0.284V, making the electron transfer more favorable.

Gibbs Free Energy released through this adsorption scheme is found using Equation 9, below. It was calculated to be -27.42 kJ/mol which is exothermic and favorable.

$$E_{cell} = E_{0,cell} - \frac{0.052 * log(Q)}{n} \qquad (8)$$

$$\Delta G = -nFE_{cell} \qquad (9)$$

where n is the number of moles of electrons, F is the Faraday constant, and E_{cell} is the cell potential.

The equilibrium constant is calculated using Equation 10. A large, negative ΔG corresponds to a high equilibrium constant, K_{eq}. The equilibrium constant was found to be around 64,000, which is much greater than one, meaning the products of the adsorption reaction are heavily favored.

$$\Delta G = -RT\ln(K_{eq}) \qquad (10)$$

where R is the universal gas constant, T is the temperature, and K_{eq} is the equilibrium constant.

4.3.2.2 Desorption

The standard potential for the desorption reaction is calculated, as well as the change when the reaction quotient, Q, is not unity. The value for FP/LFP standard potential remains constant from Section 4.3.2.1 as cited in Gupta et al. (2022). The standard potential for $Fe^{2|3+}$ has been referenced from the standard cell potential table as 0.77V (URI Chemistry Department). This creates a cell with a potential of 0.36V.

The Nernst Equation is used again to account for differences with high concentration Fe^{3+} ions in the Ferric Chloride stripping solution. The reaction quotient, Q, is found to flip with respect to $Fe^{2|3+}$ but the concentration in the stripping agent is assumed to be the opposite ratio: 99:1 Fe^{3+}:Fe^{2+}. The high Fe^{3+} concentration is reasonable since the $FeCl_3$ will favor the Fe^{3+} state. The non-standard cell potential from the Nernst equation is 0.478V, more positive and favorable. The ΔG calculated with Equation 9 was -46.141 kJ/mol, larger than the adsorption potential. This is reflected further in the equilibrium constant, found using Equation 10, which is 122,000,000. This strongly favors the product of the desorption reaction meaning the lithium ejection from the LFP will occur in the desorption conditions of the packed bed.

4.3.3 Lithium Loading & Schedule

The maximum amount of lithium in the bed is related to bed volume and density of lithium sites in the sorbent. The achieved amount of lithium in the bed is found using the concentration of lithium in the brine and the length of adsorption cycle. The calculations for these values are detailed in this section and parameters are defined in Appendices B.1-B.3.

To find bed volume, the diameter and length must be calculated. The diameter of the bed can be found using the set input flow rate of the brine of 6,000 gallons per minute, V_{in}, and the selected superficial velocity, $0.15\frac{m}{s}$, u_0 (McCabe et al., 1993, p. 812). The diameter with these specifications was 1.79m using Equation 11.

$$d_{bed} = 2 * \sqrt{\frac{V_{in}}{u_0 * \pi}} \quad (11)$$

The length of the bed was set using a maximum pressure drop of 10 bar, recommended by McCabe et al. (1993), and the Ergun equation, Equation 12 below. The pressure drop is inversely proportional to length of bed and is a function of fluid viscosity μ, porosity ε, particle diameter d_p, fluid density ρ and superficial velocity u_0. These parameters can be found in Appendix B.3. The length of bed with this pressure drop was found to be 3.6 m.

$$\frac{\Delta P}{L} = \frac{150\mu(1-\varepsilon)^2 u_0}{\varepsilon^3 d_p^2} + \frac{1.75(1-\varepsilon)\rho u_0^2}{\varepsilon^3 d_p} \quad (12)$$

The lithium capacity per volume of sorbent can be calculated using the density of the sorbent ρ_ρ, porosity of the bed ε, and the maximum ratio of lithium to sorbent material in grams W_{sat}. The lithium capacity was calculated to be 76 kilograms Li/m^3 of bed using Equation 13.

$$\rho_{Li} = \rho_\rho * \varepsilon * W_{sat} \qquad (13)$$

The volume of a cylindrical bed with a diameter of 1.79m and length of 3.6m is 9.06m^3. This correlates to 691 kilograms of lithium in the bed at full capacity.

The input concentration of lithium in the brine is set at 231 mg/kg brine using the simulated brine composition provided in the DOE competition. This is equivalent to 381 kilograms of lithium entering the bed per hour. A 1% lithium loss to reinjection was assumed. Thus, 377 kilograms is adsorbed, equal to 54.6% of sites being occupied. An adsorption period of one hour was found to be ideal for a four hour cycle containing both adsorption and desorption. Using the input flow rate V_{in}, lithium fed to the bed m_{Li}, and adsorption period t, the inlet lithium concentration c_0 can be found. The relation is detailed in Equation 14 below. The inlet concentration of lithium is 0.279 g Li/m^3.

$$m_{Li} = c_0 * V_{in} * t \qquad (14)$$

The adsorption and desorption processes happen in the same reactor, but have different solution flows through the bed. The superficial velocity for adsorption and desorption is 0.15 m/s and 0.065 m/s, respectively. The difference in superficial velocity is driven by the difference in molar flow rate between the inlet stream in adsorption versus desorption. The brine flows at a rate of 1,639,000 kg/hr into the packed bed reactor for adsorption and only 38,441.4 kg/hr of ferric chloride was needed to react with the lithium and form lithium chloride. Thus, the amount of time spent in the reactor for both liquid feeds vary significantly.

To minimize the difference in linear velocities for adsorption and desorption, water is added to form a feed stream of aqueous ferric chloride that is approximately half of the molar flow rate of the inlet brine utilized in the stripping process. Based on the bed length of 3.6m, the ferric chloride will take twice as long to pass through the reactor for desorption in comparison to the brine during adsorption. The relationship between time spent in the reactor based on the superficial velocity and height is outlined below in Equation 15.

$$t = \frac{h}{u_0} \qquad (15)$$

Hour	PBR 1	PBR2	PBR3	PBR4	Brine Into	LiPSS to EC1	LiPPS to EC2
0.5	Loading	x	x	x	PBR 1	x	x
1		x	x	x	PBR 1	x	x
1.5	Washing	Loading	x	x	PBR 2	x	x
2	Stripping		x	x	PBR 2	PBR 1	x
2.5		Washing	Loading	x	PBR 3	PBR 1	x
3		Stripping		x	PBR 3	PBR 1	PBR 2
3.5			Washing	Loading	PBR 4	PBR 1	PBR 2
4	Washing		Stripping		PBR 4	PBR 3	PBR 2
4.5	Loading			Washing	PBR 1	PBR 3	PBR 2
5		Washing		Stripping	PBR 1	PBR 3	PBR 4
5.5	Washing	Loading			PBR 2	PBR 3	PBR 4
6	Stripping		Washing		PBR 2	PBR 1	PBR 4
6.5		Washing	Loading		PBR 3	PBR 1	PBR 4
7		Stripping		Washing	PBR 3	PBR 1	PBR 2
7.5			Washing	Loading	PBR 4	PBR 1	PBR 2
8	Washing		Stripping		PBR 4	PBR 3	PBR 2
8.5	Loading			Washing	PBR 1	PBR 3	PBR 2
9		Washing		Stripping	PBR 1	PBR 3	PBR 4
9.5	Washing	Loading			PBR 2	PBR 3	PBR 4
10	Stripping		Washing		PBR 2	PBR 1	PBR 4
10.5		Washing	Loading		PBR 3	PBR 1	PBR 4
11		Stripping		Washing	PBR 3	PBR 1	PBR 2
11.5			Washing	Loading	PBR 4	PBR 1	PBR 2
12	Washing		Stripping		PBR 4	PBR 3	PBR 2

Figure 5. Schedule for Four Packed Bed Reactor Network

The entire adsorption and desorption cycle takes four hours with 30 minutes for washing after the loading and stripping periods. The schedules for each of the four reactors is shown above on Figure 5, as well as where the input brine and outlet lithium pregnant stripping solution LiPPS are going to provide continuous processing. The LiPPS alternates between two electrolysis cells, EC1 and EC2; the design of these cells will be discussed in Section 4.4.

During washing, five bed volumes of water are fed through the system to remove any non-chemically adsorbed material (Majors, 2003). This corresponds to a water flow rate of 43,416 kg/hr for both washing steps in the 4 hour period. In our process, we assume there will be no ions remaining in the interstitial sites; however, we include a washing step to account for this possibility in physical designs. A diagram is outlined below along with a material balance around the regenerative network:

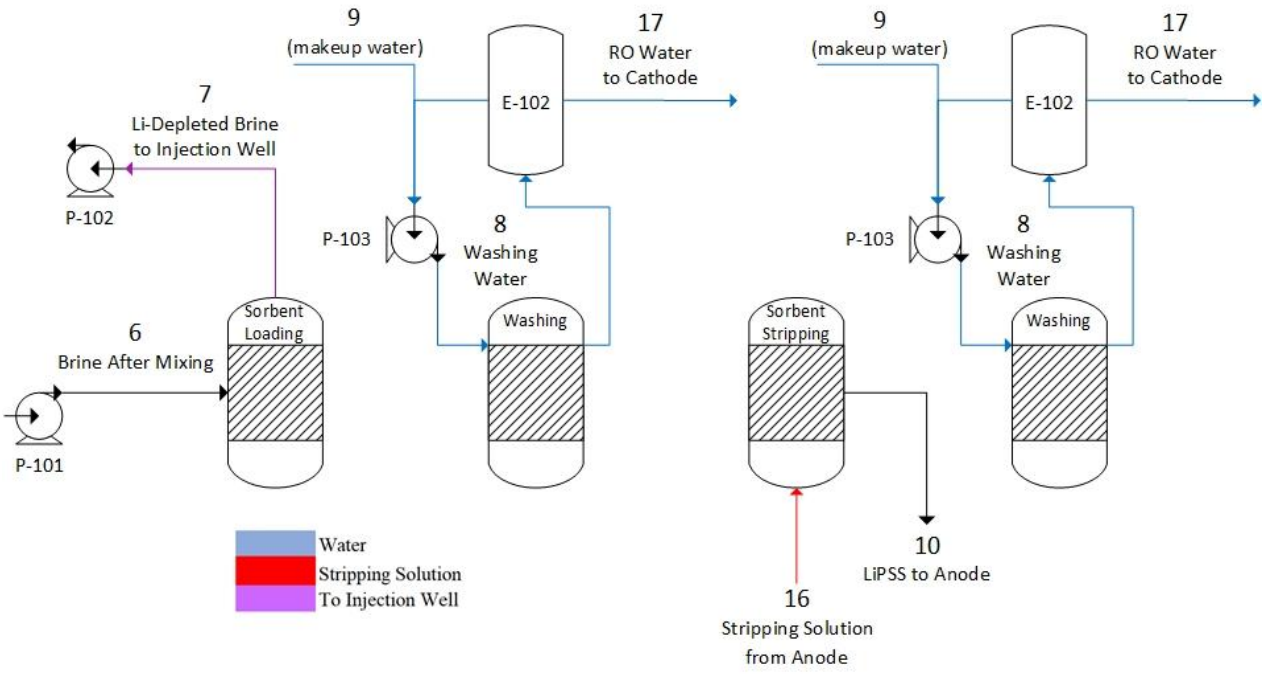

Figure 6. Close-Up Process Flow Diagram of the Reactor Regeneration Stages

Table 5. Flow Summary Table for Reactor Regeneration

Stream		6	7	8	9	10	16	17
Temperature (°C)		28	28	25	25	28	28	25
Pressure (atm)		1	1	1	1	1	1	1
Mass Flow (kg/hr)		1,634,134.30	1,633,744.43	43,446.78	11,452.63	340,646.47	680,900.39	11,452.63
Component Flow (kg/hr)	H_2O	1,151,775.51	1,151,775.51	43,446.78	11,452.63	335,980.92	671,961.83	11,452.63
	LiCl	—	—	—	—	1,152.82	—	—
	Li	380.99	3.50	—	—	—	—	—
	$FeCl_2$	—	—	—	—	3,469.95	—	—
	$FeCl_3$	—	—	—	—	—	8,880.81	—
	NaCl	—	—	—	—	42.78	57.75	—
	Na	97,970.44	97,958.06	—	—	—	—	—
	Ca	53,358.25	53,358.25	—	—	—	—	—
	Cl	292,323.81	292,323.81	—	—	—	—	—
	Fe	3,062.54	3,062.54	—	—	—	—	—
	K	35,262.76	35,262.76	—	—	—	—	—
	Mn	3,446.81	3,446.81	—	—	—	—	—
	B	709.20	709.20	—	—	—	—	—
	$C_6H_5O_7$	825.61	825.61	—	—	—	—	—

Figure 6 shows a close-up of the adsorption/desorption cycle with the corresponding flow rates outlined in Table 5. We did not design the reverse osmosis unit, E-102, due to the lack of data on the outlet wash stream. Thus, for material balances, we assumed there are no ions in the wash stream leaving the reactor. However we included the reverse osmosis unit in the PFD for future design considerations. Stream 16 represents the stripping solution sent to two reactors

while stream 10 represents the LiPSS leaving one reactor. Some sodium is adsorbed to the bed during sorbent loading which is later stripped and added to the LiPSS in stream 10. Sodium is also recycled through the stripping solution, as detailed in section 4.4.6. Thus, the total sodium entering the reactors is 57.75 kg/hr and the total sodium leaving the reactors during stripping is 85.56 kg/hr.

4.3.4 Heat Balance Considerations

The heat of adsorption and desorption are difficult to calculate since no pertinent experimental data for change in entropy for the reaction is available. This would enable the Gibbs Free Energy to be related to heat of reaction. To prove that the heat generated during adsorption is negligible compared to the flow rate of water, the maximum heat of chemisorption is assumed for the reaction. According to Adeleke et al. (2019), chemisorption heat of reaction ranges between 200-400kJ/mol. Thus, a value of 400kJ/mol is used for these calculations to represent the most conservative case. This level of heat release corresponds to low fractional coverage, meaning high uptake and early stages of adsorption. These calculations assume a 400kJ/mol chemisorption heat of reaction is maintained for the entire hour adsorption period and two hour desorption period, which is also conservative as rates slow as the bed is filled or depleted.

For adsorption, the brine flow rate is 1,620,000 kg/hr, and the heat capacity is approximated as pure water. Assuming 100% of possible sorbent sites absorb a lithium ion, much higher than the 54.6% calculated in Section 4.3.3, 687,000 kg of lithium are involved in this reaction, M_{Li}. This overestimate for heat released from the reaction and moles involved would raise the brine 5.729 °C, using Equation 16. A negative value for dT indicates the final temperature of the solution is higher than the initial before the reaction. The actual brine temperature increase will be lower than this value due to the conservative nature of the assumptions.

$$M_{Li} * \Delta h = m_{brine} * c_p * \Delta T \quad (16)$$

where Δh is the heat of reaction, m_{brine} is the mass of the brine, c_p is the heat capacity, and ΔT is the temperature change.

For desorption, the solution flow rate for 0.095 M $FeCl_3$ stripping solution is 165 kg/hour with a heat capacity of 3.74J/gK found using OLI Studio simulation. All of the sites are assumed to participate in the reaction and a heat of desorption is assumed to be equal to the maximum value identified for adsorption, -400kJ/mol. According to Tetenoire, Juaristi & Alducin (2021), classification of desorption as exothermic can be achieved using desorption potential. They relate desorption potential to the system energy when the adsorbed material is in either the solid or vacuum. If the system potential is lower when the adsorbed material is in the vacuum, the desorption can be considered exothermic. These potentials can be approximated using the chemical potentials from Section 4.3.2, thus the desorption process can be assumed to be exothermic.

Equation 16 is used with the new m_{brine} and c_p and constant M_{Li} and Δh_{rxn}. These conservative estimates predict the brine temperature will increase by 8.98°C if the highest rate of desorption is maintained for the entire two hour desorption period.

Research into the sorbent material by Gupta et al. (2022) found no noticeable molar conversion change within a system temperature range of 22.4-40°C. The initial temperature of the brine and stripping solution are 28°C. Increases in solution temperature by 5.729 and 8.98°C, to 33.729 and 36.98°C, still maintain solution temperatures within the range studied in the paper that are identified to conduct the same sorption nature.

4.3.5 Equilibrium Considerations

Pertinent kinetic data is unavailable for the system being designed, so a few points must be discussed to account for kinetic limitations. Two assumptions are proved using the equilibrium constant: highly favorable reaction products and, thus, irreversible adsorption. The magnitude of the equilibrium constant for adsorption is $6.4*10^4$, much greater than one. This proves that the forward reaction is highly favorable. Irreversibility is demonstrated using the shape of the Langmuir Isotherm which is defined below in Equation 17.

$$q = \frac{q_{max} * K_{eq} * c_{A,solution}}{1 + K_{eq} * c_{A,solution}} \quad (17)$$

where q_{max} is the maximum adsorption capacity, K_{eq} is the equilibrium constant, and $c_{A,solution}$ is the concentration of solute in solution.

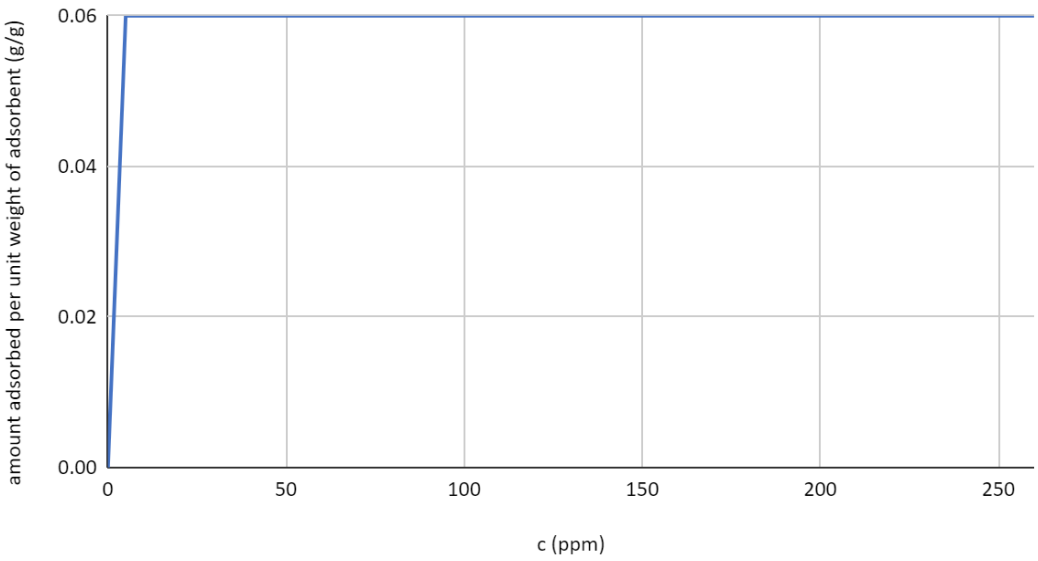

Figure 7. Adsorption Isotherm using Equation 17, amount adsorbed per unit weight of adsorbent (g/g) vs. c (ppm)

Graph of the amount adsorbed per unit weight of adsorbent, q, versus solution concentration, $c_{A,solution}$ is above, Figure 7, representing the adsorption isotherm for this reaction's thermodynamic quantities.

The shape of the adsorption isotherm is known as rectangular. This is represented by the sharp increase in maximum fraction adsorbed on the surface even at low concentrations in the solution. Rectangular langmuir isotherms are correlated with irreversibility for the adsorption reaction (Ruthven, 2000).

Due to the lack of relevant experimental relations describing desorption as a function of equilibrium parameters, the desorption isotherm is assumed to mirror that of adsorption. The desorption reaction also has an extremely high equilibrium constant of $1.22*10^8$, much greater than one, so the system will strongly favor the desorbed state. The desorption rate is proportional to the concentration of the adsorbed material in the solution (Azizian et al., 2018). These qualities enable the assumption that the desorption rate will mirror the high rate of adsorption when initial conditions are present. For adsorption, initial conditions are present when the surface lithium concentration is lowest; for desorption, initial conditions are present when the solution concentration of lithium is lowest. Initial conditions, and thus high sorption rate, will first be localized to the beginning of the bed. The high sorption rate will move down the bed over time as lithium transfer will exhaust the sites at the beginning of the bed.

4.3.6 Diffusion Considerations and Modelling

The relative importance of internal and external mass transfer resistances can be expressed in terms of the Biot number. In both adsorption and desorption processes, the Biot number was calculated as several orders of magnitude greater than one. This means the internal resistance will be dominant. The intra-pore diffusion will dominate over diffusion through the bulk solution so diffusion models must consider sorption within the pores of the FP/LFP particles.

The rectangular isotherm, described in Section 4.3.5, allows simplifications in modeling for both adsorption kinetics and diffusion. In the adsorption reaction being modeled in this reactor, diffusion is the limiting factor as the "rate-limiting step in electrochemical investigations has been Li+ diffusion-controlled phase boundary movement" (Gupta et al., 2022). By assuming equilibrium is reached moving down the bed, uptake into the bed can be approximated as instantaneous.

Brauch and Schlunder derived a dimensionless solution for the adsorption rate into activated carbon columns in their 1975 paper. Their solution is recognized for its applicability to rectangular adsorption isotherms with dilute aqueous solutions and high accuracy when compared to experimental data (Ruthven, 2000). The solution approximates the diffusive conditions with the Shrinking Core Model, where the diffusion in the system is limited in the external layer of the particle with a rapid reaction. The reaction moves into the particle as surface sites are exhausted. Brandabi (2020) cites these simplifications and the corresponding application of the numerical solution as a "reasonable model for liquid phase systems with chemisorption". Gupta (2022) identifies that the similar adsorption reaction between LFP and ferrocyanide is speculated to "follow a shrinking core process with regards to the LFP aggregate particles". With these considerations, the shrinking core model and the dimensionless solution from Brauch and Schlunder was selected to best model the diffusivity of the adsorption and desorption reactions in the packed bed reactors.

The numerical solution is presented with respect to grams of carbon sorbent in the column; this is replaced with grams of iron phosphate. The solution is further categorized by Biot number magnitudes. The Biot number for adsorption is 1,500,000 and the Biot number for desorption is 7,350,000, with calculations shown in Appendix B.10-B.11. These are approximated as infinity compared to the scale of values considered in the solution (2, 20 and infinity).

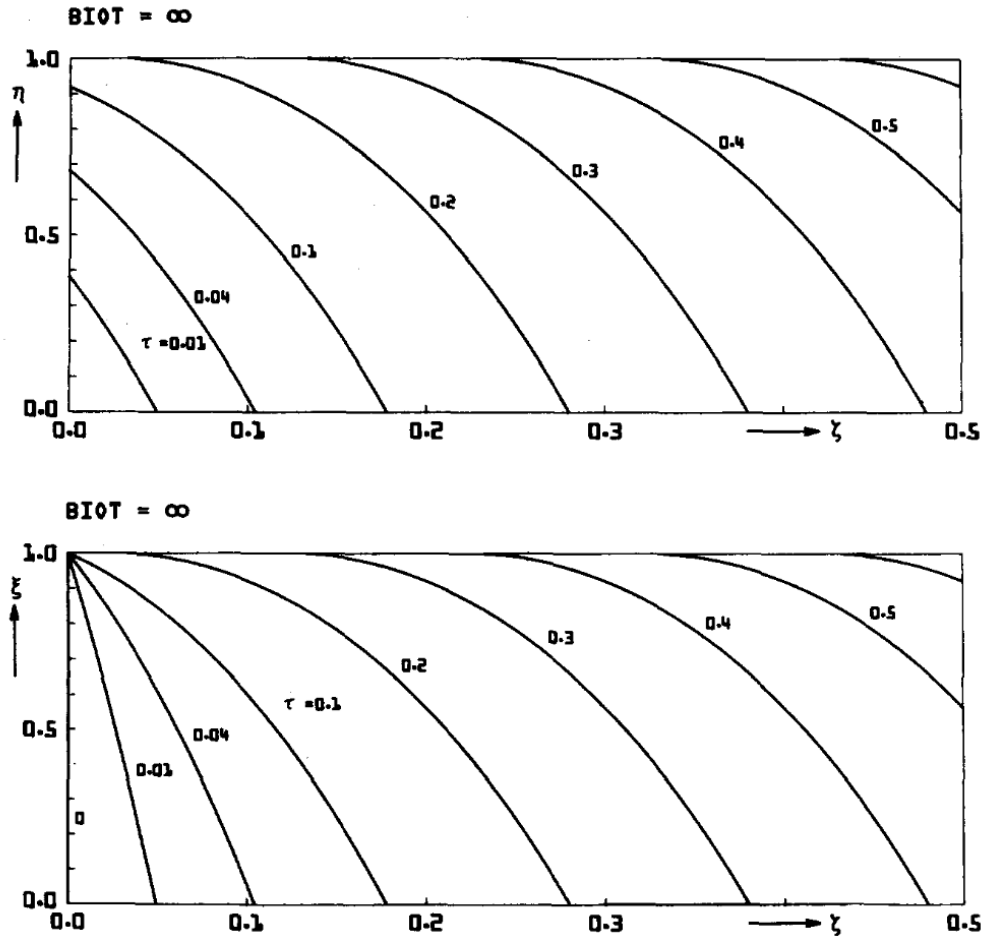

Fig. 15. Solid-concentration η and liquid-concentration ξ vs bedlength; Biot = ∞.

Figure 8. Dimensionless Numerical Solution for Adsorption Beds (Brauch and Schlunder, 1975)

Figure 8 was used along with the dimensionless groups bed length (ς), time (τ), solid phase concentration (η) and liquid phase concentration (ξ). The top plot in Figure 8 is dimensionless solid concentration and the bottom plot is dimensionless liquid concentration. Bed length is a function of sorbent mass, flow rate, maximum bed length, sorbent density, particle diameter, effective diffusivity and distance coordinate of measurement. Dimensionless time is a function of effective diffusivity, particle diameter, initial liquid concentration, sorbent density, maximum solid phase concentration, and time. Dimensionless solid phase concentration is proportional to mean solid phase concentration over theoretical solid phase concentration at equilibrium. Dimensionless liquid concentration is proportional to liquid phase concentration over

inlet solution concentration. Equations for these groups are in Appendix B.6 and values used for adsorption and desorption are in Appendix B.7.

4.3.6.1 Adsorption Model

The sorbent for adsorption is iron (III) phosphate, the adsorbed material is lithium ions and the diffusion is limited by Fe^{2+}. The Fe^{2+} is the species that donates an electron, creating a charge imbalance. Diffusion of the iron (II) citrate is the focus of the numerical model and the lithium adsorption is assumed to be electrostatically driven due to the charge in the iron phosphate after electron transfer. The graphs are shown with respect to lithium concentration as the lithium is what adsorbs as a result of the Fe^{2+} diffusion.

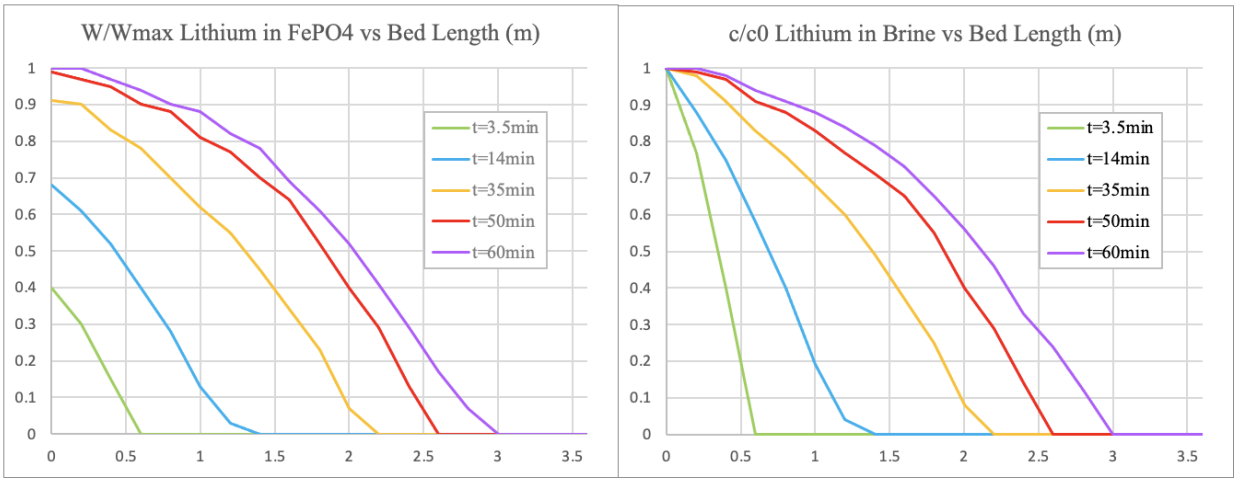

Figure 9. Uptake of Lithium into Sorbent (left) and Depletion of Lithium in Brine (right)

Figure 9 shows the concentration of lithium in both the sorbent, iron phosphate, (left) and the brine (right). The bed length is set at 3.6 m, described in Section 4.3.3. The variables W and W_{max} represent the entrained concentration and the maximum entrained concentration allowed by the sorbent, respectively. The variables C and c0 are the concentrations of lithium in the solution and the initial concentration entering the bed, respectively. Non-normalized profiles can be found in Appendix B.7. These profiles can be integrated to find the mass of lithium deposited. Since a 1% lithium reinjection rate was assumed and no other lithium breaks through, the adsorbed mass of lithium is equal to the inlet mass flow entering the bed per hour multiplied by 0.99 to give 377 kg of lithium.

Assuming a 100:1 molar selectivity of the iron phosphate towards lithium over sodium, the amount of sodium in the bed after one hour is 0.99 mol percent of the lithium adsorbed. This is equal to 12.3 kg Na. This mass of sodium is approximate because the lithium and sodium will directly compete for adsorption sites, yet this diffusion model assumes all sites are occupied by lithium. Because of the small percentage of sodium captured in the bed, is it assumed that all input lithium will still be adsorbed and the sites filled by sodium are in addition to what is calculated by the model.

4.3.6.2 Desorption Model

The sorbent material for the desorption model is lithium iron phosphate (LFP), the desorbed material is lithium ions, and the diffusion is limited by Fe^{3+} ions as the electron acceptor. Iron phosphate (FP) is used in place as the sorbent so that given data for sorbent quantity and maximum lithium entrainment can be utilized. FP material properties are a reasonable approximation for LFP due to their similar chemical composition. The model also assumes the maximum concentration of lithium in the stripping solution is equal to the molarity of ferric chloride since they interact 1:1 stoichiometrically. An updated effective diffusivity coefficient and volumetric flow rate for two hours through the bed are used. Values can be found in Appendix B.7.

No separate numerical solution was found for desorption isotherms, so it was assumed to have the same iron transfer properties as adsorption for simplicity. The change in solution composition in the desorption model is used to represent the $FeCl_3$ interacting with lithium entrained in the bed. In the graphs below, concentration of lithium desorbed predicted by the model is approximated as sites from which the $FeCl_3$ has transferred an electron. The Fe^{3+} ion is in $FeCl_3$ that has not stripped a lithium atom through electron transfer. The numerical solution is shown with respect to the Fe^{3+} concentration since it is inversely related to lithium concentration.

As concentration of Fe^{3+} is depleted, lithium is released from the bed. The Fe^{3+} saturation farther down the bed after longer times is a side effect of the model and is made up of sites the excess $FeCl_3$ could interact with that contain no lithium. If no lithium is entrained in the bed at a specific site, the $FeCl_3$ will just move onto the electrolyzer without electron transfer. The model shows these Fe^{3+} ions being converted to Fe^{2+} regardless.

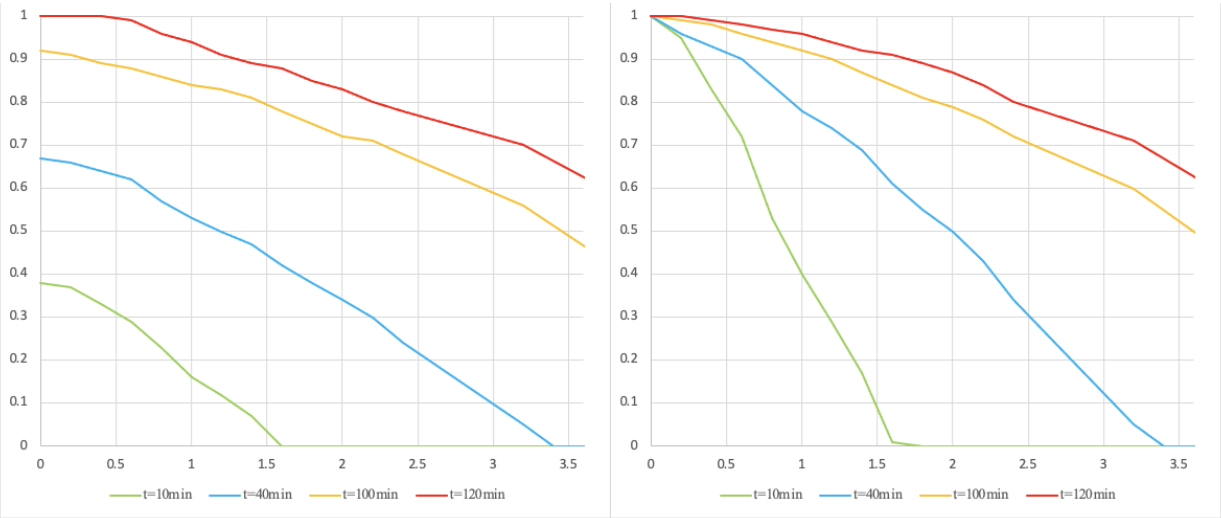

Figure 10. Modified Adsorption Profiles using Desorption Dimensionless Groups.
(Left) W/W_{max} Fe^{3+} in $FePO_4$ vs Bed Length (m)
(Right) c/c0 Fe^{3+} in Solution vs Bed Length (m)

The profiles above show that within the two hour desorption period, the ferric chloride stripping solution is able to saturate most of the bed; this section includes all of the sites that contain a lithium ion adsorbed. Non-normalized versions of Figure 10 can be found in Appendix B.9. Saturation refers to the $FeCl_3$ diffusing to the LFP sites where the electron transfer can occur. Excess saturation is possible because $FeCl_3$ is fed in stoichiometric excess of 1.95:1 moles $FeCl_3$: moles entrained Li to account for desorption efficiency. The saturated part of the bed after two hours is similar in shape to the final adsorption saturation volume, so all occupied lithium sites are assumed to be released.

Only 54.6% sites participate in the adsorption reaction, so the bed is not full of lithium. The time it takes for all of the entrained lithium to be released by the $FeCl_3$ and leave the bed can be approximated. On the left of Figure 10, the graph of sites used over sites available can be integrated to determine the percent of the used bed. The yellow curve can be approximated with a 2^{nd} degree polynomial fit to find the percentage of filled sites. The curve fit is shown in Appendix B.12. The units for area percentage are the boxes on the graph. The total area of the graph is 3.6 units squared, and the yellow curve bounds 73.9% of this area. Thus after 100 minutes, ~74% of sites can be desorbed. All lithium can be approximated as removed at this time; all $FeCl_3$ fed after this point is in excess.

This approximate desorption model enables the assumption that all entrained lithium is stripped from the bed. The amount of moles of lithium entering the packed bed network is thus equivalent to the amount of lithium entering the electrolysis cells. The 1.95:1 stoichiometric excess of ferric chloride enables the assumption that enough stripping solution is fed to free all entrained sodium as well, so all entrained sodium is also fed to downstream processing.

Table 6. Final Operating Conditions for a Packed Bed Reactor

Parameter	Value
Temperature	28 °C
Pressure	1 atm
Superficial Velocity	0.15 m/s^2
Bed Volume	9.06 m^3
Lithium Adsorbed	377 kg
Sodium Adsorbed	12.3 kg
Adsorption Cycle	1 hour
Desorption Cycle	2 hours

Table 6 summarizes the operating conditions of a packed bed reactor.

4.4 Electrolysis

4.4.1 Reactions in the Electrolyzer

The aqueous inlet feed into the electrolyzer unit from the packed bed reactor system contains LiCl, NaCl, $FeCl_2$, $FeCl_3$, and H_2O.

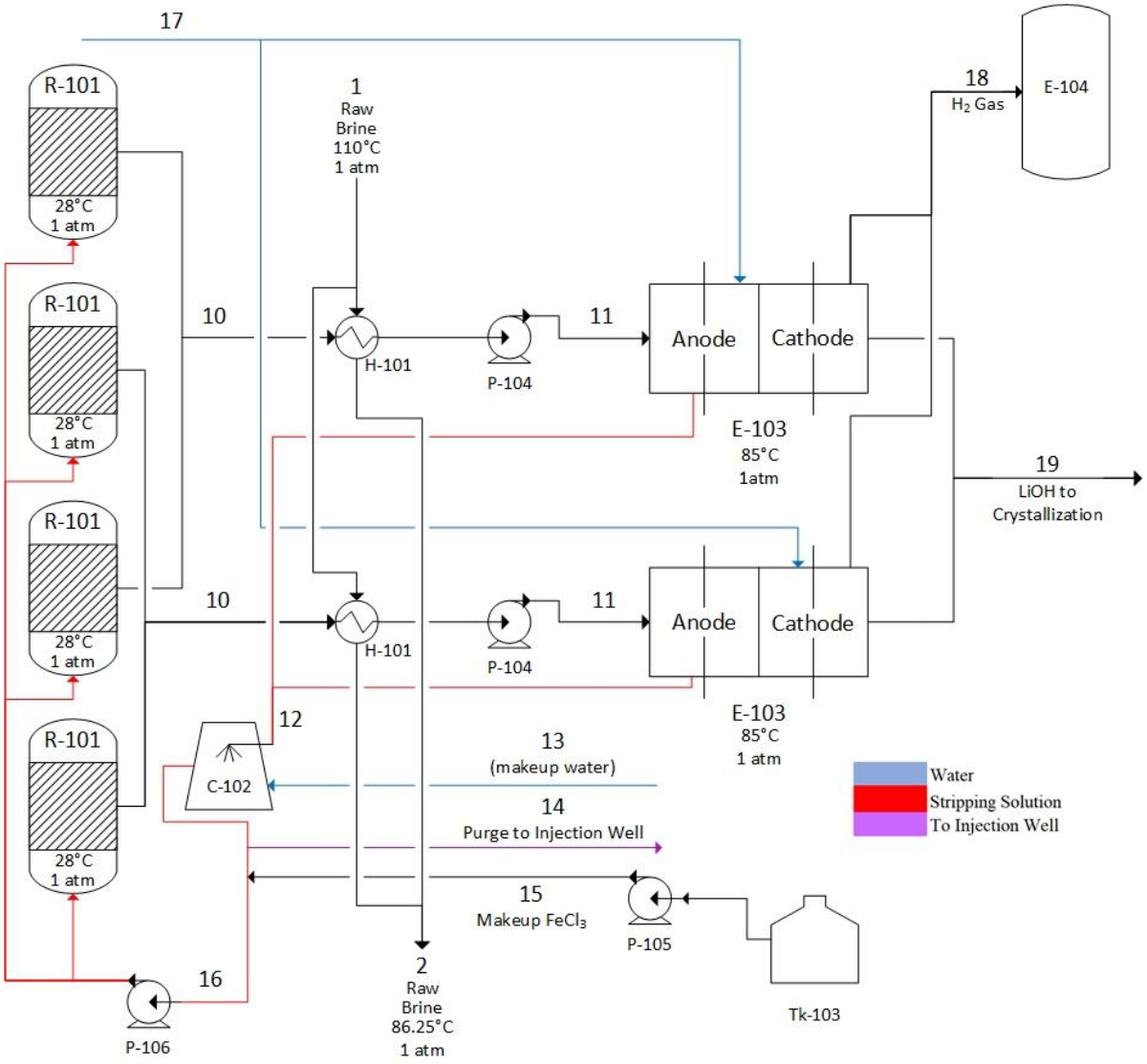

Figure 11. Close-up Process Flow Diagram of Electrolyzer Units E-103 and E-104

The streams between the packed bed reactor network and electrolyzer units are shown above in Figure 11.

Table 7. Flow Summary Table for Electrolysis

Stream		1	2	10	11	12	13	14	15	16	17	18	19
Temperature (°C)		110	86.25	28	85	85	28	28	28	28	25	85	85
Pressure (atm)		1	1	1	1	1	1	1	1	1	1	1	1
Mass Flow (kg/hr)		1,637,129.97	1,637,129.97	340,646.47	340,646.47	680,906.81	63,412.80	68,090.68	68,084.26	680,900.39	11,452.63	55.37	11,787.32
Component Flow (kg/hr)	H_2O	1,151,696.79	1,151,696.79	335,980.92	335,980.92	671,961.83	63,412.80	67,196.18	67,196.18	671,961.83	11,452.63	—	10,463.11
	LiOH	—	—	—	—	—	—	—	—	—	—	—	1,302.55
	LiCl	—	—	1,152.82	1,152.82	—	—	—	—	—	—	—	—
	Li	380.99	380.99	—	—	—	—	—	—	—	—	—	—
	$FeCl_2$	—	—	3,469.95	3,469.95	—	—	—	—	—	—	—	—
	$FeCl_3$	—	—	—	—	8,880.81	—	888.08	888.08	8,880.81	—	—	—
	H_2	—	—	—	—	—	—	—	—	—	—	55.37	—
	NaOH	—	—	—	—	—	—	—	—	—	—	—	21.66
	NaCl	—	—	42.78	42.78	64.17	—	6.42	—	57.75	—	—	—
	Na	97,970.44	97,970.44	—	—	—	—	—	—	—	—	—	—
	Ca	58,716.27	58,716.27	—	—	—	—	—	—	—	—	—	—
	Cl	291,932.06	291,932.06	—	—	—	—	—	—	—	—	—	—
	Fe	2,754.28	2,754.28	—	—	—	—	—	—	—	—	—	—
	K	29,523.13	29,523.13	—	—	—	—	—	—	—	—	—	—
	Mn	3,446.81	3,446.81	—	—	—	—	—	—	—	—	—	—
	B	709.20	709.20	—	—	—	—	—	—	—	—	—	—

Table 7 outlines the flow rates of the streams that surround the electrolysis process. Due to the set-up of the four reactor network, the use of two electrolyzer units instead of one enables continuous processing of outlet flows from the packed bed reactor units. Each feed is directed into the anode where the Fe^{2+} undergoes oxidation to form Fe^{3+}. A secondary reaction that competes within the incoming anolyte results in the oxidation of H_2O into H^+ protons. There are therefore two reactions involving H_2O that can occur in the electrolyzer unit: one involves the oxidation of H_2O that occurs on the anode side and another that involves the reduction of H_2O that occurs on the cathode side (Grageda et al., 2020). The standard potential for the oxidation of H_2O is 1.229 V whereas the standard potential for the reduction of H_2O is -0.827 V.

On the anode side, the oxidation of iron is favored over the oxidation of water because of the lower standard potential of 0.77 V vs 1.229 V, thus the oxidation of H_2O is considering a secondary reaction to the oxidation of iron. The Grageda paper mentions the oxidation of chlorine ions into chloride gas that has a standard reduction potential of 1.358 V. The applied total voltage for this cell design is below the minimum amount for the oxidation of chlorine and the reduction of H_2O to both occur. Thus, Cl_2 gas formation reaction was neglected from our analysis.

Due to the much higher tendency of the iron to oxidize, the formation of NaOH was chosen to reflect the current inefficiency. After the oxidation, the anolyte leaves the unit and is recycled to the packed bed reactor as an aqueous stream of $FeCl_3$ for reactor stripping. Any excess $FeCl_3$ simply enters and leaves the anode section of the electrolyzer unreacted.

A fresh $FeCl_3$ stream has a much greater cost than a recycled mixed composition stream. Thus, a recycle stream was selected that contains a significant amount of reused $FeCl_3$ from the electrolyzer unit. A smaller fresh makeup $FeCl_3$ stream is also included to maintain the necessary concentration of $FeCl_3$ flowing into the sorbent stripping stage. A purge stream is also included to

prevent the buildup of unreacted NaCl. This is important because the desired input for stripping is pure aqueous $FeCl_3$.

At the cathode side, a deionized water stream coming from the reverse osmosis (RO) unit is fed as the catholyte. RO purifies the water stream coming out of the washing step in the packed bed reactor system. The cathode reduction involves two molecules of H_2O gaining two electrons, resulting in splitting that forms hydroxide ions (OH^-) and hydrogen gas (H_2). The H_2 gas stream is directed to a fuel cell unit where 1.14 MW of total electricity is produced based on an assumed efficiency of 60% (Gahleitner, 2013). The use of deionized water ensures that no other side reactions occur on the cathode side, especially considering the low standard potential for reducing H_2O which is -0.827 V. On the anode side, the release of the electron from the oxidation of iron drives the lithium ion across the proton exchange membrane (PEM) where it combines with hydroxide on the cathode side to form lithium hydroxide (LiOH). The composition of LiOH in the total stream leaving the cathode and going to the crystallizer is 11 weight percent.

The overall reaction within the electrolyzer unit is outlined below, Equation 18:

$$2LiCl\,(aq) + 2FeCl_2\,(aq) + 2H_2O\,(aq) \rightarrow 2LiOH\,(aq) + 2FeCl_3\,(aq) + H_2\,(g) \quad (18)$$

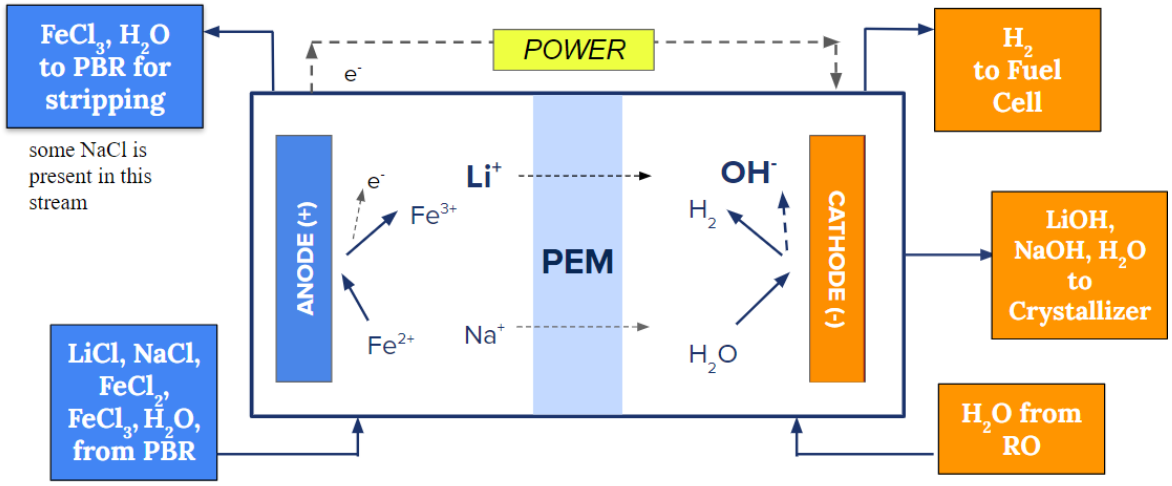

Figure 12. Electrolysis Cell Conceptual Overview

Other potential side products include NaOH. NaOH accounts for a very small amount of the final product leaving the cathode due to the high selectivity of Nafion 117 toward lithium, with 25% of incoming sodium ions passing through the membrane as opposed to 100% for lithium (Grageda et al., 2020).

The reactions at the anode and cathode with the corresponding standard reduction potentials are below:

Anode: $2Fe^{2+} = 2Fe^{3+} + 2e^{-}$ $\quad E0 = 0.77\,V$

Secondary Anode: $2H_2O = 4H^{+} + O_2 + 4e^{-}$ $\quad E0 = 1.229\,V$

Cathode: $2e^{-} + 2H_2O = 2OH^{-} + H_2$ $\quad E0 = -0.87\,V$

Overall: $2Fe^{2+} + 2H_2O = 2Fe^{3+} + 2OH^{-}$ $\quad E0 = -1.597\,V$

The overall standard reduction potential of the reaction is -1.597 V, as calculated in Appendix C.1, and it represents the theoretical cell voltage (V_{cell}) ignoring mass transport limitations and ohmic resistance drops. The standard reduction potentials were used to represent the reaction despite electrolyzer conditions set at 85°C. Grageda (2020) cites small differences between voltages when measured at different temperatures.

Table 8. Material Balance Around One Electrolyzer Unit

Stream		In Anode	In Cathode	Out Anode	Out Cathode	Out Cathode
Phase		Aqueous	Liquid	Aqueous	Aqueous	Vapor
Mass Flow (kg/hr)		340,646.47	5,726.32	340,453.41	5,893.66	27.68
Component Flow (kg/hr)	H_2O	335,980.92	5,726.32	335,980.92	5,231.56	—
	LiOH	—	—	—	651.27	—
	LiCl	1,152.82	—	—	—	—
	$FeCl_3$	—	—	4,440.40	—	—
	$FeCl_2$	3,469.95	—	—	—	—
	H_2	—	—	—	—	27.68
	NaOH	—	—	—	10.83	—
	NaCl	42.78	—	32.08	—	—

A more specific material balance around one electrolyzer unit is detailed in Table 8. These balances take into account the use of a recycle and purge stream to prevent buildup of sodium ions.

Thermodynamically, Equation 9 was used to determine the overall Gibbs Free Energy of the reaction. This was calculated as 308 kJ/mol, as shown in Appendix C.2. The highly

non-spontaneous nature of the reaction implies that an external power source is required to drive the reaction, necessitating the use of an electrolysis cell as opposed to an electrochemical cell.

4.4.2 Optimal Electrolyzer Unit Conditions

Grageda optimized process conditions for lithium hydroxide production from electrodialysis (2020).

Table 9. Experimental Conditions for LiOH Production from Electrodialysis (Grageda et al., 2020)

N° Experiment	1	2	3	4	5	6	7	8	9	10	11	12
Current density ($A \cdot m^{-2}$)	1200	2400	3600	2400	2400	2400	2400	2400	2400	2400	2400	1200
Cathode material	Nickel	Nickel	Nickel	Nickel	Stainless Steel 316	Nickel	Stainless Steel 316	Nickel	Nickel	Nickel	Nickel	Nickel
Initial Anolyte [1]	Anolyte 1	Anolyte 1	Anolyte 1	Anolyte 1	Anolyte 1	Anolyte 1	Anolyte 1	Anolyte 1	Anolyte 1	Anolyte 1	Anolyte 1	Anolyte 2
Initial concentration of LiOH in the catholyte (wt %)	2.30	2.30	2.30	2.30	2.30	2.30	2.30	5.70	2.30	2.30	1.15	1.15
Temperature (°C)	85	85	85	75	75	85	85	85	25	50	85	85
Membrane (NAFION)	117	117	117	117	117	115	115	117	117	117	117	117

Table 9 reflects the various experimental conditions that were tested by the experimental group, with experiment 2 representing the optimal condition for maximizing LiOH production. The use of Nafion 117 as a proton exchange membrane is beneficial due to its high proton conductivity, good chemical stability and mechanical properties that make it selective to atoms like lithium and hydronium (Fan et al., 2020). The greater thickness of the Nafion 117 over 115 serves to act as a greater barrier for hindering the transport of other contaminants like sodium (Na^+) and potassium ions (K^+) across the membrane.

Electrode materials consist of the cathode and anode where reduction and oxidation take place, respectively. Graphite was selected as the anode material due to its high energy and power density, long cycle life and relatively low cost (Zhang et al., 2021). Zhang discusses how the use of stainless steel 316 as the cathode material corresponds to a lower exchange current density and greater overpotential than nickel. This supported the decision that nickel is the better cathode for the electrolyzer.

We chose an operating temperature of 85°C because it corresponded to the greatest production rates of LiOH (Grageda et al., 2020). Greater operating temperatures are also correlated with greater migration speed and diffusion rates of ions through the membrane. We

ignored the high water vapor content of the H_2 stream at this temperature when determining the amount of electricity generated in the fuel cell. We also selected an operating pressure of 1 atm and a current density of 2,400 A/m^2 to maximize LiOH output and minimize energy consumption. The minimized energy consumption is based on an incremental increase in LiOH production from 2400 to 3600 A/m^2 that resulted in a very small increase in produced LiOH.

Using the second experimental conditions from Table 9, the expected current efficiency is 73.27%. Current efficiency indicates how much of the current in the electrolyzer goes toward producing LiOH on the cathode side. This is indicative of the relative rates of Li^+ opposed to H^+ or Na^+ transport across the membrane. Sodium ion (Na^+) transport, due to its relatively high concentration after recycling, was considered the main driver for limiting the generation of LiOH.

Table 10. Final Operating Conditions for one Electrolyzer Unit

Parameter	Value
Temperature	85 °C
Pressure	1 atm
Current Density	2400 A/m^2
Membrane	Nafion 117
Anode Material	Graphite
Anode Effective Area	820 m^2
Cathode Material	Nickel
Cathode Effective Area	410 m^2

Table 10 outlines the final operating conditions of one electrolyzer unit, with most conditions based on experimental data.

4.6.3 Overpotential Required for V_{cell}

Overpotential refers to the potential difference between a half-reaction's equilibrium potential for a specific reaction and the operating potential under specific conditions. This means that the applied voltage must be greater than the theoretical V_{cell} value to drive the redox reaction. The value of cathodic overpotential was selected using the overpotential used in the Grageda paper (2020).

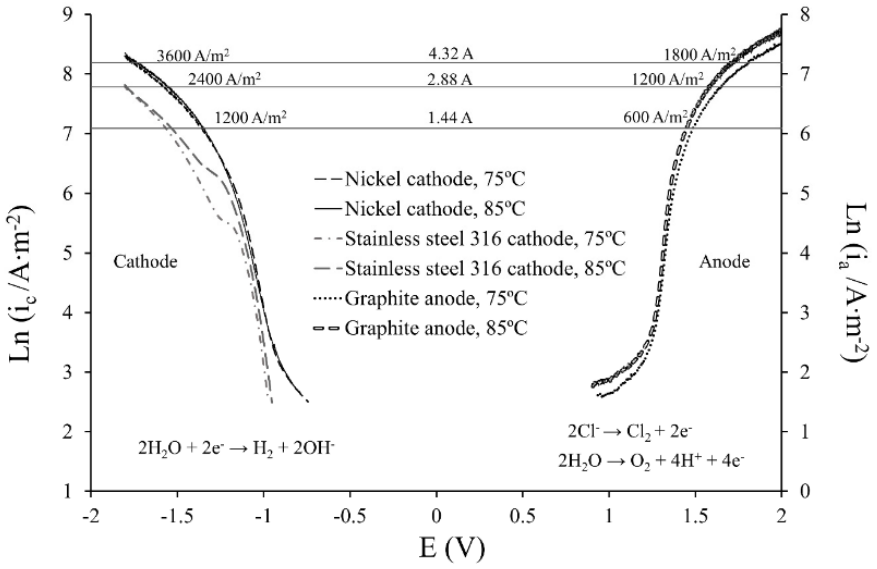

Figure 13. Kinetics of Oxidation (Cl^-/Cl_2 and H_2O/O_2) and Reduction Kinetics (H_2O/H_2) using Nickel, Stainless Steel 316 and Graphite at 75°C and 85°C (Grageda et al., 2020)

The graph of the potentiodynamic sweeps, Figure 13, was used to determine the amount of overpotential added to the electrolyzer on the cathode side. This is applicable to our process since the cathode reaction in our electrolyzer unit matches that in the paper. The total amount of voltage added to a system in order to overcome the anodic and cathodic overpotentials is determined using Equation 19. Thus, calculating the overall V_{total} involves finding both the anodic and cathodic overpotentials.

$$V_{total} = |\Delta E_e| + \eta_a + |\eta_c| \quad (19)$$

where ΔE_e represents the overall standard reduction potential of the reaction, η_a is the anodic overpotential, and η_c is the cathodic overpotential.

Using the potentiodynamic sweep curve with the desired current density of 2,400 A/m^2, the determined cathodic overpotential requirement was 0.573 V. The current cathodic potential is

-0.827 V and the operating voltage is approximately -1.4 V from the potentiodynamic sweep. Thus, an overpotential on the cathode side with an absolute value of 0.573 V is necessary for the redox reaction to occur.

Figure 13 shows data for the anode reaction for the oxidation of chlorine into chlorine gas. Since the anode reaction for our process involves the oxidation of Fe^{2+} to Fe^{3+}, a different procedure was implemented to determine the anodic overpotential. Based on the current efficiency numbers listed in the paper, the chosen assumption is built upon the notion that the remaining 27% of the current goes toward the production of NaOH from the incoming NaCl on the anode side. After accounting for the cathodic overpotential, the cell voltage stands at 2.173 V. Based on the Grageda paper, operating at a cell equilibrium voltage of greater than 2.2 V results in the formation of Cl_2 gas as the chlorine ions oxidize at the anode side. Thus, with the current anode voltage at 0.77 V, an anodic overpotential of 0.025 was selected to keep overall voltage to 2.2 V. When considering mass transport limitations as well, this means that a voltage of 0.15-0.2 V over the equilibrium voltage of 2.2 V will actually result in the undesired production of Cl_2 gas based on the potentiodynamic sweep graph. Therefore, the total necessary overpotential is about 0.598 V, resulting in a V_{total} of the cell of 2.2 V.

4.4.4 Determining Operating Current

In order to calculate the amount of current required to obtain the desired flow rate of produced LiOH, Equation 20 was used.

$$m_{theor} = \frac{I*t*M}{z*F} \quad (20)$$

where I is the current, t is time, M is molar mass of lithium, z is the number of electrons per lithium ion, and F is Faraday's constant.

The desired production of LiOH is 650 kg/hr per electrolyzer unit. Under the assumption that the theoretical mass transfer of lithium ions through the membrane is equal to the produced LiOH, the calculated current was 722,000 A, shown in Appendix C.3. However, this current assumes that 100% of the applied current goes into forming the lithium hydroxide on the cathode side. Thus, additional current must be applied given the 73% current efficiency of the system, resulting in 986,000 A of total current. Based on this calculated current, the total effective area needed for the cathode and anode are calculated from the current density of 2,400 A/m^2. Thus, the

required cathode effective area is 410 m^2 and the required anode effective area is 821 m^2. Double the anode area as opposed to the cathode is needed to reach the same current density; twice the area is required as shown from the potentiodynamic sweep figure.

With the total current and voltage, V, of the electrolyzer unit, the power is calculated through Equation 21:

$$P = I * V \quad (21)$$

The total calculated power is 2.17 MW per unit cell as shown in Appendix C.5. Thus, for two cells, the required power is 4.33 MW. This represents a little less than 10% of the total power at the 50 MW power plant in Salton Sea, California.

4.4.5 Heat Considerations from Electrolyzer Unit

Based on the limited use of the heat of formation in calculating the overall heat duty from the electrolyzer unit, the extra current and overpotential added over the equilibrium amount represents the heat generated from reaction. The calculated heat generated was calculated as 157 kW using Equation 22.

$$P = I_{\text{additional}} * (\eta_a + \eta_c) \quad (22)$$

where $I_{\text{additional}}$ is the extra current added.

This results in a change in temperature of the total brine solution of just 0.005°C as shown in Appendix C.7. This means that there is no need for designing a cooling jacket to maintain isothermal conditions in the electrolyzer.

4.4.6 Recycle Stream to Packed Bed Reactor Network

The stream leaving the anode side of the electrolyzer is recycled back to the packed bed reactor system network for stripping. While the initial amount of sodium in the inlet stream into and leaving the anode is not large, the gradual build-up of sodium necessitates the use of a purge stream. This is especially important considering that the modeling of the packed bed reactor stripping stage used a pure ferric chloride solution and increased sodium in this solution could limit stripping efficiency. In determining the purge stream percentage, we considered the

maximum allowable amount of sodium entering the electrolyzer to be 37:1 lithium to sodium molar ratio. The value of the maximum allowable amount of sodium into the electrolyzer unit was found based on the required inlet composition for the crystallizer unit that led to 99 wt% purity of $LiOH \cdot H_2O$. Based on the relatively large requirements for lithium as opposed to sodium, a larger purge stream of 10% was chosen.

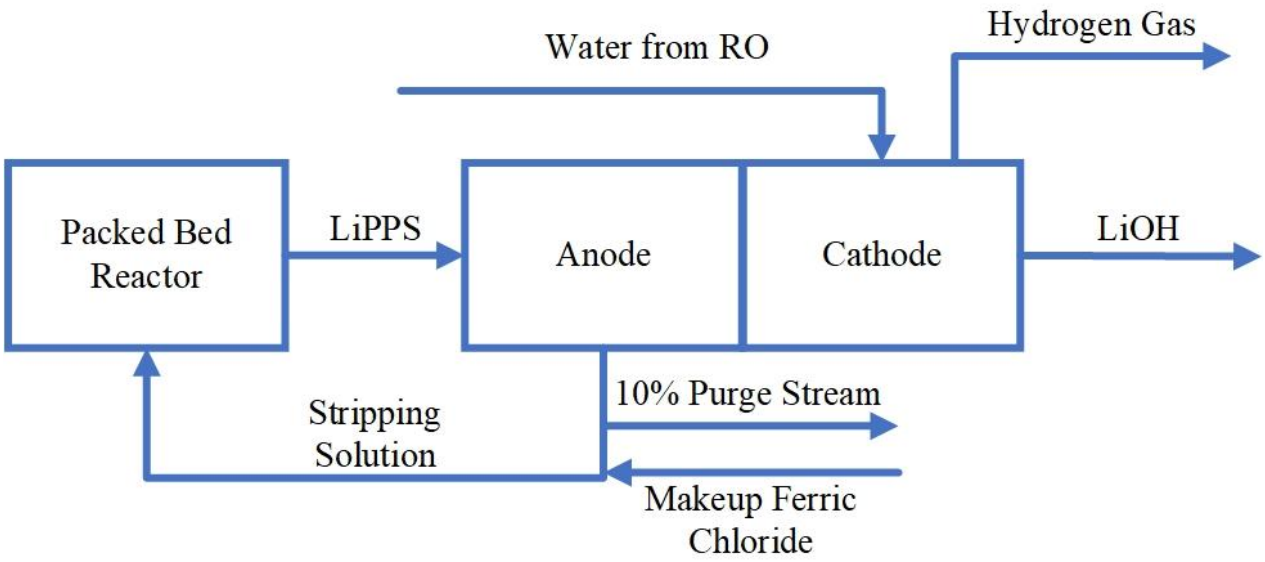

Figure 14. Simplified Block Flow Diagram Around Recycled Stripping Solution

Figure 14 shows a simplified version of the connected streams between the packed bed reactor system and the electrolyzer with the recycle and purge stream.

4.5 Crystallization

The following process utilizes evaporation crystallization as it is the conventional LiOH crystallization method since LiOH solubility does not depend strongly on temperature (Taboada et al., 2007). Crystallization was modeled as an ASPEN Electrolyte NRTL flash process. The inlet stream is modeled at 85°C and 1 atm and the crystallizer at 120°C and 1 atm. Running the block at 50°C/0.03 atm or 120°C/1 atm requires 4.26 MW or 5.59 MW, respectively. Capital costs for vacuum evaporators are high so we recommend high temperature and ambient pressure conditions despite the increased energy penalty. We recommend a forced circulation crystallizer (FCC) as they are suitable for shallow solubility curves, or curves in which the solubility does not increase greatly with increased temperature. The circulation pump rotation speed and crystallizer residence time offers particle size control.

Table 11. Material Balance Around Crystallizer E-105

Stream		**19**	**20**	**21**
IN/OUT		IN	OUT	OUT
Phase		Aqueous	Vapor	Solid
Mass Flow (kg/hr)		11,787.32	9,483.34	2,303.98
Component Flow (kg/hr)	**H_2O**	10,463.11	9,483.34	979.77
	LiOH	1,302.55	—	1,302.55
	NaOH	21.66	—	21.66

Table 11 outlines the material balance surrounding the crystallizer unit. Modeling the process with a flash unit does not allow selection for the $LiOH \cdot H_2O$ product, as Aspen predicts LiOH versus $LiOH \cdot H_2O$. Thus, we manually adjusted the water balance such that the $LiOH \cdot H_2O$ product is made. The crystallization unit yields 2,300 kg/hr $LiOH \cdot H_2O$ solid and 22 kg/hr NaOH solid. This is a 99% purity specification on a weight basis. The state of NaOH being in the anhydrous or hydrated form was considered irrelevant to the product outcome and the water balance was not adjusted for a hydrated NaOH form. The process vents 9,500 kg/hr of water

vapor after adjusting for the $LiOH \cdot H_2O$ product water balance. As the packing process for the lithium hydroxide monohydrate product is not currently watertight and lithium hydroxide is highly hygroscopic, no further drying steps are recommended.

4.5.1 Crystallizer Sizing

The following crystallization unit sizing procedure is based on Chapter 11 Crystallizer Design and Operation from Tavare (1995). Jancic and Grootscholten (1984) report a maximum dynamic pressure of released vapor, Equation 23:

$$\frac{1}{2}\rho_v u_v^2 \leq 1.75\ N/m^2 \quad (23)$$

where ρ_v is the vapor density, and u_v is the vapor superficial velocity. The corresponding minimum unit diameter is represented by Equation 24:

$$\sqrt{\frac{0.68 * V}{\rho_v^{0.5} * 3600}} \leq D_v \quad (24)$$

where V is the vent mass flow rate, ρ_v is the vent density, and D_v is the minimum unit diameter. The calculated minimum diameter is 1.70 meters, as shown in Appendix D.1. We select a double radial inlet and a single radial outlet bottom design. Newman and Bennett (1959) recommend a Reynolds number based on the inlet velocity and evaporator body diameter between 5,000,000 and 10,000,000.

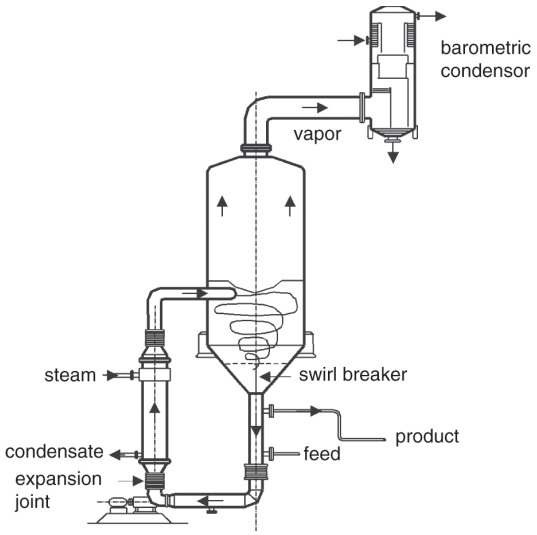

Figure 15. Forced Circulation Crystallizer Diagram (Kramer and Lakerveld, 2019)

Assuming an inlet Reynolds number of $5*10^6$ conservatively from the Newman and Bennett range, the inlet velocity can be estimated by Equation 25:

$$v_i = \frac{Re\mu_{sl}}{\rho_{sl} D_v} \quad (25)$$

where v_i is the inlet velocity, Re is the Reynolds number, μ_{sl} is the dynamic viscosity of the inlet solution, ρ_{sl} is the inlet solution density, and D_v is the unit diameter. The calculated inlet velocity is 2.20 $\frac{m}{s}$, as referenced in Appendix D.2. The diameter of the inlet radial ports D_i is estimated from Equation 26:

$$D_i = \sqrt{\frac{Q*4}{3600*2\pi v_i}} \quad (26)$$

where Q is the total circulating liquid flow rate and v_i is the inlet velocity. The calculated inlet radial port diameter is 0.037 meters, with calculations shown in Appendix D.3.

The total minimum unit height can be estimated by Equation 27:

$$H_{unit} = h + D_i + 0.75 D_v \quad (27)$$

where h is the hydrostatic head, D_i is the diameter of the inlet radial ports, and D_v is the unit diameter. We assumed the hydrostatic head requirement is negligible. The minimum unit height is thus 1.31 meters.

We recommend further process specific physicochemical data collection including the width of the metastability region for maximum allowable undercooling as a function of saturation, temperature, agitation, and crystal presence, and crystallization kinetics including crystal growth and nucleation rates.

4.6 Ancillary Equipment Design

4.6.1 Cooling Tower Design

4.6.1.1 Tower Design Parameters

The Salton Sea Known Geothermal Resource Area (KGRA) experiences seasonally fluctuating weather conditions such as periods of strong, gusty winds, annual dew point extremes from 47.3°C to -0.7°C, and higher humidity levels from December to March (Freedman et al., 2020; Owens et al., 2005; Owens et al., 2009; CDFW et al., 2017). Thus, mechanical draft cooling towers offer greater stability against environmental variation than atmospheric draft cooling towers. An induced draft type is more effective than a forced draft type against mechanical icing and has been adopted for liquid volumetric flow rates ranging from 750 to 700,000 gallons per minute. This volumetric range capability accounts for the 6,000 gallons per minute process basis and any local fluctuations. Mechanical induced cooling types have been used historically in Salton Sea geothermal operations (DiPippo, 1978; BNI & BHC, 1978).

A mean coincident wet bulb temperature of 23°C was selected using the Imperial County cooling design weather conditions with an 0.4% annual cumulative frequency (Owens et al., 2005). The minimum cooling tower temperature separation is 5°C from literature; therefore, the minimum brine exit temperature is 28°C (Green & Perry, 2008). The inlet brine temperature is 86.25°C, as the brine from the geothermal plant flash process at 110°C is first used in a downstream heat integration scheme, as outlined in Section 4.6.2, before being recycled to the beginning of the process. Heat integration doubly serves to lower the brine temperature and provide energy otherwise expended to the environment for useful process heating.

The total cooling range is 58.25°C based on the inlet brine temperature, 86.25°C, and the outlet temperature of 28°C. This would yield unreasonably high gas flow rate and tower diameter requirements. The total range is split into two towers within C-101 of varying cooling ranges such that the inlet gas flow rate and consequential sizing requirements are approximately equal between towers. The following design considers two towers run in series. Further economic analysis could optimize the number and configuration of cooling towers, as splitting the inlet brine and running towers in parallel could be more energetically or economically favorable.

The Imperial Valley has among the highest particulate matter air pollution concentrations in the United States particularly during strong west-southwesterly (WSW) springtime wind events (Freedman et al., 2020). Regular maintenance against particulate deposition will be critical for optimal thermal performance on top of expected anti-scaling measures owing to mineral deposition on tower packing.

4.6.1.2 C-101-A and C-101-B Design

Table 12. Inlet and Outlet Stream Temperatures Around C-101-A

	Brine	**Air**
Inlet	86.25°C	23°C
Outlet	55°C	37.8°C

Cooling towers are typically designed for an L/G ranging from 0.75 to 1.50. We modeled the cooling tower as a heat exchanger using Aspen v.11 with NRTL-RK method and heat exchanger design shortcut method. The brine was approximated as the water, sodium, and chloride ions from Appendix Table A.6 owing to limitations of electrolyte modeling in Aspen. Sodium and chloride are the dominant ions present in solution; therefore, we proceeded with an approximate brine composition.

The inlet brine is set at 86.25°C and 1 atm in the first cooling tower in C-101. The inlet air humidity ratio to the first cooling tower is 0.09054 $\frac{kg\ water}{kg\ dry\ air}$ based on a cooling design dry bulb temperature of 44°C (Owens et al., 2005), the 23°C mean coincident wet bulb temperature, and a psychrometric chart at 1 atm. Psychrometrics concerns itself with the thermodynamic and physical properties of gas and water vapor mixture. The inlet air is thus set at 23°C and 0.0089 mass fraction water. A lower inlet air temperature may be possible because the modeled mean monthly coincident wet bulb temperature represents a maximum for the region. However, we predict the effect of high brine salinity will dominate the effect of moderately variable inlet air temperature on tower performance. The following design is thus considered non-optimized. The simulated inlet brine vapor fraction is set to zero. The L/G ratio was selected as 0.75 for the greatest possible gas flow rate within reasonable operating range, yielding an inlet air flow rate of 34205.22 kg/min, as shown in Appendix E.1. The outlet brine temperature is 55°C and the outlet

air temperature is 37.8°C. From Aspen simulation, the enthalpic difference between the air inlet and outlet is 74.5 kJ/kg and the modeled brine heat capacity is 3.29 $\frac{kJ}{kg\,K}$. We recommend explicitly measuring the brine heat capacity with citrate additives.

From the Merkel equation, Equation 28, we find the tower characteristic ($\frac{K_a\bar{V}}{\bar{L}}$):

$$\frac{Ka\bar{V}}{L} = \int_{TC}^{TH} \frac{C_L dT}{h_w - h_a} \quad (28)$$

where K is the mass transfer coefficient, a is the contact area, $\bar{V}$ is the active cooling volume, L is the liquid mass flow rate, C_L is the liquid heat capacity, T_C is the liquid outlet temperature, T_H is the liquid inlet temperature, h_w is the enthalpy of saturated air at the bulk water temperature, and h_a is the enthalpy of the air-water vapor mixture at bulk water temperature. The Merkel equation theorizes the enthalpy difference between a given water droplet and a thin film of air surrounding it drives cooling (Green & Perry, 2008). The enthalpy of the air-water vapor mixture at bulk water temperature (h_a) and enthalpy of saturated air at the bulk water temperature (h_w) are approximated as the inlet and outlet air enthalpy values. The tower characteristic ($\frac{Ka\bar{V}}{L}$) is approximately 0.95, within Perry's recommended 0.5 to 2.5.

Fisenko et al. (2004) developed a mathematical model for mechanical induced draft counter flow cooling tower performance accounting for water droplet radii, temperature distribution, the change in temperature, and density of water vapor in the cooling air. Simulations predict the contributions of various physical and environmental variables on heat transfer, mass transfer, and overall tower efficiency.

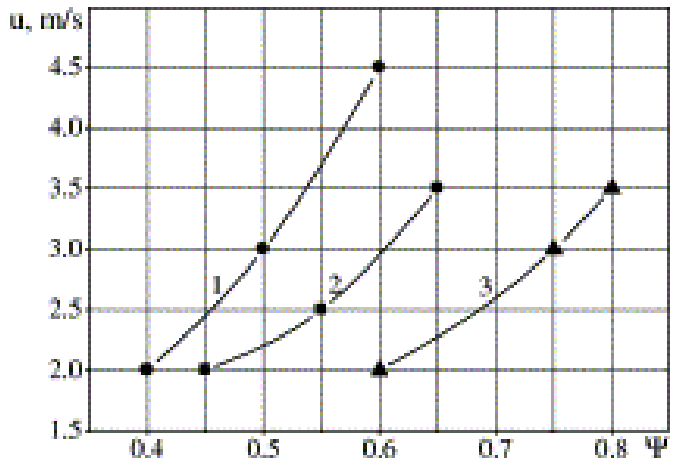

Figure 16. Cooling Tower Optimal Air Velocity vs. Relative Humidity: Curve 1 is for Air Temperature 25°C, Curve 2 is for Air Temperature 22°C and curve 3 is for Air Temperature 20°C (Fisenko et al., 2004)

Figure 16, from Fisenko et al., shows optimal superficial air velocity versus relative humidity for air streams at 25°C, 22°C, and 20°C for curves 1, 2, and 3, respectively. Higher humidity levels require higher optimal air velocity.

Based on the design dry and mean coincident wet bulb temperatures and psychrometry, the inlet air relative humidity is approximately 0.15. For estimation of the required tower cross sectional area, we will use an optimal value of 2 m/s inlet air flow as is the available humidity point. From the psychometrically derived inlet air density of 1.107 kg/m^3 , the inlet gas flow rate of 34,205 kg/min, and the approximated optimal superficial velocity of 2 m/s, the cooling tower cross sectional area should be 257 m^2, as referenced in Appendix E.3. This corresponds to a tower diameter of 18.1 meters.

Gharagheizi et al. (2007) derived a correlation between water and air mass flux and the mass transfer coefficient for a pilot scale mechanical induced draft counterflow cooling tower with vertical corrugated packing, Equation 29:

$$Ka = 0.534375L'^{0.747}\ G'^{0.253} \quad (29)$$

where K is the mass transfer coefficient based on the humidity driving force, a is the effective area of heat and mass transfer, L' is the water mass flux, and G' is the air flux. Their work was done for a range of 0.2 to 4 L/G ratio which includes the selected 0.75 L/G ratio. The inlet temperature difference between literature and process is approximately 77°C. While we assume this

correlation holds for different inlet brine temperatures, tower geometries, brine composition, and packing types, the following design can be considered highly non-optimized. By this correlation, Ka is equal to 0.95 ($\frac{kg}{m^2 s}$), as outlined in Appendix E.4. From Equation 30, derived in Geankoplis (2003) the estimated C-101-A tower height is 3.2 meters, as shown in Appendix E.5.

$$Z = \frac{G'}{Ka} \int_{Hy1}^{Hy2} \frac{dHy}{Hy^* - Hy} \quad (30)$$

Table 13. Inlet and Outlet Stream Temperatures Around C-101-B

	Brine	**Air**
Inlet	55°C	23°C
Outlet	28°C	35.9°C

We repeated the above design procedure for C-101-B. For an L/G ratio of 0.75, the minimum exit brine temperature is 28°C. The tower characteristic is thus 1.40. The mass transfer coefficient Ka, Equation 29, and cross sectional area are equivalent to the first tower at 0.95 ($\frac{kg}{m^2 s}$) and 257 m^2, respectively. The estimated C-101-B tower height is 3.26 meters.

Table 14. Tower Sizing for C-101-A and C-101-B

	C-101-A	**C-101-B**
Tower diameter (m)	18.11	18.11
Tower height (m)	3.20	3.26
Heat released (MW)	42	36

4.6.1.4 C-101-A and C-101-B Water Balance Considerations

Water makeup requirements include water losses due to evaporation, drift, and blowdown, Equation 31 (Green & Perry, 2008).

$$W_m = W_e + W_d + W_b \quad (31)$$

Evaporative losses W_e from C-101-A and C-101-B can be estimated together by Equation 32 from Green & Perry (2008) and equals 534 $\frac{gal\ water}{min}$, Appendix E.6.

$$W_e = 0.00085 W_c (T_1 - T_2) \quad (32)$$

where W_e is evaporative losses, T_1 is the liquid inlet temperature, T_2 is the liquid outlet temperature, and W_c is the inlet water flow rate. Drift loss, or water lost to entrainment in the ascending vapors can be estimated by Equation 33 (Green & Perry, 2008) and equals 1.2 $\frac{gal\ water}{min}$ for C-101-A and C-101-B, Appendix E.7.

$$W_d = 0.0002 W_c \quad (33)$$

where W_d is drift loss, and W_c is the inlet water flow rate.

Eliminator addition, particularly a metal panel aluminum filter eliminator, reduces drift losses (Shublaq & Sleiti, 2020). Further economic analysis between eliminator capital, installation, and operational costs versus operational costs without an eliminator can be considered in future design iterations.

Blowdown losses are water losses from discarding concentrated circulating water to lower the system solids concentration and prevent solid precipitation. No scaling or blowdown are considered because complex ion formation was not modeled in the saline brine. Operationally, discarding concentrated brine is detrimental to lithium ion recovery; therefore, blowdown will not be included in this process. Economic analysis between the potential product loss from solid precipitation versus discarding desired minerals from blowdown can be considered in further design iterations. Adding a condenser which supplies cooling tower makeup could also reduce blowdown losses. Together, evaporative and drift losses account for approximately 536 $\frac{gal}{min}$. We will add this amount of makeup water because the effect of reduced water concentration during adsorption is not known.

4.6.1.5 C-102 Design for Recycle Stream to the Packed Bed Reactor

Table 15. Inlet and Outlet Stream Temperatures Around C-102

	Ferric Chloride Solution	Air
Inlet	85°C	23°C
Outlet	28°C	73.32°C

The ferric chloride solution leaving electrolysis, Section 4.4.6, is cooled from 85°C, the operating temperature of the electrolyzer cells, to 28°C, the operating temperature of the PBR before recycling. The following section largely follows the procedure established in Section 4.6.1.2. The cooling tower was modeled in Aspen v.11 using NRTL-RK and heat exchanger shortcut design mode. For an inlet cooling air of 23°C and humidity ratio of 0.09054 $\frac{kg\ water}{kg\ dry\ air}$, the minimum gas flow rate to achieve an outlet solution temperature of 28°C is approximately 744,170 kg/hr. This results in an L/G mass ratio of 0.88, within the standard 0.75 to 1.5 range. By the design method established in 4.6.1.2, the cooling tower cross sectional area is 85 m^2 (10.4 m diameter) and the tower height is 32 meters.

4.6.1.6 C-102 Water Balance Considerations

From equations 31, 32, and 33, the drift losses, evaporative losses, and total makeup water requirement to C-102 are 0.6 gal/min, 279 gal/min, and 280 gal/min, respectively.

4.6.2 Heat Exchanger Design

The LiPSS exiting the reactor network goes through heat exchanger H-101 before entering the electrolyzer units. Two of these heat exchangers lie in parallel and each consist of two heat exchangers in series due to heat transfer area limitations. Since the reactor network operates at a temperature of 28°C and the electrolyzers operate at a temperature of 85°C, this heat exchanger raises the temperature of the LiPSS from 28°C to 85°C. To achieve this, the raw brine is passed through as the hot stream before it enters the mixing unit at the beginning of the process. Since we do not have experimental data on the brine's heat capacity, the brine is assumed to have the same heat capacity as water. The LiPSS is very dilute and has a molar mass of 18.2 g/mol, very similar

to the molar mass of water. Therefore, we assume the LiPSS to also have the same heat capacity as water. To obtain a greater correction factor, a two-pass shell and tube heat exchanger is selected for this design. We selected a two-pass shell and tube heat exchanger which provides a viable correction factor, ($F_T(R,S)$), of approximately 0.96.

The brine is cooled from 110°C to 86.25°C and passes through at a flow rate of 817,200 kg/hr. This is equivalent to half the flowrate listed in stream 1 or stream 2 as the stream is split between the two heat exchangers and combined before the brine enters the mixing unit. The LiPSS passes through heat exchanger H-101 at a flow rate of 340,600 kg/hr, as shown in Appendices E.8-E.12. The required heat duty for H-101 is 22,700 kW. Heat exchanger H-101 operates with 318 ten-meter long tubes where the LiPSS passes through the shell side and the hot brine passes through the tubes. This generates a total heat transfer surface area of 1,998 m^2, as calculated in Appendix E.9. This will be split between two heat exchangers with a heat transfer surface area of 999 m^2 each to generate a total area of 1,998 m^2 in H-101. While the total tube length is 10 meters in H-101, each heat exchanger in series will have 5 m long tubes. The tubes have an outer radius of 0.1 m and an inner radius of 0.06 m. The overall heat transfer coefficient was calculated to be 298 W/m^2K, as referenced in Appendix E.8. To resist corrosion due to ferric chloride contained within the LiPSS, the heat exchanger is made out of titanium material on both the shell and tube side.

4.6.3 Pump Design

The pumps in this process are designed as centrifugal pumps which are typically used for flows up to 1,000 L/s and for up to 150 m of head. The power requirement calculations are performed using Equation 34, assuming a pump efficiency of 70% and an electrical driver efficiency of 90% for all pumps.

$$Power = \frac{\Delta P * Q}{\eta_P} * 100 \quad (34)$$

where ΔP is the change in pressure, Q is the volumetric flow rate, and η_P is the pump efficiency.

Table 16. Pump Discharge Pressure and Power requirements

Pump ID	Discharge Pressure (barg)	Power (kW)
P-101	11.01	641.43
P-102	11.01	641.28
P-103	51.01	98.02
P-104	1.52	23.57
P-105	1.01	3.01
P-106	8.01	241.30
P-107	1.01	0.54

Table 16 details the gauge discharge pressure and the power requirements for each pump in this process. All process units operate at atmospheric pressure. Pump P-101 pumps the brine following the additives mixing unit into the reactors for sorbent loading. There is a 10 bar pressure drop during sorbent loading, as detailed in section 4.3. Additionally, there is an assumed 0.505 bar pressure loss due to flow through pipes and an assumed 0.505 bar pressure loss due to the control valves around the reactor network. This results in a discharge pressure of 11.01 barg. The brine passes through pump P-101 at a flow rate of 454 kg/s or 0.367 m^3/s which results in a power requirement of 641.43 kW.

Pump P-102 pumps the lithium-depleted brine back to the injection well. Pump P-102 maintains the same discharge pressure as pump P-101 to account for pressure difference in the reactors, flow through pipes, and flow through control valves. Due to the similar volumetric flows in both streams, P-102 has a similar power requirement of 641.28 kW.

Pump P-103 is responsible for pumping the washing water into the reactors from reverse osmosis unit E-102. Industrial seawater reverse osmosis units typically have an osmotic pressure of 50 bar. Additionally, there is an assumed 0.505 bar pressure loss due to flow through pipes and an assumed 0.505 bar pressure loss due to control valves. This results in a discharge pressure of 51.01 barg. The washing water passes through pump P-103 at a flow rate of 12.07 kg/s or 0.012 m^3/s which results in a power requirement of 98.0 kW.

Pump P-104 pumps the LiPSS following the heat exchangers into the electrolyzer units. Although there is no pressure difference between the reactor and the electrolyzer, there is an assumed 0.505 bar pressure loss due to flow through pipes, an assumed 0.505 bar pressure loss due to the control valves, and an assumed 0.505 bar pressure loss due to flow through a heat

exchanger. This results in a discharge pressure of 1.52 barg. The LiPSS passes through pump P-104 at a flow rate of 95 kg/s or 0.098 m^3/s which results in a power requirement of 23.6 kW.

Pump P-105 pumps makeup $FeCl_3$ from storage vessel Tk-103 into the recycled stripping solution. Storage vessel Tk-103 operates at atmospheric pressure so there is no pressure difference besides an assumed 0.505 bar pressure loss due to flow through pipes and an assumed 0.505 bar pressure loss due to control valves. This results in a discharge pressure of 1.01 barg. The makeup $FeCl_3$ passes through pump P-105 at a flow rate of 18.9 kg/s or 0.019 m^3/s which results in a power requirement of 3.01 kW.

Following electrolysis, Pump P-106 directs the stripping solution in the recycle loop back to the reactors to perform sorbent stripping. There is a seven bar pressure drop during sorbent stripping, as detailed in section 4.3. Additionally, there is an assumed 0.505 bar pressure loss due to flow through pipes and an assumed 0.505 bar pressure loss due to control valves. This results in a discharge pressure of 8.01 barg. The brine passes through pump P-106 at a flow rate of 189 kg/s or 0.190 m^3/s which results in a power requirement of 241.30 kW.

Pump P-107 pumps the LiOH-rich outlet stream from the electrolyzer units towards the evaporation and crystallization unit. There is no pressure difference between the electrolyzer unit and the evaporation and crystallization unit, but there is an assumed 0.505 bar pressure loss due to flow through pipes and an assumed 0.505 bar pressure loss due to control valves. This results in a discharge pressure of 1.01 barg. The LiOH-rich solution passes through pump P-107 at a flow rate of 3.27 kg/s or 0.003 m^3/s which results in a power requirement of 0.54 kW.

SECTION 5: DESIGN

5.1 Mixing Unit

Mixing is the first stage in the process for producing battery-grade lithium hydroxide monohydrate. This section involves adding tripotassium citrate monohydrate and ferrous chloride to the silica-free brine feed in a mixing tank. The addition of ferrous chloride in a 1:1 molar ratio to lithium and tripotassium citrate monohydrate in a 1:1 molar ratio to the iron drives the electron transfer in adsorption to completion.

Table 17. Material Balance Around Mixing Unit E-101 (kg/hr)

Stream		2	3	4	6
IN/OUT		IN	IN	OUT	OUT
Phase		Aqueous	Solid	Solid	Aqueous
Mass Flow (kg/hr)		1,637,129.97	16,573.05	14,587.06	1,639,115.92
Component Flow (kg/hr)	H_2O	1,151,696.79	—	802.75	1,151,775.51
	Li	380.99	—	—	380.99
	$FeCl_2$	—	699.67	—	—
	Na	97,970.44	—	—	97,970.44
	Ca	58,716.27	—	5,358.03	53,358.25
	Cl	291,932.06	—	—	292,323.81
	Fe	2,754.28	—	—	3,062.54
	K	29,523.13	—	—	35,262.76
	Mn	3,446.81	—	—	3,446.81
	B	709.20	—	—	709.20
	$C_6H_5O_7$	—	—	8,426.28	825.61
	$K_3C_6H_5O_7 \cdot H_2O$	—	15,873.38	—	—

Table 18. Equipment Summary for Mixing

Equipment ID	Name	Material of Construction	Design Specifications
C-101	Cooling Tower for inlet brine	PVC	2 x 427 L/s
Cv-101	Screw Conveyor for Citrate	Stainless Steel 304	2.4 kW, 10 m
Cv-102	Screw Conveyor for $FeCl_2$	Titanium	0.44 kW, 10 m
E-101	Mixing Vessel	Titanium	2x2 m, vertical
	Propeller	Stainless Steel 304	273 kW
P-101	Brine to PBR	Titanium	641 kW, 11 barg
Tk-101	Citrate Storage	Carbon Steel	2700 m^3
Tk-102	$FeCl_2$ Storage	HDPE	250 m^3

The stream flows and equipment summary of this unit are shown in Tables 17 and Table 18. A carbon steel tank Tk-101, with a total volume of 2700 m^3, stores the tripotassium citrate monohydrate powder. Another tank made out of HDPE, Tk-102, has a total volume of 250 m^3 and stores the ferrous chloride powder. In order to transport the citrate from the storage tank to the mixing tank, a screw conveyor, Cv-101, made out of Stainless Steel 304 is used. This screw conveyor has a power requirement of 2.4 kW and a conveyor length of 10 m. An additional titanium screw conveyor, Cv-102, is used to transport the ferrous chloride powder to the mixing unit with a power of 0.44 kW and conveyor length of 10 m. The inlet brine, fed at 86.25℃ and 1 atm, at a flow rate of 1,637,000 kg/hr goes into mixing unit E-101 which has a diameter of 2 m and a height of 2 m. The mixing unit has a mean residence time of 17 seconds, and operates at 1 atm and 86℃.

The brine and citrate mixture, with a total flow rate of 1,639,000 kg/hr, flows into a series of two cooling towers to decrease the temperature from 86℃ to 28℃. The first cooling tower, C-101-A, decreases the brine temperature from 86℃ to 55℃, which corresponds to 44 MW of heat released, with a makeup water stream of 121,000 kg/hr to restore water lost primarily from evaporative losses. For C-101-A, the diameter is 18 m and the height is 3.2 m. The second tower, C-101-B, decreases the brine temperature from 55℃ to 28℃, which corresponds to 36 MW of heat released. For C-101-B, the diameter is 18 m and the height is 3.3 m. Both cooling towers are made from PVC.

Following cooling, the brine and citrate mixture at 28℃ is pumped using a titanium centrifugal pump, P-101, to the packed bed reactor network. With a flow rate of 1,639,000 kg/hr, the discharge pressure is 11 barg and the power requirement is 641.4 kW.

5.2 Packed Bed Reactor Network

The packed bed reactor network is the second stage of the design. Here, the brine that contains a low concentration of lithium ions is converted into a higher concentration lithium chloride solution. This is achieved using a Iron (III) Phosphate sorbent material that selectively absorbs lithium ions from the brine. This stage occurs in four distinct phases: sorbent loading, washing, sorbent stripping and washing again.

Table 19. Material Balance Around Packed Bed Reactor R-101 (kg/hr)

Stream		6	7	8	8	10	16
IN/OUT		IN	OUT	IN	OUT	OUT	IN
Phase		Aqueous	Aqueous	Aqueous	Aqueous	Aqueous	Aqueous
Mass Flow (kg/hr)		1,639,115.92	1,638,726.05	43,446.78	43,446.78	340,646.47	680,900.39
Component Flow (kg/hr)	H_2O	1,151,775.51	1,151,775.51	43,446.78	43,446.78	335,980.92	671,961.83
	LiCl	—	—	—	—	1,152.82	—
	Li	380.99	3.50	—	—	—	—
	$FeCl_2$	—	—	—	—	3,469.95	—
	$FeCl_3$	—	—	—	—	—	8,880.81
	NaCl	—	—	—	—	42.78	57.75
	Na	97,970.44	97,958.06	—	—	—	—
	Ca	53,358.25	53,358.25	—	—	—	—
	Cl	292,323.81	292,323.81	—	—	—	—
	Fe	3,062.54	3,062.54	—	—	—	—
	K	35,262.76	35,262.76	—	—	—	—
	Mn	3,446.81	3,446.81	—	—	—	—
	B	709.20	709.20	—	—	—	—
	$C_6H_5O_7$	825.61	825.61	—	—	—	—

Table 20. Equipment Summary for Packed Bed Reactor Network

Equipment ID	Name	Material of Construction	Design Specifications
C-102	Cooling Tower for Recycle Stream	PVC	189 L/s
E-102	Reverse Osmosis	Stainless Steel 304	1000 m^3/day
P-102	Spent Brine to Well	Titanium	641 kW, 11 barg
P-103	Wash Water to PBR	Stainless Steel 304	98 kW, 51 barg
P-105	$FeCl_3$ from Storage to PBR	Titanium	3.01 kW, 1.01 barg
R-101	PBR	Titanium	4, 3.6 x 1.79 m, vertical vessels

The stream flow table for this section is shown in Table 19. Design parameters for the equipment in this stage are summarized in Table 20. The brine enters the reactor at a flow rate of 1,639,000 kg/hr with a lithium concentration of 231 mg/kg. The reactor superficial velocity is set at 0.15 m/s, so the diameter must be 1.79m with the specified volumetric flow. The maximum pressure drop across the reactor is set at 10 bar, thus the length is 3.6 m. The volume of the bed is 9.06 m^3. The sorbent is assumed to be 100:1 selective to lithium over sodium on a molar basis; for every 101 sites, 100 are lithium and 1 is sodium. Loading occurs over one hour and 377 kg of lithium and 12 kg of sodium are entrained in the bed in this time, assuming a 1% loss to reinjection. Assuming the maximum heat is released for a chemisorption reaction, the fluid through the bed raises 5.7 °C. This has a negligible effect on the adsorption reaction behavior. The adsorbed lithium and sodium represent just under 55% of sites filled in the sorbent material. The remainder of the brine is sent back to be reinjected into the ground without any post processing steps necessary.

There are two washing cycles: one after sorbent loading and the other after sorbent stripping. The purpose is to remove excess ions not chemically bound to the sorbent material. This ensures a fresh bed with no side reactions for both sorbent loading and stripping. In our design, we assume no ions remain in interstitial sites; however, we include a washing step to account for this possibility in real-world applications. Five bed volumes of water were selected based on the most conservative washing estimate from chromatography experiments, which is equivalent to a flow rate of roughly 43,400 kg/hr. This water is first purified in the reverse osmosis unit, E-102, where any aqueous ions are removed. The reverse osmosis unit processes 1000 m^3 of water a day and is made of stainless steel 304. The cooling tower has a diameter of 10.4 meters and a height of 32 meters. The water is pumped into the beds using pump P-103 which is made of stainless steel 304 and uses 98 kW of electricity with a pressure differential of 51 barg.

The final step to convert the adsorbed lithium to the lithium chloride solution is sorbent stripping. An aqueous ferric chloride solution is pumped through the bed at a rate of 680,900 kg/hr. This stream is cooled from 85°C to 28°C to maintain constant temperature in the reactors using cooling tower C-102. This process emits 45 MW of heat. The aqueous solution contains ferric chloride in just under a 2:1 excess to ensure all lithium and sodium are released from the bed. The ferric chloride solution is a product from the anode side of the electrolyzer cell with ferric chloride makeup from storage to reach the desired concentration of stripping solution.

Sorbent stripping occurs over a two hour period as the superficial velocity is roughly half that of sorbent loading. The same maximum heat released from chemisorption is assumed, but the lower mass flow causes a higher temperature change of the solution with a value of 9 °C. This has a negligible effect on the behavior of the desorption reaction. The stream leaving sorbent stripping is 340,650 kg/hr, contains all entrained lithium and sodium, and is assumed to have a constant concentration of these ions for the next stage.

5.3 Electrolysis

Following the packed bed reactor network, the electrolyzer cell represents the third process stage of design. In this section, the lithium pregnant stripping solution (LiPSS) from two packed bed reactors is sent to two electrolyzer units in parallel in order to convert the incoming lithium chloride to lithium hydroxide. Other byproducts include H_2 gas that is sent to a hydrogen fuel cell as well as $FeCl_3$ solution that is recycled back to the packed bed reactor network for stripping.

Table 21. Material Balance Around Electrolyzer E-103 (kg/hr)

Stream		In Anode	In Cathode	Out Anode	Out Cathode	Out Cathode
Phase		Aqueous	Liquid	Aqueous	Aqueous	Vapor
Mass Flow (kg/hr)		340,646.47	5,726.32	340,453.41	5,893.66	27.68
Component Flow (kg/hr)	H_2O	335,980.92	5,726.32	335,980.92	5,231.56	—
	LiOH	—	—	—	651.27	—
	LiCl	1,152.82	—	—	—	—
	$FeCl_3$	—	—	4,440.40	—	—
	$FeCl_2$	3,469.95	—	—	—	—
	H_2	—	—	—	—	27.68
	NaOH	—	—	—	10.83	—
	NaCl	42.78	—	32.08	—	—

Table 22. Equipment Summary for Electrolysis

Equipment ID	Name	Material of Construction	Design Specifications
E-103	Electrolyzers	Titanium	2 x 2.2 MW
E-104	Hydrogen Fuel Cell	Carbon Steel	1.14 MW
H-101	PSS Cooler	Titanium/ Titanium	4x1000 m^2, 2 in series, 2 in parallel
P-104	PSS to Electrolyzer	Titanium	23.6 kW, 1.52 barg, 2 in parallel
P-105	Recycle from Electrolyzer to PBR	Titanium	241 kW, 8.01 barg
Tk-103	$FeCl_3$ Solution Storage	HDPE	7800 m^3

The stream flows and unit operations for this process is outlined in Tables 21 and 22. In order to increase the temperature of the stream leaving the reactor from 28℃ to 85℃ degrees C, four heat exchangers H-101 are used: two in parallel and two in series. These heat exchangers consist of countercurrent shell-and-tube heat exchangers with heat transfer areas of 999 m^2 each, where both the tube and shell are made of titanium. More specifically, there are 318 ten-meter tubes total where each tube has an outer radius of 0.1 m and an inner radius of 0.06 m. The total power requirement is 22,650 kW. The feed brine, with a flow rate of 1,637,000 kg/hr, is used in the beginning of the process to heat up the stream entering the electrolyzer unit, resulting in a temperature drop in the brine from 110℃ to 86.5℃. Concurrently, the cold inlet LiPSS stream heats up from 28℃ to 85℃, the operating temperature of the electrolyzer, at a flow rate of 341,000 kg/hr.

The heat exchanger H-101 is directly followed by pump P-104 that drives the flow of the LiPSS stream into each electrolyzer unit. With a flow rate of 341,000 kg/hr of LiPSS passing through each pump, as there are two electrolyzers running in parallel, there is a discharge pressure of 1.52 barg and a power requirement of 23.6 kW.

Both electrolyzer units, E-103, are made of titanium with a power requirement of 2.2 MW each, resulting in a total power requirement of 4.4 MW. The total reduction potential of the

reaction is -1.6 V, with a required overpotential of 0.6 V. This leads to an operating voltage of 2.2 V. Based on the desired production rate of LiOH with a value of 651 kg/hr per cell, the ideal current amount is 722,000 A. Considering 73% current efficiency, the operating current is 985,800 A. The required effective area for the nickel cathode is 410 m^2 and the required graphite anode effective area is 821 m^2.

A purge stream of 10%, with a total flow rate of 68,100 kg/hr, is used in order to remove NaCl from the recycle stream. As a result, a makeup stream of $FeCl_3$ solution with a total molar flow rate of 68,100 kg/hr. There is therefore a 7790 m^3 storage tank Tk-103 made of HDPE for the $FeCl_3$ solution. The recycle stream further requires a titanium centrifugal pump P-106 that has a power requirement of 241 kW and a discharge pressure of 8 barg assuming a total flow rate of 681,000 kg/hr.

The produced H_2, at a flow rate of 28 kg/hr per electrolyzer unit, is sent to a hydrogen fuel cell E-104 with an efficiency of 60%. The fuel cell, made of carbon steel, produces 1.14 MW of total electricity. This fuel cell cell operates at 25℃ and 1 atm.

5.4 Crystallization

The aqueous stream of lithium hydroxide and sodium hydroxide impurity produced by electrolysis is sent to the evaporative crystallizer in the fourth process stage. This process stage evaporates the water from the aqueous solution to form the final battery grade lithium hydroxide monohydrate solid for distribution. The inlet stream to the crystallizer is at 85°C and 1 atm and the crystallizer at 120°C and 1 atm. The water evaporated from solution vents as vapor to the atmosphere at a rate of 9,483.34 kg/hr. Additionally, the total power requirement is 5.59 MW.

Table 23. Material Balance Around Crystallizer E-105 (kg/hr)

Stream		**19**	**20**	**21**
IN/OUT		IN	OUT	OUT
Phase		Aqueous	Vapor	Solid
Mass Flow (kg/hr)		11,787.32	9,483.34	2,303.98
Component Flow (kg/hr)	**H_2O**	10,463.11	9,483.34	979.77
	LiOH	1,302.55	—	1,302.55
	NaOH	21.66	—	21.66

Table 24. Equipment Summary for Crystallization

Equipment ID	**Name**	**Material of Construction**	**Design Specifications**
E-105	Crystallizer	Stainless Steel 304	1.70 m diameter, 0.037 m inlet radial port diameter,
P-107	LiOH solution to Crystallizer	Stainless Steel 304	0.53 kW, 1.01 barg
Tk-104	LiOH·H2O Storage	Stainless Steel 304	500 m^3

Table 23 summarizes the material balance surrounding the unit. Table 24 summarizes the crystallizer equipment. Pump P-107 pumps the LiOH-rich outlet stream from the electrolyzer units towards the evaporation and crystallization unit. There is no pressure difference between the electrolyzer unit and the evaporation and crystallization unit, but there is an assumed 0.505 bar

pressure loss due to flow through pipes and an assumed 0.505 bar pressure loss due to control valves. This results in a discharge pressure of 1.01 barg. The LiOH-rich solution passes through pump P-107 at a flow rate of 3.27 kg/s or 0.003 m^3/s which results in a power requirement of 0.54 kW.

SECTION 6: ECONOMICS

We performed an economic analysis to determine the overall viability of the lithium extraction and purification design process. By calculating capital, operating and materials costs, and expected revenues, the net present value and corresponding internal rate of return (IRR) serve as indicators of profitability of the plant. To calculate capital costs, most of the prices for equipment were found using Capcost 2001 from Turton, which is a Microsoft Excel spreadsheet that has a copious database for various materials of construction and process units. The Chemical Engineering Plant Cost Index (CEPCI), a tool to adjust plant construction costs over different time periods that accounts for equipment, construction labor, buildings, and engineering/supervision, was listed as 397 in Capcost. In order to scale to represent 2023 prices with a CEPCI of 800, we used the purchased equipment cost obtained from Capcost. For raw materials and utility costs, we used prices based on the cheapest bulk cost available at market price. The calculated projected revenue was found entirely from sales of battery-grade lithium hydroxide monohydrate ($LiOH \cdot H_2O$) with a purity of 99 weight percent. Finally, for the discounted cash flow (DCF) analysis, the plant was assumed to run for 20 years with a 7-year straight-line depreciation schedule.

6.1 Mixing Unit

6.1.1 Capital Costs

The mixing unit involves four main pieces of equipment: the vessel, propeller, screw conveyors and storage tanks. For material costs, the only streams to consider involve the inlet citrate and added $FeCl_2$ as the brine feed comes directly from the reinjection well at zero cost. The equipment consists of the main vessel and the impeller; the vessel price itself was calculated from Capcost 2001 while the propeller price was calculated based on power requirements from the Towler and Sinnott textbook. Assuming that the inlet brine feed is at a sufficiently high pressure that does not require additional pumps to reach the mixing unit from the well, the use of a pump is neglected.

The price of screw conveyors is also included in order to transport the tripotassium citrate and ferrous chloride in powder form. The calculated power of the screw conveyor, for the purpose of pricing, is modeled through Equation 35:

$$P = 0.07 * m^{0.85} * L \quad (35)$$

where P is the power required, m is the mass flow rate, and L is the length of the conveyor. The chosen length for all screw conveyors is 10 m which moves across at a speed of 2 m/s (Blackwood, 2023).

The screw conveyor associated with transporting citrate and ferrous chloride is modeled as baking powder and ferrous sulfate respectively in the KWS manufacturing calculator to calculate the required diameter specifications for costing (*Screw Conveyor Interactive Calculators*). The total purchased equipment cost, scaled for 2023, of $4,525,329 is further broken down in Table 25 on the following page.

Table 25. Cost Breakdown of Mixing Unit Equipment, scaled for 2023

Equipment ID	Name	Material of Construction	Design Specifications	Cost, $
C-101	Cooling Tower for inlet brine	PVC	2 x 427 L/s	867,314 (Towler and Sinnott, 2012)
Cv-101	Screw Conveyor for Citrate	Stainless Steel 304	2.4 kW, 10 m	21,857 (Dutch Association of Cost Engineers, 2016)
Cv-102	Screw Conveyor for $FeCl_2$	Titanium	0.44 kW, 10 m	75,541 (Dutch Association of Cost Engineers, 2016)
E-101	Mixing Vessel	Titanium	2x2 m, vertical	114,966 (Turton CAPCOST, 2018)
	Propeller	Stainless Steel 304	273 kW	1,277,135 (Towler and Sinnott, 2012)
P-101	Brine to PBR	Titanium	641 kW, 11 barg	1,836,171 (Turton CAPCOST, 2018)
Tk-101	Citrate Storage	Carbon Steel	2700 m^3	312,343 (Turton CAPCOST, 2018)
Tk-102	$FeCl_2$ Storage	HDPE	250 m^3	20,002 (Turton CAPCOST, 2018)
			Total	4,525,329

6.2 Packed Bed Reactor System

6.2.1 Capital Costs

The capital equipment required for the packed bed reactor system includes two pumps, cooling tower system, four vessels, and a reverse osmosis unit. Before entering the packed bed reactor (PBR) system network, the brine must pass through three cooling towers to lower the temperature from 86°C to 28°C. A centrifugal pump is also necessary to drive the brine solution to the packed bed reactor system while accounting for a 10 bar pressure drop in each reactors. Another centrifugal pump is required to reinject the spent brine, which is the remaining solution that does not get adsorbed in the PBR, into the injection well. A reverse osmosis unit is also incorporated into the design to purify the exiting water that leaves the reactor following washing. The capital equipment costs are outlined in Table 26 below and sum to $2,910,489.

Table 26. Cost Breakdown of Packed Bed Reactor System Equipment, scaled for 2023

Equipment ID	Name	Material of Construction	Design Specifications	Cost, $
C-102	Cooling Tower for Recycle Stream	PVC	189 L/s	281,766 (Towler and Sinnott, 2012)
E-102	Reverse Osmosis	Stainless Steel 304	1000 m^3/day	31,500 (Alibaba, 2023)
P-102	Spent Brine to Well	Titanium	641 kW, 11 barg	1,836,171 (Turton CAPCOST, 2018)
P-103	Wash Water to PBR	Stainless Steel 304	98 kW, 51 barg	102,771 (Turton CAPCOST, 2018)
P-105	$FeCl_3$ from Storage to PBR	Titanium	3.01 kW, 1.01 barg	77,284 (Turton CAPCOST, 2018)
R-101	PBR	Titanium	4, 3.6 x 1.79 m, vertical vessels	580,997 (Turton CAPCOST, 2018)
			Total	2,910,489

6.3 Electrolysis

6.3.1 Capital Costs

The electrolysis stage of the process consists of two electrolyzer units, three centrifugal pumps, two heat exchangers, and a hydrogen fuel cell. Directly following the packed bed reactor system, the lithium pregnant stripping solution (LiPSS) is split and passed through a heat exchanger (two in parallel) and centrifugal pump (two in parallel). The heat exchanger brings the temperature of the solution up from 28℃ to 85℃ which are the conditions of the electrolyzer unit. The final pump is required to pump the recycled $FeCl_3$ solution back to the stripping unit in the PBR system. Utilizing centrifugal pumps further drive the lithium pregnant stripping solution into the electrolyzer units. Additionally, a hydrogen fuel cell is used in order to convert the produced H_2 from electrolysis into usable energy. A more detailed breakdown of the capital costs are outlined below in Table 27. In total, the final capital costs associated with the electrolyzer unit is $10,649,054.

Table 27. Cost Breakdown of Electrolyzer Equipment, scaled for 2023

Equipment ID	Name	Material of Construction	Design Specifications	Cost, $
E-103	Electrolyzers	Titanium	2 x 2.2 MW	3,340,550 (Irena, 2020)
E-104	Hydrogen Fuel Cell	Carbon Steel	1.14 MW	1,990,876 (Mongird et al., 2020)
H-101	PSS Cooler	Titanium/ Titanium	4x1000 m^2, 2 in series, 2 in parallel	4,220,453 (Turton CAPCOST, 2018)
P-104	PSS to Electrolyzer	Titanium	23.6 kW, 1.52 barg, 2 in parallel	309,683 (Turton CAPCOST, 2018)
P-105	Recycle from Electrolyzer to PBR	Titanium	241 kW, 8.01 barg	671,436 (Turton CAPCOST, 2018)
Tk-103	$FeCl_3$ Solution Storage	HDPE	7800 m^3	116,056 (Turton CAPCOST, 2018)
			Total	10,649,054

6.4 Crystallization

6.4.1 Capital Costs

The main capital costs for crystallization include the crystallization unit, pump, and lithium hydroxide monohydrate storage tank. Following the electrolyzer, the resulting lithium hydroxide solution must be pumped to the crystallization unit. The capital costs are outlined in Table 28 below. Additional washing and drying costs are not included as the high achieved purity of 99 wt.% for lithium hydroxide monohydrate warranted no need for further design considerations. The total capital costs associated with crystallization is $403,615.

Table 28. Cost Breakdown of Crystallization Equipment, scaled for 2023

Equipment ID	Name	Material of Construction	Design Specifications	Cost, $
E-105	Crystallizer	Stainless Steel 304	1.3 m	109,005 (Towler and Sinnott, 2012)
P-107	LiOH solution to Crystallizer	Stainless Steel 304	0.53 kW, 1.01 barg	19,748 (Turton CAPCOST, 2018)
Tk-104	LiOH·H2O Storage	Stainless Steel 304	500 m^3	274,861 (Turton CAPCOST, 2018)
			Total	403,615

6.5 Final Capital and Plant Costs

The final total capital cost amounts to $18,488,487. Considering a Lang factor of 6.05 that takes into account equipment erection, piping, instrumentation and control, electrical, civil, structures and buildings, lagging and paint as well as offsites, design and engineering and contingency, for a fluids-solids process the project fixed capital plant cost is $111,855,349 (Towler and Sinnott, 2012). This was calculated using Equation 36.

$$C = F * \sum Ce \quad (36)$$

where F is the Lang Factor and Ce is the total costs of all major equipment items. After factoring in the location factor of California, as the used baseline location is the Gulf Coast, the final fixed capital cost amounts to $119,685,223.

6.6 Operating Costs

The yearly operating costs were calculated by determining the annual consumables or raw materials cost, labor cost, maintenance cost, utilities, and site overhead cost. As our process is combined with an existing geothermal power plant, additional land costs are not included in the operating costs.

Table 29. Breakdown of Yearly Operating Costs

Yearly Cost	$/year
Consumables	$169,397,540.44
Utilities	$ 3,733,633.17
Labor	$ 5,310,240.00
Maintenance	$ 10,238,220.00
Site Overhead	$ 1,241,102.00
Total:	$189,920,735.61

The total operating costs are displayed above in Table 29. The breakdown for the consumables cost and the utilities cost is detailed in sections 6.6.1 and 6.6.2 respectively. Labor, maintenance, and site overhead costs were provided through personal communication with Prof.

Koenig based on a similar process plant (personal communication, March 13, 2023). The operating costs per ton of lithium hydroxide monohydrate produced amounts to $10,350 when considering the use of tripotassium citrate monohydrate; without the citrate, the operating cost per ton of lithium hydroxide monohydrate produced is $2,773 which is slightly lower than the industry average of $3,660 (Warren, 2021). Thus, seeking alternatives to citrate is an important future step for minimizing materials costs. In terms of water cost per ton of lithium hydroxide monohydrate produced, our process corresponds to $1,190; without cooling towers, this amount is $95 in comparison to the higher industry average of $177 (Warren, 2021). Testing the packed bed reactor unit at temperatures closer to the operating temperature of the electrolyzer unit can eliminate the need for cooling towers and therefore reduce the costs associated with water. It is important to note that the reported industry average takes into account pre-treatment of the brine whereas our process starts after pre-treatment.

6.6.1 Consumables Cost

The consumables included in the operating costs include makeup water for cooling towers C-101 and C-102, additives for mixing unit E-101, makeup water for reactor washing, makeup ferric chloride solution in the recycled stripping solution following the purge, and sorbent losses in the packed bed reactors.

Table 30. Breakdown of Consumables Costs

Consumable	Amount (MT/year)	$/MT	$/year
C-101 Makeup Water (Stream 5)	1,063,120.50	$0.21	$225,806.79
C-102 Makeup DI Water (Stream 13)	554,737.47	$17.40	$9,652,431.89
$FeCl_2$ Powder (Stream 3)	6,129.07	$600.00	$3,677,441.97
Potassium Citrate Monohydrate Powder (Stream 3)	139,046.53	$1,000.00	$139,046,533.90
Makeup Washing DI Water (Stream 9)	100,327.00	$17.40	$1,745,689.81
Makeup .1M Ferric Chloride Solution (Stream 15)	596,433.63	$25.01	$14,914,289.27
Makeup Sorbent Losses	13.53	$10,000.00	$135,346.80
Total:			$169,397,540.44

Table 30 details the costs for consumables. The prices for process water and DI water were taken from Table 8.3 in Turton et al. and multiplied by 1.2 to account for inflation between 2018 and 2023 (Turton et al., 2018). The selected bulk prices for $FeCl_2$ powder (*Ferrous chloride*), potassium citrate monohydrate powder (*Potassium citrate monohydrate*), and the sorbent are listed above (*High purity ferric phosphate*). The sorbent losses are estimated at 30% per year. Since ferric chloride solution is not typically sold at low molarities, the 0.1M ferric chloride solution price was extrapolated from the price of bulk ferric chloride powder found online and the price of DI water from Turton et al. adjusted for inflation (Turton et al., 2018). The potassium

citrate monohydrate powder exists as the most expensive operating cost, so we recommend further testing on the necessity of citrate for this process.

Table 31. Summary of Starting Materials Costs

Material	Amount (MT)	$/MT	Cost
.1M Ferric Chloride Solution	$ 680.87	$ 25.01	$ 17,025.75
Washing DI Water	$ 43.45	$ 17.40	$ 755.99
Sorbent	$ 45.12	$ 10,000.00	$ 451,156.00
	Total:		$ 468,937.74

The startup materials costs are displayed above in Table 31. The process requires an initial ferric chloride solution that is recycled through sorbent stripping, an initial washing water flow that is recycled through reverse osmosis unit E-102, and initial sorbent in the packed bed reactors.

6.6.2 Utilities Cost

The utilities included in the operating costs include electrical power required for the mixing unit, screw conveyors, electrolyzers, and pumps. The power generated by the hydrogen fuel cell in the process is subtracted from the power requirements of the other units. In addition to electrical power, low pressure steam is required for the crystallization unit.

Table 32. Breakdown of Utilities Costs

Equipment ID	Power Requirement (kW)	Power Requirement (kWh)	$/kWh	$/year
E-101	270.00	2,170,800.00	$ 0.08	$ 175,574.30
Cv-101	2.40	19,296.00	$ 0.08	$ 1,560.66
Cv-102	0.44	3,537.60	$ 0.08	$ 286.12
E-103	4,330.00	34,813,200.00	$ 0.08	$2,815,691.62
E-104	-1,140.00	-9,165,600.00	$ 0.08	$ (741,313.73)
E-105	5,590.00	44,943,600.00	$ 0.01	$ 394,105.87
P-101	641.43	5,157,097.20	$ 0.08	$ 417,106.02
P-102	641.28	5,155,891.20	$ 0.08	$ 417,008.48
P-103	98.02	788,080.80	$ 0.08	$ 63,739.98
P-104	47.14	379,005.60	$ 0.08	$ 30,653.97
P-105	3.01	24,200.40	$ 0.08	$ 1,957.33
P-106	241.30	1,940,052.00	$ 0.08	$ 156,911.41
P-107	0.54	4,341.60	$ 0.08	$ 351.15
	Total:			$3,733,633.17

Table 32 details the costs for utilities. The prices for electrical power and low pressure steam were taken from Table 8.3 in Turton et al. and multiplied by 1.2 to account for inflation between 2018 and 2023 (Turton et al., 2018). Crystallizer E-105 is the only process unit requiring steam. The electrolyzer E-103 and pump P-104 include the power requirement for two of each respective unit. The two electrolyzers represented by E-103 contain the greatest power requirements and make up 75% of the total utilities costs. The total power requirement, ~10.7 MW, is 21% of the 50 MW geothermal power plant. Heat exchanger H-101 uses the raw brine as the heat source, so this is not included in Table 32. The power requirement for reverse osmosis unit E-102 is included in pump P-103.

6.7 Discounted Cash Flow Analysis

The projected revenue for this process is calculated using Equation 35.

$$Revenue = (Units/year) * (Price/Unit) \quad (35)$$

The price of battery grade lithium hydroxide monohydrate as of March 23, 2023 is $65/kg (*About lithium*, 2023). Assuming 30 days of planned shutdown, there will be 335 days of continuous production. Therefore, we expect to produce 18,348,923 kg of battery grade lithium hydroxide monohydrate. Using Equation 35, our annual revenue is calculated as $1,192,680,019 assuming we meet all projected demand. The federal corporate tax rate is 21% and the California corporate tax rate is 8.84%. The total corporate tax rate is calculated as 29.84%.

Table 33. 20-Year Economic Summary of Discounted Cash Flow Analysis with a Discount Rate of 592%

Year	Costs	Depreciation	Revenue	Cash Flow	Taxed Amount	Post-Tax Cash Flow	Post-Discount	Total Cash Position
0	$119,685,223.00	$0.00	$0.00	($119,685,223.00)	$0.00	($119,685,223.00)	($119,685,223.00)	($119,685,223.00)
1	$190,389,673.35	$17,097,889.00	$1,192,680,019.44	$985,192,457.09	$293,981,429.20	$708,308,916.89	$102,384,917.09	$588,623,693.89
2	$190,389,673.35	$17,097,889.00	$1,192,680,019.44	$985,192,457.09	$293,981,429.20	$708,308,916.89	$14,799,575.43	$1,296,932,610.79
3	$190,389,673.35	$17,097,889.00	$1,192,680,019.44	$985,192,457.09	$293,981,429.20	$708,308,916.89	$2,139,254.88	$2,005,241,527.68
4	$190,389,673.35	$17,097,889.00	$1,192,680,019.44	$985,192,457.09	$293,981,429.20	$708,308,916.89	$309,225.86	$2,713,550,444.58
5	$190,389,673.35	$17,097,889.00	$1,192,680,019.44	$985,192,457.09	$293,981,429.20	$708,308,916.89	$44,698.10	$3,421,859,361.47
6	$190,389,673.35	$17,097,889.00	$1,192,680,019.44	$985,192,457.09	$293,981,429.20	$708,308,916.89	$6,461.04	$4,130,168,278.37
7	$190,389,673.35	$17,097,889.00	$1,192,680,019.44	$985,192,457.09	$293,981,429.20	$708,308,916.89	$933.93	$4,838,477,195.26
8	$190,389,673.35	$0.00	$1,192,680,019.44	$1,002,290,346.09	$299,083,439.27	$703,206,906.82	$134.03	$5,541,684,102.08
9	$190,389,673.35	$0.00	$1,192,680,019.44	$1,002,290,346.09	$299,083,439.27	$703,206,906.82	$19.37	$6,244,891,008.89
10	$190,389,673.35	$0.00	$1,192,680,019.44	$1,002,290,346.09	$299,083,439.27	$703,206,906.82	$2.80	$6,948,097,915.71
11	$190,389,673.35	$0.00	$1,192,680,019.44	$1,002,290,346.09	$299,083,439.27	$703,206,906.82	$0.40	$7,651,304,822.53
12	$190,389,673.35	$0.00	$1,192,680,019.44	$1,002,290,346.09	$299,083,439.27	$703,206,906.82	$0.06	$8,354,511,729.34
13	$190,389,673.35	$0.00	$1,192,680,019.44	$1,002,290,346.09	$299,083,439.27	$703,206,906.82	$0.01	$9,057,718,636.16
14	$190,389,673.35	$0.00	$1,192,680,019.44	$1,002,290,346.09	$299,083,439.27	$703,206,906.82	$0.00	$9,760,925,542.98
15	$190,389,673.35	$0.00	$1,192,680,019.44	$1,002,290,346.09	$299,083,439.27	$703,206,906.82	$0.00	$10,464,132,449.79
16	$190,389,673.35	$0.00	$1,192,680,019.44	$1,002,290,346.09	$299,083,439.27	$703,206,906.82	$0.00	$11,167,339,356.61
17	$190,389,673.35	$0.00	$1,192,680,019.44	$1,002,290,346.09	$299,083,439.27	$703,206,906.82	$0.00	$11,870,546,263.43
18	$190,389,673.35	$0.00	$1,192,680,019.44	$1,002,290,346.09	$299,083,439.27	$703,206,906.82	$0.00	$12,573,753,170.24
19	$190,389,673.35	$0.00	$1,192,680,019.44	$1,002,290,346.09	$299,083,439.27	$703,206,906.82	$0.00	$13,276,960,077.06
20	$190,389,673.35	$0.00	$1,192,680,019.44	$1,002,290,346.09	$299,083,439.27	$703,206,906.82	$0.00	$13,980,166,983.88

The 20-year economic summary is displayed above in Table 33. Depreciation of capital costs reflect a 7-year straight line depreciation schedule. The initial capital investment is reflected as the cost for year 0. The starting materials cost is included with the operating costs per year to account for planned shutdown. A discounted cash flow analysis is performed based on a 7-year straight-line depreciation schedule and a plant lifetime of 20 years. To perform this analysis, the net present value (NPV) was calculated and minimized to zero using Microsoft Excel's Solver tool by adjusting the internal rate of return (IRR). The formula for calculating the NPV is displayed below in Equation 36.

$$NPV = \sum \frac{CF}{(1+r)^n} \quad (36)$$

where CF represents the cash flow, r represents the IRR, and n represents the number of years.

A sensitivity analysis is performed at lower prices to identify different economic scenarios. Since this process is expected to manufacture a substantial amount of lithium hydroxide monohydrate, our product may need to be sold at lower prices to successfully enter the lithium market. We identified price points of $19.28/kg and $13.08/kg to achieve payback periods of one and three years, respectively, to analyze the lower bounds of our product price.

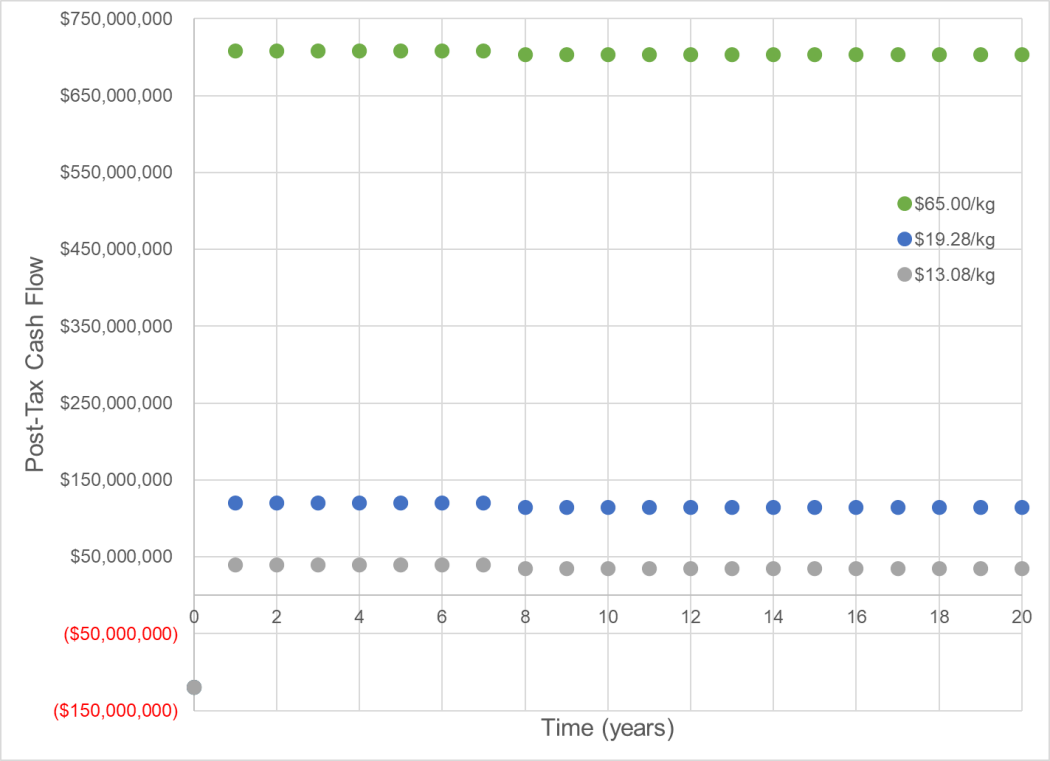

Figure 17. Post-Tax Cash Flow Based on a 7-Year Straight-Line Depreciation Schedule and a 20 Year Plant Lifetime

The post-tax profit is displayed in Figure 17 using the discounted cash flow analysis from Table 33.

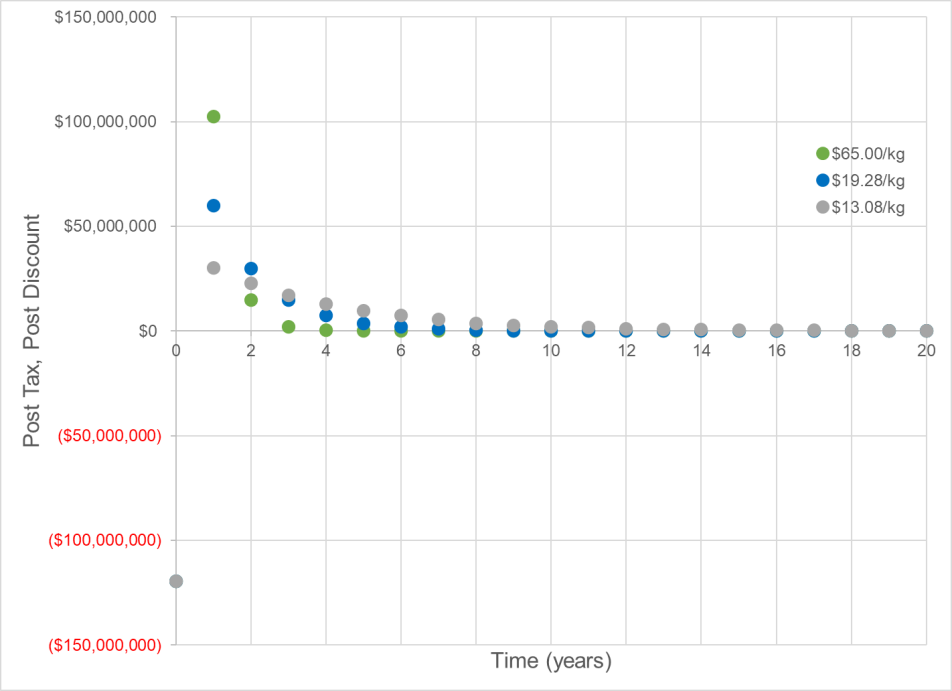

Figure 18. Discounted Cash Flow Over Time

Figure 18 displays the results of our discounted cash flow analysis. At all three price points, the discount is expected to be paid off reasonably within 20 years.

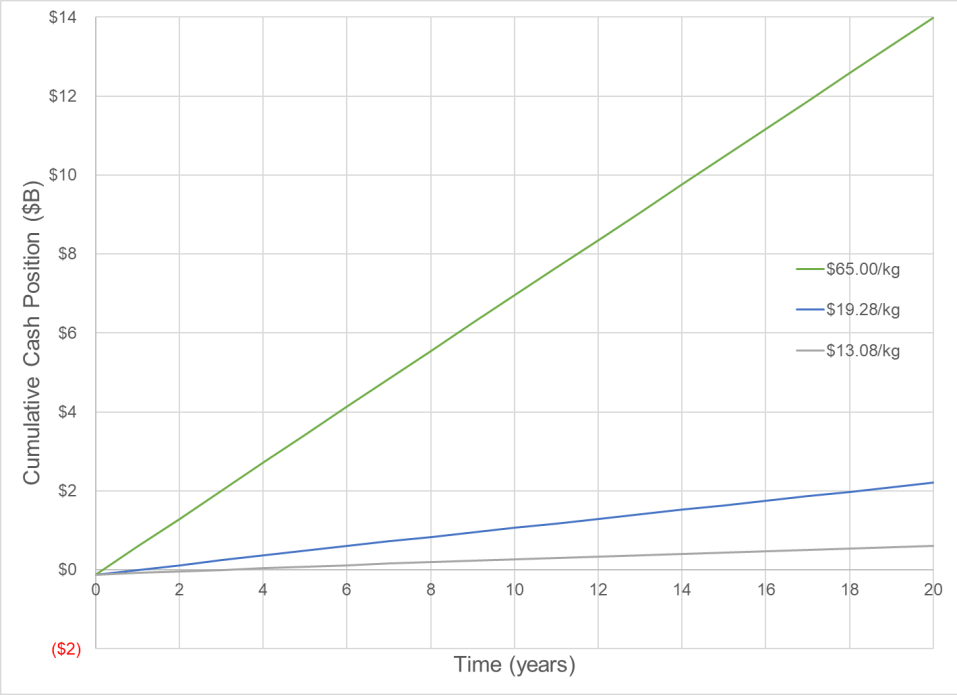

Figure 19. Cumulative Cash Position Based on a 7-Year Straight-Line Depreciation Schedule and a 20 Year Plant Lifetime

Figure 19, above, displays the cumulative cash position based on this discounted cash flow analysis. At all three price points, a significant profit is expected after 20 years. At a $65/kg price point, we expect approximately $14 billion after 20 years. In the most conservative case of a $13.08/kg product price, we expect $612 million after 20 years.

Table 34. Sensitivity Analysis Comparing Three Different Product Price Points

$LiOH \bullet H_2O$ Bulk Price ($/kg)	IRR (%)	ROI (%)	Payback Period (years)
65.00 (100%)	592	11,700	0.17
19.28 (30%)	100	1,840	1
13.08 (20%)	32.6	511	3

Table 34 displays the IRR, return on investment (ROI), and payback period for three product price points. At prices much lower than $65/kg, a large ROI is still expected. Based on this discounted cash flow analysis, a profit is expected after only two months. Further, even at the lowest price point available on the market, the payback period of 3 years is still a very attractive investment opportunity. The IRR is determined to be 592% at a price point of $65/kg. The return

on investment (ROI) is determined to be 11,700% over 20 years with a final cumulative cash position of $13,980,166,984.

SECTION 7: ENVIRONMENTAL, SAFETY, AND SOCIAL CONSIDERATIONS

7.1 Environmental Considerations

Primary lithium extraction pathways currently include extraction from hard rock pegmatites, extraction from sedimentary rock such as clays, or evaporation from arid basin brines (Blair et al., 2022, p. 4). Arid basin brine lithium sourcing faces particular criticism for its heavy water requirements within the internationally recognized wetlands of Chile, Argentina, and Bolivia; for its ecological disruption to migratory and native species; and for its exploitation of indigenous and local people's land (Blair et al., 2022, p. 4). Lithium extraction from geothermal brine offsets the environmental damages of historical lithium extraction methods particularly as the proposed scheme would be added to existing geothermal operations; thus, minimizing the process ecological impact versus new plant construction. This process additionally has lessened water intensity compared to purely evaporative schemes. Energy integration decreases process energy intensity. Reinjection of the geothermal brine after processing should minimize concerns related to subsidence and seismicity; however, we recommend continual monitoring of land stability and activity (DiPippo, 1978, p. 35).

While offsetting the environmental damages of historical lithium extraction methods, extraction from geothermal brine is not without negative consequence. The expansion of domestic lithium mining raises legal and environmental debate between mining interests and local groups seeking to protect the micro-ecosystems mining threatens, as seen in Bartell Ranch LLC v. McCullough (2023). The Bureau of Land Management’s approval of a lithium mining project at Thacker Pass faced heavy resistance from local environmental, indigenous, and ranching coalitions. Land co-stewardship policies allowing voice to local interests may mitigate resistance in Salton Sea development projects.

Noise propagation concerns arise from “water falling in a cooling tower, mechanical fans, venting steam, electric generators, etc.” (Kelly, 1975, p. 19). Analysis by Kelly, Lawrence Livermore National Laboratory, indicates that noise pollution to populated areas in the Imperial Valley is most concerning during November through February based upon wind velocity and

direction (1975). While Kelly concluded that noise propagation at the time of authorship, 1975, was not a significant issue, regional development particularly as lithium speculation increases may force greater consideration.

7.2 Safety Considerations

In considering the hazardous chemicals present throughout the process units, the compounds of concern with the corresponding properties are highlighted in Table 34.

Table 34. Chemical and Hazard Information of Process Compounds

Compound Name	Flammability	Corrosivity	OSHA Limits	Incompatibilities	Storage Considerations
$FeCl_3$	Not flammable (Contact with metals may evolve flammable H_2 gas)	Acidic and corrosive to most metals	1 mg/m^3	Avoid contact with metals, bases, halocarbons and combustible materials	Store in fiberglass/plastic tanks Use PVC or FRP pipes
$FeCl_2$	Not flammable (Contact with metals may evolve flammable H_2 gas)	Corrosive to metals and skin	1 mg/m^3	Ethylene oxide	Dry, well-closed. Separated from strong oxidants/alcohols
NaOH	Not flammable	Very corrosive to aluminum metal	2 mg/m^3	Acid. generates heat when diluted with water	Separated from strong acids and metals. Store in original container.
LiOH	Not flammable (Contact with metals may evolve flammable H_2 gas)	Corrosive	N/A	Strong acids, oxidizing agents	Keep under nitrogen blanket, in closed container
H_2	Highly flammable	Non-corrosive	N/A	Calcium, barium, and strontium Oxygen, halogens, other oxidizing materials	Fireproof, cool and well-ventilated location

Note. The data for $FeCl_3$, $FeCl_2$, NaOH, LiOH, and H_2 are from U.S. National Library of Medicine. (n.d.) National Center for Biotechnology Information. PubChem Compound Database.

After considering the hazards associated with the compounds of concern, the appropriate storage and handling methods are implemented. The only flammable material of concern is H_2 gas which leaves the electrolyzer unit and is transferred to the hydrogen fuel cell where electricity is generated. Due to its high flammability and incompatibilities with calcium, barium, strontium, oxygen and halogens, the H_2 stream will not be in close-contact with any of the aforementioned chemicals. In consideration of the highly-corrosive nature of select process chemicals including $FeCl_3$, NaOH, and LiOH, the intended material of construction for units involving those compounds will be titanium and HDPE. It is also important to wear proper protective equipment (PPE) when handling such materials, such as chemical safety goggles, gloves, and protective clothing. Given the co-location with a geothermal power plant, hard hat and steel-toe shoes must be worn as necessary.

Regarding potential equipment failures in the mass transfer space, leaks can occur as a result of corrosion or flange leaks (Unnerstall, 2022). This process requires regular inspection, hydrotesting, and proper maintenance techniques for mitigating leaks and toxic releases. In reactors, a loss of cooling, loss of agitation, overcharge of reactant or catalyst, contamination or a step done out of sequence is possible. Emergency relief systems and back-up cooling for mitigating loss of cooling are essential design safeguards to prevent and mitigate potentially harmful consequences. For storage tanks, a loss of containment of $FeCl_3$ is possible from overfilling or mechanical failure. Potential safeguards include the installation of level alarms or interlocks, secondary containment tanks, or overflow lines that are separate from vent lines. For pumps, potential failure modes include stopping, deheading, and cavitation which are caused by power failures, blocked outlets, blocked suction, respectively. The implementation of low-flow alarms, overpressure protection and vibration monitors will help mitigate the probability of catastrophic failures.

The PEM electrolyzer unit in particular should be composed of materials resistant to chemical, thermal and mechanical exposure, as well as consist of pressure bearing components and piping that fits regulatory requirements. The use of a ventilation system will further mitigate accidental releases and leakages of H_2 or other gasses (Hotellier and Becker, 2013). Utilizing leak proof connections prevents accumulation of an explosive atmosphere. Additional safety measures include installing temperature sensors, pressure sensors, pressure relief devices and hydrogen-gas detection systems to monitor the reaction and overall process unit. Grounding is also essential to

prevent electric shock. The ambient temperature fluctuates annually between -7 to 46°C (20 to 115°F). This necessitates forced ventilation of electrical equipment during the hottest months (DiPippo, 1978, p. 24).

Considering the overall nature of geothermal power plants, the location near fault zones or “hot spots” makes the location more unstable and susceptible to earthquakes (Soltani et al., 2021). Thus, it is important to build earthquake-resistant structures to create a safe space for evacuation as necessary.

7.3 Social Considerations

Lithium extraction from geothermal brine offers increased domestic lithium supply; thus, diminishing reliance on foreign sources. Trade imbalance owing to lithium's highly polarized global distribution will cause "geostrategic bottlenecks" (Grosjean et al., 2015), as shown in Figure 20. Geothermally derived lithium offers a steady domestic source during a time of rapid scale-up. Lithium mining processes with sufficient technological feasibility are likely to be heavily subsidized by either private or public actors, or both.

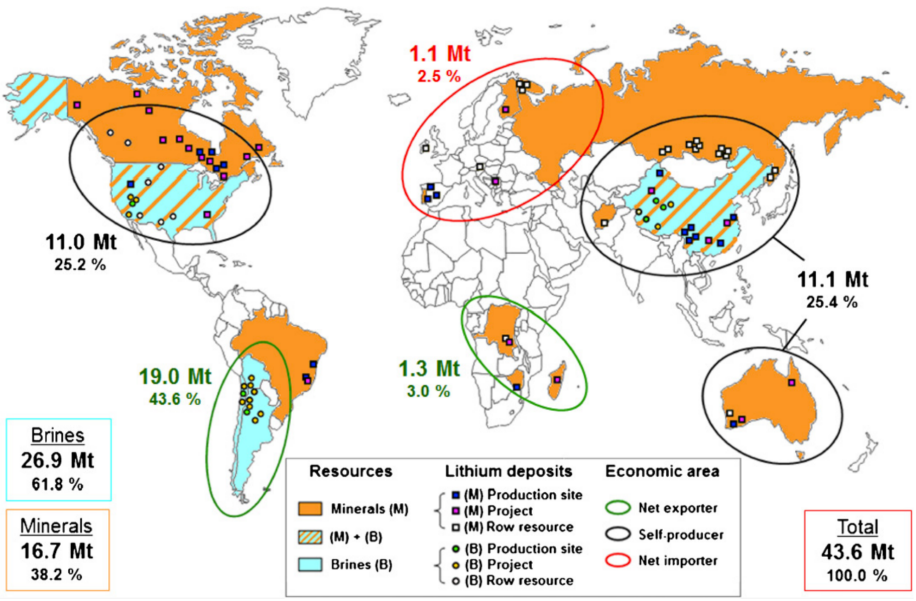

Figure 20. Map of Lithium Resource Availability and Geostrategic Impacts (Grosjean et al., 2012)

Classification of geothermal resource ownership and jurisdiction is legally complicated. Lands containing geothermal resources can be divided between a surface and a mineral estate. Legal disputes often trace estate lease agreements back decades, in some cases to the 1950's when geothermal exploitation in the American west began (Kennecott Corp. v. Union Oil Co., 1987). Geothermal resource water rights remain undecided between estate parties and are often reliant on the phase and source of geothermal water present or if the resource is located on federal, state, or

private land (Silver & Comeau, 1979, p. 446). 1977 analysis by NASA's Jet Propulsion Laboratory writes:

> [Geothermal development] requires an interrelationship among explorer, developer, and user that has not previously been required. This requirement emerges not only because of technical factors in extraction and use, but also because of an increasing awareness by local governments and private citizens of the consequences of major development activities [...] As is becoming typical in our country, industry, government, and concerned citizens square off in an advocacy proceeding with their own experts who attempt to discredit either the research tool, the procedure, or the interpretation of the results. There should be no expectation that geothermal energy development will foster a different environment. (p. 38-39)

Today, increasing competition and marketability for mineral extraction process knowledge, geochemical data, and mineral technologies disincentivize collaboration between actors within a complicated geo-political and technical regulatory space (Williams, 2022). Coordination between actors operating at the federal, state, local, and private levels is essential for rapid and equitable geothermal exploration.

SECTION 8: CONCLUSION & RECOMMENDATIONS

8.1 Conclusion

The process and plant designed within this report should be strongly considered as a promising candidate for implementation and investment. Further work should be done to finalize chemical and plant scale specifications, but the overall profitability suggests this is a worthwhile investment of time and resources. The IRR for this project is 592%, assuming the final lithium hydroxide monohydrate product is sold as battery grade. This translates to a payback period of just 2 months. As is, the final purity of our product is 99.06 wt%, which meets the original 99 wt% purity requirement. The purity reached for this process is largely dependent on the many assumptions that were made throughout the design process. This criteria should be reevaluated once more specific designs are completed. The overall recovery of lithium throughout processing is 99 wt%, accounting for small losses at the point of reinjection following the adsorption reaction.

Extracting lithium from geothermal brines has advantages over current extraction methods like evaporation. The chemical sorption and electrochemical conversion in this process have a lower water use and minor additional land use beyond the existing power plant. The identification of ownership of brine can be included in existing agreements for the power plant. Local populations are already familiar with the power plant adjacent to their livelihoods, so less resistance is expected than if a new plant were to be constructed. Creating a national supply chain of lithium will be key in the coming years as lithium ion batteries gain popularity and demand with inclusion in electric vehicle manufacturing. The market associated with raw mineral extraction is unstable causing price variations; this is likely to be exacerbated as demand rises and suppliers are motivated to increase sourcing. By implementing the process designed in this report, future expansions into the lithium extraction industry can have less negative societal effects while remaining extremely profitable.

8.2 Recommendations

Further research recommendations are listed below to transition the theoretical design in this report to a complete and implementable plant design. Many of the designs presented were based on multiple assumptions due to lack of available data. Recommendations to close these gaps are listed below in order of perceived importance and categorized by the major equipment they correspond with.

8.2.1 Mixing Unit Recommendations

1. Further testing the effect of additives on brine pH and sorbent performance beyond a pH 3-5 range to eliminate pH balancing additives.
2. Measure the chemical potential of brine without citrate ion addition. If existing elemental concentrations in the brine act as a sufficient redox shuttle, it would eliminate the need to buy and mix potassium citrate, a major chemical cost.
3. If an external redox shuttle is required, we recommend experimentation into the effect of citrate concentration on the brine chemical potential and the ability for other compounds to achieve the same potential drop with less precipitation or lower concentration/cost.
4. Further inclusion of trace elements (aluminum, ammonia, antimony, arsenic, barium, copper, fluoride, magnesium, silica, silver, sulfate, and strontium) in the synthetic brine for more accurate process design and scaling predictions.
5. Study mixing unit performance with predicted scaling concerns for a more accurate mixing unit design.

8.2.2 Packed Bed Reactor Network Recommendations

1. Measure sorption kinetic and thermodynamic properties at different temperatures, especially at 86.25 °C, the temperature of the inlet brine. This would eliminate the need for cooling towers and heat exchangers.
2. Measure lithium to sodium selectivity in adsorption reaction to determine the ratio of lithium to sodium hydroxide in the final product. If more sodium is adsorbed, further downstream processing will be necessary to reach desired purity.

3. Measure diffusion characteristics of adsorption and desorption reactions through the iron phosphate material to determine necessary residence time and lithium breakthrough into the reinjection well.
4. Measure heat capacity of the brine with additives for more accurate cooling tower design and assess need for cooling jacket to accommodate heat of reaction if brine is not satisfactory at removing heat.
5. Measure the heat of adsorption and desorption reactions to find temperature change of brine and stripping solution after reaction to determine if external cooling jacket is required to maintain specified temperature range for sorption.

8.2.3 Electrolysis Recommendations

1. Obtain potentiodynamic sweeps for cathode and anode reactions so overpotential can be estimated more accurately
2. Determine monoprotic ion selectivity of Nafion 117 using similar starting concentrations in electrolyzer so more accurate diffusion can be modeled across the membrane.
3. Determine the maximum allowable amount of sodium into the electrolyzer unit to maintain desired lithium to sodium hydroxide ratio in the final product and not disrupt lithium diffusion across the membrane.

8.2.4 Crystallization Recommendations

1. Study crystallization particle size distribution with varying residence time for a more accurate crystallization design.

8.2.5 Other Recommendations

1. Perform an economic and energetic analysis for parallel versus series cooling tower configuration for further capital and operational cost optimization.
2. Cooling tower performance study with higher salinity brine for more accurate cooling tower design.
3. Continual monitoring of subsidence and seismicity surrounding the wellhead for land stability assurance to inform the need for excess safety to be incorporated into final plant design.

8.3 Acknowledgements

We would like to thank Professor Eric W. Anderson of the Department of Chemical Engineering at the University of Virginia for advising us throughout the Capstone project. We would also like to thank Professor Gaurav Giri, Professor Gary Koenig, and Professor Geoffery Geise for providing essential data and for relaying relevant information from industry partners. Finally, we would like to thank Professor Nick Vecchiarello for his assistance in modeling the diffusion processes for the packed bed reactor system and Armando Shehi for his help with OLI modeling, used in an earlier document version.

.

SECTION 9: APPENDIX

List of Figure Titles

Appendix A: Section 4.2

A.1 Experimentally measured brine density extrapolation at ambient pressure

Appendix Table A.1. Experimentally measured brine density (A. Hawkins, personal communication, February 9, 2023)

Temperature (°C)	Density (g/mL)
20	1.238
45	1.226
70	1.219

From linear regression, y = -0.0004x + 1.2448.

Density at 86.25°C, the brine temperature at contact with mixing unit E-101 is 1.2103 g/mL from extrapolation

A.2 System inlet brine volumetric flow rate

$$6,000\ \frac{gal\ brine}{min} = 22712.47\ \frac{liters\ brine}{min}$$

A.3 Inlet brine constituents to E-101

Sample Unit Conversion:

$$1.2103\frac{g}{mL} = 1.2103\frac{kg}{L}$$

$$\frac{mg\ Constituent}{kg\ brine} * 1.2103\ \frac{kg\ brine}{L} = \frac{mg\ constituent}{L\ brine}$$

$$\frac{mg\ constituent}{L\ brine} * 22712.47\ \frac{L\ brine}{min} * \frac{1\ g}{1000\ mg} = \frac{g\ constituent}{min}$$

$$\frac{g\ constituent}{min} * \frac{mol\ constituent}{g} = \frac{mol\ constituent}{min}$$

Appendix Table A.3. Inlet brine constituents to E-101

	SLPB [mg/L brine]	Mass constituents (g/min)	Constituent Molar Mass (g/mol)	Constituent mols (mol/min)	Constituent mols (kg/hr)
Boron	520.4	11820	10.811	1093.35	65.60
Calcium	43086.68	978605	40.078	24417.51	1465.05
Chloride	214223.1	4865536	35.453	137239.04	8234.34
Iron	2021.201	45906	55.845	822.03	49.32
Potassium	21664.37	492051	39.0983	12584.98	755.10
Lithium	279.5793	6350	6.941	914.84	54.89
Manganese	2529.527	57452	54.9384	1045.75	62.74
Sodium	71891.82	1632841	22.99	71024.67	4261.48
Total	3.56E+05	8.09E+06	—	2.49E+09	1.49E+04

Moles of water calculation below, Appendix A.4.

A.4 Moles of Stream 1 inlet water to E-101

$$22712.47\ \frac{liters\ brine}{min} * 1.2103 \frac{kg\ brine}{L} = 5.16 * 10^8\ \frac{kg\ brine}{min}$$

From Appendix A.3, TDS flow rate = 8,090.56$\frac{kg\ salts}{min}$

Brine=Water+Salts

$$5.16 * 10^8\ \frac{kg\ brine}{min} - 8090.56\ \frac{kg\ salts}{min} = 5.08 * 10^8 \frac{kg\ water}{min}$$

$$5.08 * 10^8\ \frac{kg\ water}{min} * \frac{1000\ g}{1\ kg} * \frac{1\ mol}{18.02\ g\ H2O} = 2.82 * 10^{10} moles\ H_2O/min$$

A.5 Predicted $Ca_3(C_6H_5O_7)\cdot 4H_2O$ scaling rate to E-101

Calcium citrate solubility at 95°C: 1.85 g/L

Maximum soluble $Ca_3(C_6H_5O_7)\cdot 4H_2O$ in brine:

$$1.85\ \frac{g}{L} * 22712.47\ \frac{liters\ brine}{min} = 41563.8201\ \frac{g}{min}$$

Molar mass of $Ca_3(C_6H_5O_7)\cdot 4H_2O$: 570.5 g/mol

Maximum moles soluble in brine:

$$41563.8201\ \frac{g}{min} * \frac{1\ mol}{570.5\ g} = 72.855 \frac{mols}{min}$$

Moles of citrate added to brine: 815.58 mols/min

Insoluble moles of $Ca_3(C_6H_5O_7)\cdot 4H_2O$:

$$815.58\frac{mols}{min} - 72.855\frac{mols}{min} = 742.73\ \frac{mols}{min} = 44.56\ \frac{kmols}{hr}$$

A.6 Heat removal required for brine cooling in E-101

m= $1,639,115.92\ \frac{kg}{hr}$ summed from Table 3 Stream 6

$$1,639,115.92\ \frac{kg}{hr}\frac{1000\ g}{1\ kg} * \frac{1\ hr}{60\ min} = 2.73\ *\ 10^{7}\frac{g}{min}$$

$$Q = mC_p\Delta T$$

C_p =1 cal/g*C

$$\Delta T = 28°C - 86.25°C = -58.25°C$$

$Q = mC_p\Delta T$ =$(2.73\ *\ 10^{7}\frac{g}{min})(1\ \frac{cal}{g\ °C})(-58.25°C)$ =-1,591,308.37$\frac{kcal}{min}$

-1,591,308.37$\frac{kcal}{min}$= 111 MW released

A.7 Enthalpy of solution for tripotassium citrate monohydrate

$$7087\ \frac{J\ absorbed}{mol\ K_3C_6H_5O_7\cdot H_2O} *\ \frac{48.9\ kmol\ K_3C_6H_5O_7\cdot H_2O}{hr} * \frac{1000\ mol}{1\ kmol} = 346554300\frac{J}{hr}$$

$$346554300\frac{J}{hr} = 0.096\ MW\ absorbed$$

A.8 Enthalpy of solution for ferric chloride

$$19.82\ \frac{kcal}{mol} * \frac{1000\ mol}{1\ kmol} * \frac{6\ kmol}{hour} * \frac{1\ hour}{60\ min} = 1982\ \frac{kcal}{min} = 0.138\ MW\ released$$

A.9 Mixing Design Calculations

$$Re = \frac{\rho ND^2}{\mu} = \frac{(1220)(6.67)(0.67)^2}{0.019} = 1.9\ *\ 10^{6}$$

$$Np = \frac{P}{\rho N^3 D^5}$$

$$P = Np\ *\ \rho N^3 D^5 = 5.75\ *\ 1220\ *\ 6.67^3\ *\ 0.67^5 = 0.27\ MW$$

$$\tau = \frac{V}{V°} = \frac{6.3}{0.37} = 16.54\ seconds$$

Appendix B: Section 4.3

B.1 Reaction Favorability for Adsorption and Desorption

Adsorption	
Standard Cell	**Nernst Equation**
Reduction	Ecell = E0cell - (0.0592)log(Q)/n
FP(3+) + Li(+) + e- => LFP(2+)	n = 1 electron
Oxidation	Q = [Fe3+][LFP]/[Fe2+][FP]
Fe(2+) => e- + Fe(3+)	[LFP] = [FP] = 1
E0,LFP|FP = 0.41 V	Q = [Fe3+]/[Fe2+]
E0,Fe2|3+ = 0.244 V	Assume in brine 99:1 Fe2+:Fe3+
vs SHE	[Fe3+] = 1
E0cell = E0red - E0ox	[Fe2+] = 99
E0cell = 0.166 V	E0cell = 0.166 V
Constants	**Ecell = 0.2841416 V**
n = 1 electron	dG = -nFEcell
F = 96.5 kJ/V* mol e-	dG = -27.419665 KJ/mol
R = 0.008314 kJ/mol K	Keq = exp(dG/-RT)
T = 298 K	**Keq = 6.40E+04**

Adsorption Potential, ΔG and K_{eq} with Adjustment for $Fe^{2|3+}$ Concentration

Desorption	
Standard Cell	**Nernst Equation**
Reduction	Ecell = E0cell - (0.0592)log(Q)/n
Fe(3+) + e- => Fe(2+)	n = 1 electron
Oxidation	Q = [Fe2+][FP]/[Fe3+][LFP]
LFP(2+) => e- + FP(3+) + Li(+)	[LFP] = [FP] = 1
E0,Fe3|2+ = 0.77 V	Q = [Fe2+]/[Fe3+]
E0,LFP|FP = 0.41 V	Assume in FeCl3 99:1 Fe3+:Fe2+
vs SHE	[Fe3+] = 99
E0cell = E0red - E0ox	[Fe2+] = 1
E0cell = 0.36 V	E0cell = 0.36 V
Constants	**Ecell = 0.478142 V**
n = 1 electron	dG = -nFEcell
F = 96.5 kJ/V* mol e-	dG = -46.14066 KJ/mol
R = 0.008314 kJ/mol K	Keq = exp(dG/-RT)
T = 298 K	**Keq = 1.22E+08**

Desorption Potential, ΔG and K_{eq} with Adjustment for $Fe^{2|3+}$ Concentration

B.2. Variables Used in Bed Diameter Calculations

Parameter	Value
u_0(superficial velocity)	0.15 m/s
ε (porosity)	0.5
ρ_ρ (sorbent density)	2.49 gSorbent/cm^3
W_{sat} (maximum entrained conc.)	0.0613 gLi/gSorbent
c_0 (initial concentration)	231 mg Li/kg brine
t (time)	3600 s

As written by Davis & Davis, "Since the porosity of many solid catalysts falls between 0.3 and 0.7, a reasonable estimate of ε in the absence of experimental data is 0.5" (p. 195, 2003).

B.3. Ergun Equation Parameters for Pressure Drop Calculations

Adsorption

Parameter	Value
μ (viscosity)	0.000336 Pa s
u_0(superficial velocity)	0.15 m/s
ε (void fraction)	0.5
d_p(spherical equivalent diameter)	0.0009 m
ρ (density of fluid)	1238 kg/m^2

Desorption

Parameter	Value
μ (viscosity)	0.01 Pa s
u_0(superficial velocity)	0.0647 m/s
ε (void fraction)	0.5

d_p (spherical equivalent diameter)	0.0009 m
ρ (density of fluid)	1053 kg/m^2

B.4 Variables and Equations used in Lithium Capacity Calculations

Parameter	Value
V (bed volume)	9.06 m^3
ε (porosity)	0.5
ρ_ρ (sorbent density)	2.49 gSorbent/cm^3
W_{sat} (maximum entrained conc.)	0.0613 gLi/gSorbent
c_0 (initial concentration)	231 mg Li/kg brine
t (time)	3600 s
V_{in} (volumetric flow into bed)	0.3785 m^3/s

$$m_{Li,capacity} = V * \rho_\rho * \varepsilon * W_{sat}$$

$$m_{Li,actual} = V_{in} * c_0 * t$$

$$\%\ sites\ used = \frac{m_{Li,actual}}{m_{Li,capacity}}$$

B.5 Heat Released during Adsorption and Desorption

Moles of Li in Bed			Adsorption			Desorption		
pLi=	76318.5	gLi/m3	Values		units	Values		units
Vbed=	9.059	m3	cp=	4.184	J/gC	cp=	3.738	J/gC
MW=	6.94	gLi/mol	m_brine=	2.77E+07	g/min	m_strip=	9.89E+06	g/min
MLi = pLi*Vbed/MW			dT=	5.729	C	dT=	8.980	C
M_Li=	9.96E+04	mol Li						
Maximum heat of adsorption/desorption								
dh=	-4.00E+05	J/mol						

Change in Temperature of Brine and Stripping Solution from Sorption Reaction

B.6 Dimensionless Groups used in Numerical Solution for Shrinking Core Model

Dimensionless Group Name	Equation
Bed Length (ς)	$\varsigma = \frac{S*\delta_\varepsilon}{F*\rho_s*R^2*\iota}Z$
Time (τ)	$\tau = \frac{\delta_\varepsilon*t}{R^2} * \frac{X_0}{\rho_s*Y_h^*}$
Solid Phase Concentration (η)	$\eta = \frac{Y_{avg}}{Y_h^*}$
Liquid Phase Concentration (ξ)	$\xi = \frac{X}{X_0}$

B.7 Values for Variables in Dimensionless Groups

Adsorption

Variable Name	Value for Adsorption Model
Sorbent Quantity (S)	11278927 g Sorbent/bed
Effective Diffusivity* (δ_ε)	$5.31*10^{-9}$ m^2/s
Flow rate (F)	0.3784 m^3/s
Sorbent Density (ρ_s)	2490000 g Sorbent/m^3
Particle Radius (R)	0.00045 m
Total Length of Bed (ι)	3.6 m
Distance Coordinate (Z)	Varied 0-3.6 m
Mean Solid Phase Concentration (Y_{avg})	Solved for
Theoretical Solid Phase Equilibrium Conc. (Y_h^*)	8.83 mmol Li/g Sorbent
Liquid Phase Concentration (X)	Solved for
Initial Liquid Phase Concentration (X_0)	40280 mmol/m^3
Time (t)	Varied 0-3600 seconds

*Effective Diffusivity is calculated in Appendix B.8

Desorption

Variable Name	Value for Desorption Model
Sorbent Quantity (S)	11278927 g Sorbent/bed
Effective Diffusivity* (δ_ε)	$7.7681*10^{-10}$ m^2/s
Flow rate (F)	0.156 m^3/s
Sorbent Density (ρ_s)	2490000 g Sorbent/m^3
Particle Radius (R)	0.00045 m
Total Length of Bed (ι)	3.6 m
Distance Coordinate (Z)	Varied 0-3.6 m
Mean Solid Phase Concentration (Y_{avg})	Solved for
Theoretical Solid Phase Equilibrium Conc. (Y_h^*)	8.832853 mmol Li/g Sorbent
Liquid Phase Concentration (X)	Solved for
Initial Liquid Phase Concentration (X_0)	95797 mmol/m^3
Time (t)	Varied 0-7200 seconds

*Effective Diffusivity is calculated in Appendix B.7

B.8 Non-normalized Adsorption and Desorption Profile Figures

Adsorption

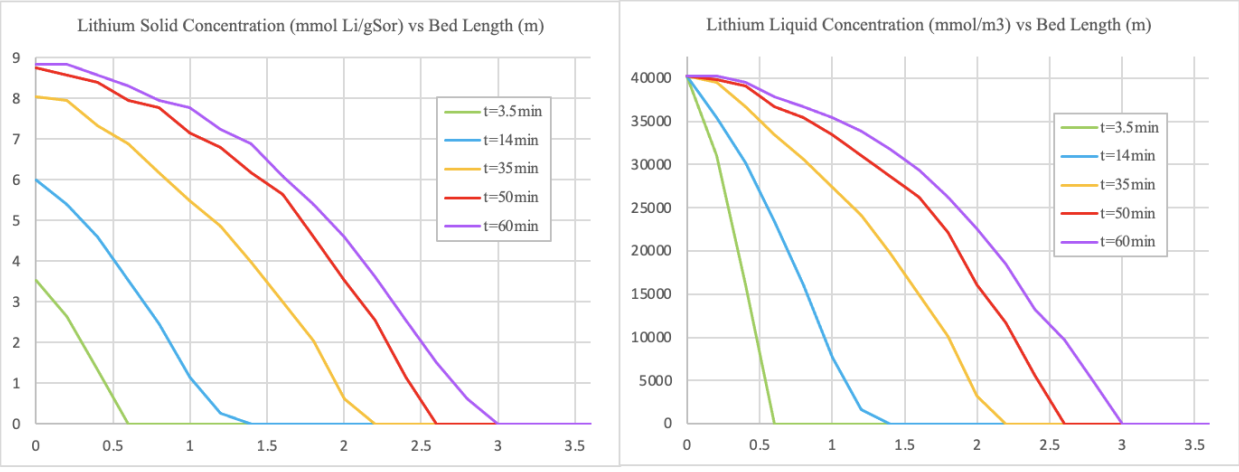

Desorption

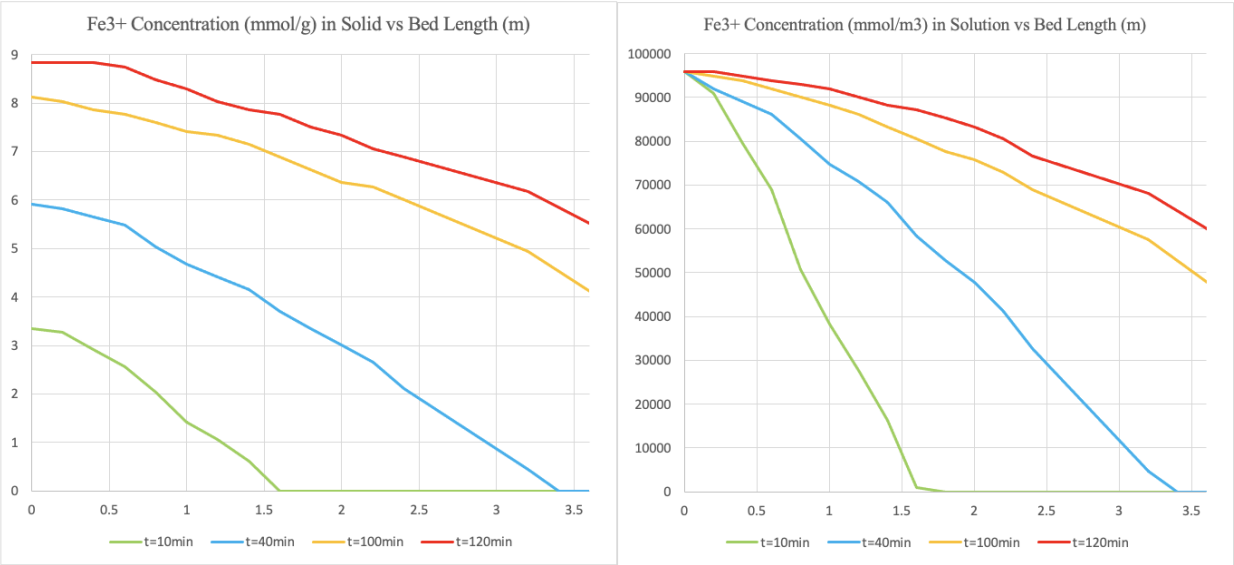

Concentration of Fe^{3+} is mmol/g Sorbent (left) and mmol/m^3 stripping solution (right)

B.9 Diffusivity Coefficient Calculations

Sorbent Loading: Diffusivity of lithium in brine solution

Using the Wilke-Chang equation:

$$\frac{D_{A,B}^{0} * \mu_B}{T} = 7.4 * 10^{-8} * \frac{(\phi_B M_{r,B})^{0.5}}{(\widehat{V}_A)^{0.6}}$$

Where μ_B is the brine viscosity (0.336 cP) found from OLI, T is the reactor temperature (298 K), $M_{r,B}$ is the brine's molar mass (21.9 g/mol), ϕ_B is the solvent association parameter (2.6) assuming water, and $\widehat{V}_A$ is the molar volume of lithium (13.0 cm^3/mol). With these values, $D_{A,B}^{0}$=0.000106 cm^2/s

The effective diffusivity is found assuming a porosity of 0.5 and a tortuosity of 1.0:

$$D^e = \frac{0.5}{1} * 0.000106 = 0.0000531\ cm^2/s$$

Sorbent Stripping: Diffusivity of ferric chloride in solution

Using the Wilke-Chang equation:

$$\frac{D_{A,B}^{0} * \mu_B}{T} = 7.4 * 10^{-8} * \frac{(\phi_B M_{r,B})^{0.5}}{(\widehat{V}_A)^{0.6}}$$

Where μ_B is the solution viscosity (0.894 cP) assuming dilute conditions, T is the reactor temperature (298 K), $M_{r,B}$ is the solution's molar mass (19.1 g/mol), ϕ_B is the solvent association

parameter (2.6) assuming water, and $\widehat{V}_A$ is the molar volume of $FeCl_3$ (56.0 cm^3/mol). With these values, $D^0_{A,B}$=0.0000155 cm^2/s

The effective diffusivity is found assuming a porosity of 0.5 and a tortuosity of 1.0:

$$D^e = \frac{0.5}{1} * 0.0000155 = 0.00000777\ cm^2/s$$

B.10 Mass Transfer Coefficient Calculations

Sorbent Loading

The Reynold's number through a packed bed reactor is found using:

$$Re = \frac{x*U*\rho_f}{\mu*(1-\varepsilon)} = 995$$

Where *x* is the FP particle diameter (0.0009 m), *U* is the superficial velocity (0.15 m/s), ρ_f is the brine density (1,240 kg/m^3), μ is the brine's dynamic viscosity (0.000336 kg/(m*s)), and ε is the bed porosity (0.5)

The Sherwood number is calculated using:

$$Sh = \frac{0.25}{\varepsilon} * Re^{0.69} * Sc^{0.333} = 172$$

Where Sc is the calculated Schmidt number (25.5)

$$k_{c,ext} = Sh * \frac{D_{A,B}}{x} = 0.00203 \text{ m/s}$$

Kc can be calculated using the following approximation:

$$k_{c,int} \approx \frac{10D_e}{x}$$

$$Kc = \left[\frac{1}{k_{c,ext}} + \frac{x}{10D_e}\right]^{-1} = 0.0000573 \text{ m/s}$$

Sorbent Stripping

The Reynold's number through a packed bed reactor is found using:

$$Re = \frac{x*U*\rho_f}{\mu*(1-\varepsilon)} = 137$$

Where *x* is the LFP particle diameter (0.0009 m), *U* is the superficial velocity (0.0647 m/s), ρ_f is the ferric chloride solution density (1,053 kg/m^3), μ is the solution's dynamic viscosity (0.000894 kg/(m*s)), and ε is the bed porosity (0.5)

The Sherwood number is calculated using:

$$Sh = \frac{0.25}{\varepsilon} * Re^{0.69} * Sc^{0.333} = 122$$

Where Sc is the calculated Schmidt number (546)

$$k_{c,ext} = Sh * \frac{D_{A,B}}{x} = 0.000211 \text{ m/s}$$

Kc can be calculated using the following approximation:

$$k_{c,int} \approx \frac{10D_e}{x}$$

$$Kc = \left[\frac{1}{k_{c,ext}} + \frac{x}{10D_e}\right]^{-1} = 0.00000829 \text{ m/s}$$

B.11 Biot Number Calculations

Sorbent Loading

$$Bi = \frac{k_c{}^*R}{D^0_{A,B}{}^*Kc} = \frac{0.00203*0.00045}{0.0000000106*0.0000573} = 1,500,000$$

Sorbent Stripping

$$Bi = \frac{k_c{}^*R}{D^0_{A,B}{}^*Kc} = \frac{0.000211*0.00045}{0.00000000155*0.00000829} = 7,360,000$$

B.12 Integral of Desorption Plot at t=100min

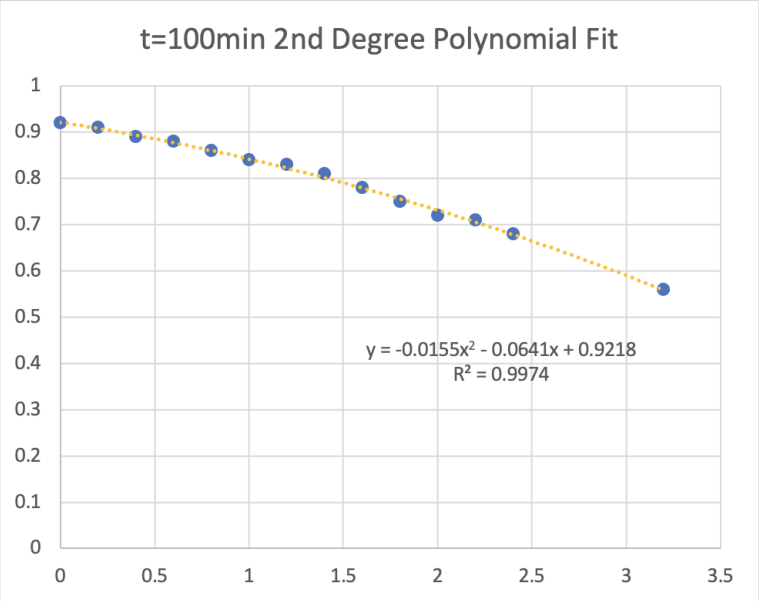

This curve fit was integrated over 0-3.6 meters then divided by 3.6 (area of graph) to find the percentage of sites filled at this time. This percentage is 73.9%.

$$\frac{\int_0^{3.6} -0.0155x^2 - 0.0641x + 0.9218\, dx}{3.6} = 0.739$$

Appendix C: Section 4.4

C.1 Standard Reduction Potential of Overall Reaction

$$E_0 = E_{red} - E_{ox} = -0.87V - 0.77V = -1.597\,V$$

C.2 Gibbs Free Energy Calculation

$$\Delta G = -nF\Delta E = -2 * 96485 * -1.597 = 308\,kJ/mol$$

C.3 Theoretical Current Needed for Production Rate of LiOH

$$I_{theory} = \frac{m_{theory} * z * F}{t*M} = \frac{3117*1*96484.5}{60*6.941} = 722,294\,A$$

C.4 Actual Current given Current Efficiency of 73%

$$I_{actual} = \frac{722,294}{0.73} = 985,797\,A$$

C.5 Power Calculation

$$P = I * V = 985,797 * 2.373 = 2.33\,MW$$

C.6 Power Generated from Reaction

$$P_{add} = I_{add} * V_{add} = (985797 - 722294) * 0.773 = 203,688\,W$$

C.7 Change in Temperature

$$P_{add} = m * Cp * \Delta T$$

$$\Delta T = \frac{P_{add}}{m*Cp} = \frac{203,688}{7301692*4.184} = 0.0066\,℃$$

Appendix D: Section 4.5

D.1 Crystallizer unit diameter calculation

$$\sqrt{\frac{0.68 * V}{\rho_v^{0.5} * 3600}} \leq D$$

D: unit minimum diameter, meters

ρ_v: density of the vapor phase=0.4658$\frac{kg}{m^3}$ from Aspen v.11 simulation

V: vapor mass flow rate (kg/hr)=10453.519 kg/hr from Aspen v.11 simulation

$$\sqrt{\frac{0.68 * 10453.519}{0.4658^{0.5} * 3600}} \leq 1.70\ m$$

D.2 Inlet solution velocity to crystallizer unit

$$v_i = \frac{Re * \mu_{sl}}{\rho_{sl} * D_v}$$

v_i inlet solution velocity: ($\frac{m}{s}$)

Re: Reynolds number=$5*10^6$

μ_{sl} : dynamic viscosity of the inlet solution: 0.000519 ($\frac{N\,s}{m^2}$) from Aspen v.11 simulation

D_v is the unit diameter (m): 1.70 m from Appendix D.1

ρ_{sl}: Density of inlet solution=693.555$\frac{kg}{m^3}$ from Aspen v.11 simulation

$$v_i = \frac{Re\mu_{sl}}{\rho_{sl} D_v} = \frac{5*10^6*0.000519}{693.555*1.70} = 2.2\ m/s$$

D.3 Diameter of inlet radial ports to crystallizer unit

$$D_i = \sqrt{\frac{Q*4}{3600*2\pi v_i}}$$

Q: total circulating solution flow rate: 16.996 $\frac{m^3}{hr}$

v_i: inlet solution velocity=2.19 m/s from Appendix D.2

$$D_i = \sqrt{\frac{Q*4}{3600*2\pi v_i}} = \sqrt{\frac{16.996*4}{3600*2\pi*2.2}} = 0.037\ m$$

Appendix E: Section 4.6

E.1 Inlet Gas Flow Rate to Cooling Tower 1

From Appendix Table A.6:

$$H_2O = 1.92 * 10^7 \frac{g}{min} = 19200 \frac{kg}{min}$$

$$Na^+ = 1620040.436 \frac{g}{min} = 1620.04 \frac{kg}{min}$$

$$Cl^- = 4833873.916 \frac{g}{min} = 4833.874 \frac{kg}{min}$$

Total mass of approximated brine: 25653.91 kg/min

E.2 Merkel Equation Tower Characteristic Approximation, Cooling Tower 1

86.25°C=359.4K

55°C=328.15K

$$\frac{Ka\bar{V}}{L} = \int_{T_C}^{T_H} \frac{C_L dT}{h_w - h_a} = \frac{3.292 \frac{kJ}{kg\,K}}{-1205.5 \left(\frac{kJ}{kg}\right) - -1280.07 \left(\frac{kJ}{kg}\right)} (359.4 - 328.15) = 1.38$$

E.3 Estimation of cooling tower cross-sectional area

$$34205 \frac{kg\ air}{min} * \frac{1}{1.107} \frac{m^3}{kg\ air} = 30899 \frac{m^3}{min}$$

$$2 \frac{m}{s} * \frac{60\ s}{1\ min} = 120 \frac{m}{min}$$

$$\frac{30899.02361 \frac{m^3}{min}}{120 \frac{m}{min}} = 257\ m^2$$

E.4 Mass transfer coefficient estimation from Thomas correlation

L' : water mass velocity per unit area ($\frac{kg}{m^2 s}$)

$$25653 \frac{kg\ brine}{min} * \frac{1\ min}{60\ sec} * \frac{1}{257\ m^2\ cross-sectional\ area} = 1.6605 \frac{kg\ brine}{m^2 s}$$

$G^{'}$: air mass velocity per unit area ($\frac{kg}{m^2 s}$)

$$34205 \frac{kg\ air}{min} * \frac{1\ min}{60\ sec} * \frac{1}{257\ m^2\ cross-sectional\ area} = 2.214\ \frac{kg\ air}{m^2 s}$$

$$Ka = 0.534375 L^{'0.747}\ G^{'0.253} = 0.534375(1.6605)^{0.747}(4.428)^{0.253} = 0.95\ \frac{kg}{m^3 s}$$

E.5 Cooling tower height calculation, C-101-A

$G^{'}$: air mass velocity per unit area ($\frac{kg}{m^2 s}$)=2.214 from Appendix E.4

$$Z = \frac{G}{Ka} \int_{Hy1}^{Hy2} \frac{dHy}{Hy^{*} - Hy} = \frac{2.214 \frac{kg}{m^2 s}}{0.95 \frac{kg}{m^3 s}} * 1.38 = 3.200\ meters$$

E.6. C-101 evaporative losses estimation

$$W_e = 0.00085 W_c (T_1 - T_2)$$

$$W_c = 6000\ \frac{gal}{min}$$

$$T_1 = 86.25\ C = 187.25\ F$$

$$T_2 = 28\ C = 82.4\ F$$

$$W_e = 0.00085 W_c (T_1 - T_2) = 0.00085 * (6000) * (187.25 - 82.4) = 534.735\ \frac{gal}{min}$$

E.7. C-101 drift losses estimation

$$W_d = 0.0002 W_c = 0.0002 * 6000 = 1.2\ \frac{gal}{min}$$

E.8 Overall heat transfer coefficient calculation

$$U_0 = [\frac{1}{h_0} + \frac{r_0 ln(r_0/r_i)}{k} + \frac{1}{h_i}\frac{r_0}{r_i}]^{-1}$$

where r_0 is the outer radius of the inner pipe, r_i is the inner radius of the inner pipe, k is the thermal conductivity of the tube wall, h_0 is the convective heat transfer coefficient outside the inner pipe, and h_i is the convective heat transfer coefficient inside the pipe

h_0≈7500 W/m^{2}K, estimated for LiPSS

$h_i \approx 7500$ W/m^{2}K, estimated for raw brine

$r_0 \approx 0.1$ m

$r_i \approx 0.06$ m

k≈17 W/mK for titanium

Appendix Table E.8A Ranges of Convective Heat Transfer Coefficient Values Encountered in Practice

System/Process	h (W/m² K)*
Air/free convection	5–50
Air/forced convection	25–250
Water/forced convection	250–15,000
Boiling	2,500–25,000
Condensation	5,000–100,000

Appendix Table E.8B Typical Values of Individual Heat Transfer Coefficients for Preliminary Design of Shell and Tube Heat Exchangers

System	h (W/m² K)
Steam condensation (film type)	2,500–20,000
Boiling water (pool boiling)	1,800–3,000
Boiling organics (pool boiling)	1,000–1,500
Condensing organic vapors	1,000–1,600
Cooling water	1,000–1500
Heat transfer oils	1,000–1,500
Light organic liquids	800–1,000
Heavy organic liquids	600–900
Oils	100–600
Air and low-pressure gases (forced convection)	20–100

*Data from Sinnott and Towler, *Chemical Engineering Design*, Elsevier, 2019, 6th edition.

Tables from Carta, G. (2021). *Heat and Mass Transfer for Chemical Engineers: Principles and Applications*. McGraw-Hill.

$$U_0 = \left[\frac{1}{h_0} + \frac{r_0 ln(r_0/r_i)}{k} + \frac{1}{h_i}\frac{r_0}{r_i}\right]^{-1} = \left[\frac{1}{7500} + \frac{0.1ln(0.1/0.06)}{17} + \frac{1}{7500}\frac{0.1}{0.06}\right]^{-1} = 298\, W/m^2K$$

E.9 Calculation of heat transfer area

$A_o = 2\pi r_o L N_{total}$

$r_0 \approx 0.1$ m

L≈10 m

$N_{total} \approx 318$ tubes per pass

$A_o = 2\pi(0.1m)(10m)(318) = 1998\, m^2$

E.10 Calculation for Logarithmic mean temperature difference

$$\Delta T_{lm} = \frac{(T_{H,out} - T_{C,in}) - (T_{H,in} - T_{C,out})}{ln\frac{(T_{H,out} - T_{C,in})}{(T_{H,in} - T_{C,out})}} = \frac{(86.25-28)-(110-85)}{ln\frac{86.25-28}{110-85}} = 39.3$$

E.11 Calculation for heat duty correction factor

$F_T(R, S)$

$S = \frac{T_{tube,out} - T_{tube,in}}{T_{shell,in} - T_{tube,in}} = 0.2896$ | $R = \frac{T_{shell,in} - T_{shell,out}}{T_{tube,out} - T_{tube,in}} = 2.4$

$F_T(R, S) \approx 0.96$

E.12 Calculation of heat exchanger heat duty

$Q = U_o A_o \Delta T_{lm} F_T(R, S) = 22,650$ kW

REFERENCES

Adeleke, O. A., Latiff, A. A., Saphira, M. R., Daud, Z., Ismail, N., Ahsan, A., Ab Aziz, N. A., Al-Gheethi, A., Kumar, V., Fadilat, A., & Apandi, N. (2019). Principles and mechanism of adsorption for the effective treatment of palm oil mill effluent for Water Reuse. *Nanotechnology in Water and Wastewater Treatment*, 1–33. doi.org/10.1016/b978-0-12-813902-8.00001-0

Alibaba. (2023). 1000M3/day large scale ro reverse osmosis pure water purifier machine RO treatment systems with Plug & Play. 1000m3/day Large Scale Ro Reverse Osmosis Pure Water Purifier Machine Ro Treatment Systems With Plug & Play - Buy Reverse Osmosis Water Treatment Systems,Pure Water Treatment Systems,Water Purifier Machines Product on Alibaba.com.

Apelblat, A. (1994). Enthalpies of solution of citrates and hydrogen citrates of lithium, sodium, and potassium. Journal of Chemical Thermodynamics, 26(1), 49–51. doi.org/https://doi.org/10.1006/jcht.1994.1019

Azizian, S., Eris, S., & Wilson, L. D. (2018). Re-evaluation of the century-old Langmuir isotherm for modeling adsorption phenomena in solution. *Chemical Physics*, *513*, 99–104. doi.org/10.1016/j.chemphys.2018.06.022

Bartell Ranch LLC v. McCullough, 2023 U.S. Dist. LEXIS 30864 (United States District Court for the District of NevadaFebruary 24, 2023, Filed). advance-lexis-com.proxy1.library.virginia.edu/api/document?collection=cases&id=urn:contentItem:67MN-S4V1-F7VM-S066-00000-00&context=1516831.

BNI & BHC (1978). Bechtel National, Inc. & Ben Holt Company. Feasibility and risk study of a geothermal power plant in the Salton Sea KGRA: Phase I interim report. *San Diego Gas and Electric Company.* www.osti.gov/servlets/purl/860582

Blackwood, T. (2023, March 8). *Consider high-speed belt conveyors*. Chemical Processing. https://www.chemicalprocessing.com/processing-equipment/powder-solids/article/11303256/consider-high-speed-belt-conveyors

Blair, J., Balcázar, R. M., Barandiarán, J., Maxwell, A. (2022). Exhausted: How We Can Stop Lithium Mining from Depleting Water Resources, Draining Wetlands, and Harming Communities in South America. *California State Polytechnic Pomona, Natural Resources Defense Council, Inc., Observatorio Plurinacional de Salares Andinos, University of California Santa Barbara.* www.nrdc.org/sites/default/files/exhausted-lithium-mining-south-america-report.pdf

Boulet, M., & Marier, J. R. (1960). Solubility of tricalcium citrate in solutions of variable ionic strength and in milk ultrafiltrates. *Journal of Dairy Science*, *43*(2), 155–164. doi.org/10.3168/jds.s0022-0302(60)90138-7

Brandani, S. (2020). Kinetics of liquid phase batch adsorption experiments. *Adsorption*, *27*(3), 353–368. doi.org/10.1007/s10450-020-00258-9

Brauch, V., & Schlünder, E. U. (1975). The scale-up of activated carbon columns for water purification, based on results from batch tests—II. *Chemical Engineering Science*, *30*(5-6), 539–548. doi.org/10.1016/0009-2509(75)80024-8

Carta, G. (2021). *Heat and Mass Transfer for Chemical Engineers: Principles and Applications*. McGraw-Hill

CDFW, CDWR, CNRA. (2017). California Department of Fish & Wildlife, California Department of Water Resources, California Natural Resources Agency. Salton Sea management program phase I: 10-Year plan. resources.ca.gov/CNRALegacyFiles/docs/salton_sea/ssmp-10-year-plan/SSMP-Phase-I-10-YR-Plan-with-appendices.pdf.

CEC (2020.). Selective recovery of lithium from geothermal brines. *California Energy Commission*. www.energy.ca.gov/publications/2020/selective-recovery-lithium-geothermal-brines

Cerutti, P. J. & Hepler, L. G. (1977). The enthalpy of solution of ferrous chloride in water at 298 K. *Thermochimica Acta,* 20(3), 309–314. doi.org/10.1016/0040-6031(77)85085-5

Davis, M. & Davis. R. (2003). *Fundamentals of Chemical Reaction Engineering*. McGraw-Hill.

Delevingne, L., Glazener, W., Grégoir, L., Henderson, K. (2020). Climate risk and decarbonization: What every mining CEO needs to know. *McKinsey & Company.* www.mckinsey.com/~/media/McKinsey/Business%20Functions/Sustainability/Our%20Insights/Climate%20risk%20and%20decarbonization%20What%20every%20mining%20CEO%20needs%20to%20know/Climate-risk-and-decarbonization-What-every-mining-CEO-needs-to-know.pdf

DiPippo, R. (1978). Geothermal plants of the United States: A technical survey of existing and planned installations. *Brown University, Department of Energy Division of Geothermal Energy.* www.osti.gov/servlets/purl/6389636

Dutch Association of Cost Engineers. (2016). Screw conveyors | DACE Price Booklet. www.dacepricebooklet.com/table-costs/screw-conveyors-0

Early, C. (2020, November 20). The new 'gold rush' for Green Lithium. *BBC Future.* www.bbc.com/future/article/20201124-how-geothermal-lithium-could-revolutionise-green-energy

Fan, L., Shi, J., & Xi, Y. (2020). PVDF-modified Nafion membrane for improved performance of MFC. *Membranes*, *10*(8), 185. doi.org/10.3390/membranes10080185

Ferrous chloride. Made-in-China. (n.d.). hdhg2022.en.made-in-china.com/product/KOctNifdMBpW/China-Ferrous-Chloride-FeCl2-le-2-0-.html

Fisenko, S. P., Brin, A. A., & Petruchik, A. I. (2004). Evaporative cooling of water in a mechanical draft cooling tower. *International Journal of Heat and Mass Transfer*, *47*(1), 165–177. doi.org/10.1016/s0017-9310(03)00409-5

Freedman, F. R., English, P., Wagner, J., Liu, Y., Venkatram, A., Tong, D. Q., Al-Hamdan, M. Z., Sorek-Hamer, M., Chatfield, R., Rivera, A., & Kinney, P. L. (2020). Spatial particulate fields during high winds in the Imperial Valley, California. *Atmosphere*, *11*(1), 88. doi.org/10.3390/atmos11010088

Gahleitner, G. (2013). Hydrogen from renewable electricity: An international review of power-to-gas pilot plants for stationary applications. international Journal of hydrogen energy, 38(5), 2039-2061.

Geankoplis, C. (2003). Chapter 10. Stage and Continuous Gas–Liquid Separation Processes. *Transport Processes and Separation Process Principles (Includes Unit Operations)* (4th ed.). *Pearson*.

Gharagheizi, F., Hayati, R., & Fatemi, S. (2007). Experimental study on the performance of mechanical cooling towers with two types of film packing. *Energy Conversion and Management*, *48*(1), 277–280. doi.org/10.1016/j.enconman.2006.04.002

Grageda, M., Gonzalez, A., Quispe, A., Ushak, S. (2020). Analysis of a Process for Producing Battery Grade Lithium Hydroxide by Membrane Electrodialysis. *Membranes*, *10*(8), 198. doi.org/10.3390/membranes10090198

Green, D. W., & Perry, R. H. (Eds.). (2008). 12-17 Evaporative Cooling. Perry's Chemical Engineers' Handbook (8th ed.). *McGraw-Hill*.

Grosjean, C., Miranda, P. H., Perrin, M., & Poggi, P. (2012). Assessment of World Lithium Resources and consequences of their geographic distribution on the expected development of the Electric Vehicle Industry. *Renewable and Sustainable Energy Reviews*, *16*(3), 1735–1744. doi.org/10.1016/j.rser.2011.11.023

GTO (n.d.). Geothermal Technologies Office. *Imperial Valley Geothermal Area*. www.energy.gov/eere/geothermal/imperial-valley-geothermal-area

Gupta, D., Zhang, Y., Nie, Z., Wang, J., Koenig, G. (2022, January 15). Chemical redox of lithium-ion solid electroactive material in a packed bed flow reactor. *Chemical Engineering Science.* doi.org/10.1016/j.ces.2022.117443

Hailes, O. (2022). Lithium in international law: Trade, investment, and the pursuit of Supply Chain Justice. *Journal of International Economic Law*, *25*(1), 148–170. doi.org/10.1093/jiel/jgac002

High purity ferric phosphate anhydrate iron phosphate. Alibaba. (n.d.). https://www.alibaba.com/product-detail/High-Purity-Ferric-Phosphate-Anhydrate-Iron_1600669647468.html?s%3Dp&sa=D&source=editors&ust=1680002938330474&usg=AOvVaw1LhXqFpjvGtDe91MVJGQIz

Hoffmann, M. (1975). *Brine Chemistry - Scaling and Corrosion: Geothermal Research Study in the Salton Sea Region of California*. Environmental Quality Laboratory California Institute of Technology. www.osti.gov/servlets/purl/7364728-VQTguC/

Hotellier, G., & Becker, I. (2013). Safety Concept of a self-sustaining PEM Hydrogen Electrolyzer System.

IEA (2022). International Energy Agency. The Role of Critical Minerals in Clean Energy Transitions. iea.blob.core.windows.net/assets/ffd2a83b-8c30-4e9d-980a-52b6d9a86fdc/TheRoleofCriticalMineralsinCleanEnergyTransitions.pdf

Irena – International Renewable Energy Agency. Green Hydrogen Cost Reduction. (2020). www.irena.org/-/media/Files/IRENA/Agency/Publication/2020/Dec/IRENA_Green_hydrogen_cost_2020.pdf

Jancic, S. J. and Grootscholten, P. A. M., Industrial Crystallization, Delft, D. Reidel Publishing Company, Dordrecht, The Netherlands (1984).

Kelly, R. (1975). Atmospheric Dispersion and Noise Propagation at Imperial Valley Geothermal Fields. *Lawrence Livermore National Laboratory.* www.osti.gov/servlets/purl/7357665

Kramer, H., & Lakerveld, R. (2019). Selection and Design of Industrial Crystallizers. In A. Myerson, D. Erdemir, & A. Lee (Eds.), *Handbook of Industrial Crystallization* (pp. 197-215). Cambridge: Cambridge University Press. doi:10.1017/9781139026949.007

KWS Manufacturing Company, Ltd. (n.d.). Screw Conveyor Interactive Calculators: Engineering Guide. www.kwsmfg.com/engineering-guides/screw-conveyor/kws-calculators/

London Metal Exchange. (2023, March). *About lithium*. www.lme.com/Metals/EV/About-Lithium

McCabe, W. L., Smith, J. C., & Harriott, P. (1993). Chapter 25 Adsorption. In Unit operations of Chemical Engineering (5th ed., pp. 810–837). *McGraw-Hill Inc.*

Majors, R. (2003). The Cleaning and Regeneration of Reversed-Phase HPLC Columns. *LCGC North America.* www.chemass.si/ca_content/Cleaning_and_maintaining_C-18_columns.pdf

Mongird, K., Viswanathan, V., & Alam, J. (2020, December). 2020 Grid Energy Storage Technology Cost and Performance Assessment. www.pnnl.gov/sites/default/files/media/file/Hydrogen_Methodology.pdf

Newman, H. H. and Bennett, R. C., "Circulating magma crystallizers," *Chem. Eng. Prog.* 55,65-70 (1959).

NORAM, HGA (Hunt, Guillot & Associates), APEX Geoscience Ltd., ECCI, Matrix Solutions Inc., METNETH2O Inc. (2021). Standard Lithium Ltd. preliminary economic assessment

of SW Arkansas lithium project. (Report No. NI 43 – 101) minedocs.com/21/SW-Arkansas-Lithium-Project-PEA-11202021.pdf

Olivetti, E. A., Ceder, G., Gaustad, G. G., & Fu, X. (2017). Lithium-ion battery supply chain considerations: Analysis of potential bottlenecks in critical metals. *Joule*, *1*(2), 229–243. doi.org/10.1016/j.joule.2017.08.019

Owens, M. S. (Ed.). (2005). Design conditions for Imperial, CA, USA. In ASHRAE Handbook: Fundamentals. *American Society of Heating, Refrigerating and Air-Conditioning Engineers.* cms.ashrae.biz/weatherdata/STATIONS/747185_s.pdf

Owens, M. S. (Ed.). (2009). Appendix: Design considerations for selected locations. In ASHRAE Handbook: Fundamentals. *American Society of Heating, Refrigerating and Air-Conditioning Engineers.* www.captiveaire.com/CatalogContent/Fans/Sup_MPU/doc/Winter_Summer_Design_Temps_US.pdf?v=17112015

Padron, G. A. (2001). *Measurement and comparison of power draw in batch rotor-stator mixers*. Measurement and Comparison of Power Draw in Batch Rotor-Stator Mixers. https://www.researchgate.net/publication/305281000_Measurement_and_Comparison_of_Power_Draw_in_Batch_Rotor-Stator_Mixers

Parker, S., Franklin, B., Williams, A., Cohen, B. S., Clifford, M., Rohde, M. (2022). Potential Lithium Extraction in the United States: Environmental, Economic, and Policy Implications. *The Nature Conservancy.* www.scienceforconservation.org/assets/downloads/Lithium_Report_FINAL.pdf

Potassium citrate monohydrate. Made-in-China. (n.d.). https://dongdu.en.made-in-china.com/product/emTrlJyEucVR/China-Food-Grade-Potassium-Citrate-Monohydrate.html

Unnerstall, R. J. (2022.). Fundamentals of Process Safety Lecture #7-Equipment Failures. Valve Types and Characteristics.

Ruthven, D. M. (2000). The Rectangular Isotherm Model for Adsorption Kinetics. *Adsorption*, *6*, 287–291. doi.org/https://doi.org/10.1023/A:1026504730443

Shublaq, M., & Sleiti, A. K. (2020). Experimental analysis of water evaporation losses in cooling towers using filters. *Applied Thermal Engineering*, *175*, 115418. doi.org/10.1016/j.applthermaleng.2020.115418

Simbol (2011). *Inlet to Simbol lithium extraction pilot plant*. Unpublished internal company document.

Soltani, M., Kashkooli, F. M., Souri, M., Rafiei, B., Jabarifar, M., Gharali, K., & Nathwani, J. S. (2021). Environmental, economic, and social impacts of geothermal energy systems. *Renewable and Sustainable Energy Reviews*, 140, 110750.

Sun, X., Liu, Z., Zhao, F., & Hao, H. (2021). Global competition in the lithium-ion battery supply chain: A novel perspective for criticality analysis. *Environmental Science & Technology*, *55*(18), 12180–12190. doi.org/10.1021/acs.est.1c03376

Taboada, M. E., Graber, T. A., Cisternas, L. A., Cheng, Y. S., & Ng, K. M. (2007). Process design for drowning-out crystallization of lithium hydroxide monohydrate. *Chemical Engineering Research and Design*, *85*(9), 1325–1330. doi.org/10.1205/cherd06251

Tavare, N. S. (1995). Crystallizer Design and Operation. In Industrial crystallization: Process simulation analysis and design (pp. 415–463). *Springer.* doi.org/10.1007/978-1-4899-0233-7_11

Tetenoire, A., Juaristi, J., Alducin, M. (2021). Insights into the Coadsorption and Reactivity of O and Co on Ru(0001) and Their Coverage Dependence. *J. Phys. Chem.* doi.org/10.1021/acs.jpcc.1c01618

Towler, G., & Sinnott, R. (2012). Chemical engineering design : Principles, practice and economics of plant and process design. Elsevier Science & Technology.

Turton, R., Shaeiwitz, J. A., Bhattacharyya, D., & Whiting, W. B. (2018). Analysis, synthesis, and design of Chemical Processes. Prentice Hall.

US DOE. (2022, July 13). United States Department of Energy. DOE announces finalists of Geothermal Lithium Extraction Prize. www.energy.gov/eere/articles/doe-announces-finalists-geothermal-lithium-extraction-prize

USGS (2022). United States Geological Survey. Mineral Commodity Summaries 2022. pubs.usgs.gov/periodicals/mcs2022/mcs2022.pdf

URI Chemistry Department. (n.d.). Standard Electrode (Reduction) Potentials in Aqueous Solution at 25C. www.chm.uri.edu/weuler/chm112/refmater/redpottable.html

Ventura, S., Bhamidi, S., Hornbostel, M., Nagar, A. (2020). Selective Recovery of Lithium from Geothermal Brines. *California Energy Commission*. www.energy.ca.gov/sites/default/files/2021-05/CEC-500-2020-020.pdf

Warren, Ian. (2021). Techno-Economic Analysis of Lithium Extraction from Geothermal Brines. *National Renewable Energy Laboratory*. www.nrel.gov/docs/fy21osti/79178.pdf

Wen, Y., Zhang, H., Qian, P., Zhou, H., Zhao, P., Yi, B., Yang, Y. (2006, March 29). Studies on Iron (Fe3+/Fe2+) -Complex/Bromine (Br2/Br-) Redox Flow Cell in Sodium Acetate Solution. *J. Electrochem. Soc.* DOI: 10.1149/1.2186040

World Economic Forum. (2023). www.weforum.org/agenda/2023/01/chart-countries-produce-lithium-world/

Zhang, H., Yang, Y., Ren, D., Wang, L., & He, X. (2021). Graphite as anode materials: Fundamental mechanism, recent progress and advances. *Energy Storage Materials*, *36*, 147–170. doi.org/10.1016/j.ensm.2020.12.027